

**Preparation of novel photoactive materials: different  
pre-compositions, post-modifications and improved  
performance**

**Dissertation**

zur Erlangung des akademischen Grades  
"doctor rerum naturalium"(Dr. rer. nat.)  
in der Wissenschaftsdisziplin Kolloidchemie

eingereicht an der  
**Mathematisch-Naturwissenschaftlichen Fakultät**  
der Universität Potsdam

von

**Lina Li**

Geboren am 22.11.1989

Potsdam-Golm, im Dezember 2017



# Contents

<b>1 Motivation and background</b> .....	5
1.1 Increasing energy demands and solar energies.....	5
1.2 Photochemistry and fundamental mechanism .....	7
1.3 Photocatalysis.....	8
1.4 Graphitic carbon nitride.....	13
1.5 Application of carbon nitride.....	15
1.6 Current challenges in photocatalysis .....	19
1.7 Methods to promote photocatalysis performance.....	20
1.8 Summary .....	25
<b>2 New organic photoactive semiconducting scaffolds by supramolecular preorganization</b> .....	26
2.1 Background and state-of-the-art.....	26
2.2 Synthesis and characterization of DBQ-M complex .....	28
2.3 Characterization of the supramolecular assembly after condensation at different temperatures.	30
2.4 Photochemical performance of DBQ-M materials.....	37
2.5 Conclusion.....	40
<b>3 1D photoactive semiconductors from chlorine substituted supramolecular assemblies and their improved photocatalytic performance</b> .....	42
3.1 Background and state-of-the-art.....	42
3.2 Synthesis and characterizations of M-CLA complex.....	44
3.3 Characterization of B-M-CLA condensed at different temperatures .....	50
3.4 Photoactivity of CLA-M materials.....	59
<b>4 Photocatalytic cyanation of graphitic carbon nitride scaffold: tuning band structure and enhancing the performance in green light driven C-S bond formation</b> .....	64
4.1 Background and state-of-the-art.....	64
4.2 Preparation methods of cyanation of graphitic carbon nitride scaffold.....	65
4.3 Characterization of g-C <sub>3</sub> N <sub>4</sub> -xCN materials. ....	66
4.4 Band structure and photocatalysis performance of g-C <sub>3</sub> N <sub>4</sub> -xCN materials.....	72
4.5 Conclusions .....	76
<b>5 Conclusions and outlooks</b> .....	78
<b>6 Appendix</b> .....	81
6.1 Characterization methods.....	81
6.2 Supplementary information.....	83

**7 Acknowledgment** ..... 94  
**8 References** ..... 95

# 1 Motivation and background

## 1.1 Increasing energy demands and solar energies

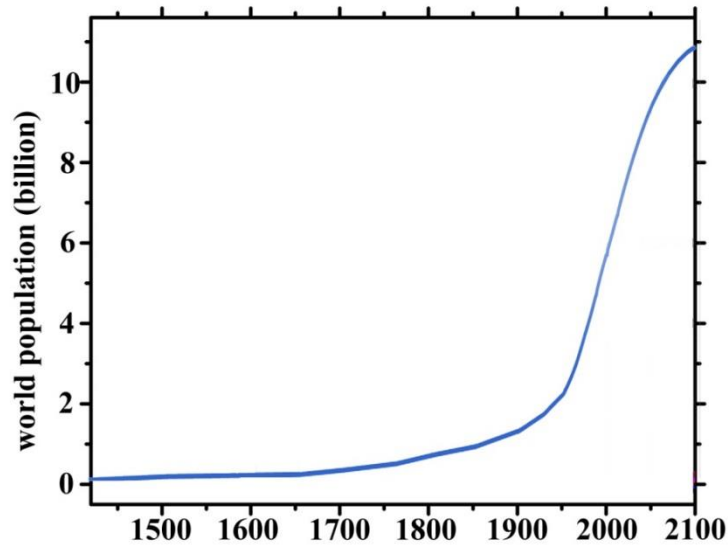


Figure 1.1 Growth of the world population in recent history.

Currently, the world population is experiencing an unprecedented fast growth, which is expected to exceed 9 billion in 2040, according to the world population prospects of the United Nations.<sup>[1] [2]</sup> The increasing numbers indicate bigger load on the earth system, while the universal yearning for better life standards is always inseparable from more resources and energy. Nowadays, over 80 % of energy is provided by fossil fuels, such as oil, coal and natural gases. However, the high dependency on fossil fuels is controversial and full of criticism, not only because it has led to regional dispute and even wars, but also due to the decline of fossil energy reserves.<sup>[3]</sup> Another worth mentioning shortcoming of fossil fuels is the inevitable carbon dioxide emission, which is extensively believed to be related to be global warming and recent extreme climate variations.<sup>[4]</sup>

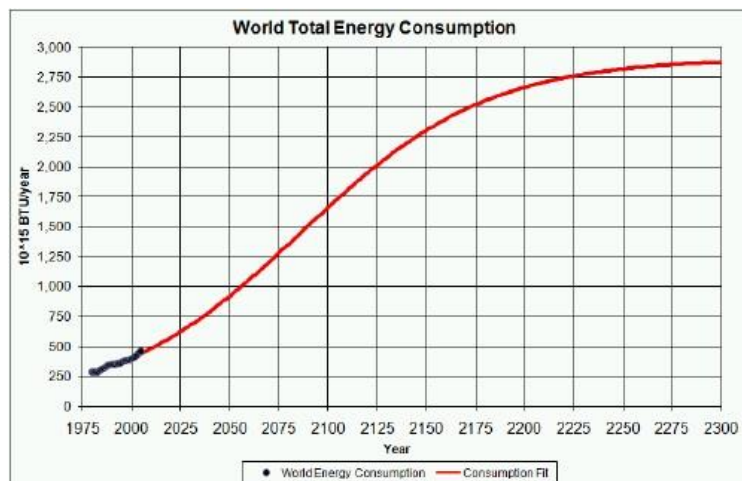


Figure 1.2 World total energy consumption records and prediction.<sup>[5]</sup>

In order to tackle all abovementioned problems, great efforts must be taken from the source. In other words, the general thinking should be focused on the renewable resources, such as solar, wind, geothermal and hydropower. The utilization of renewable energy has already got wide encouragement from government in a series of countries. According to the projections of the International Energy Outlook 2017, the consumption of renewable energy will be doubled to around 16 % in the coming 20 years, as the biggest increase among all sectors. Thus, methods of renewable energy production and application are of great research value.

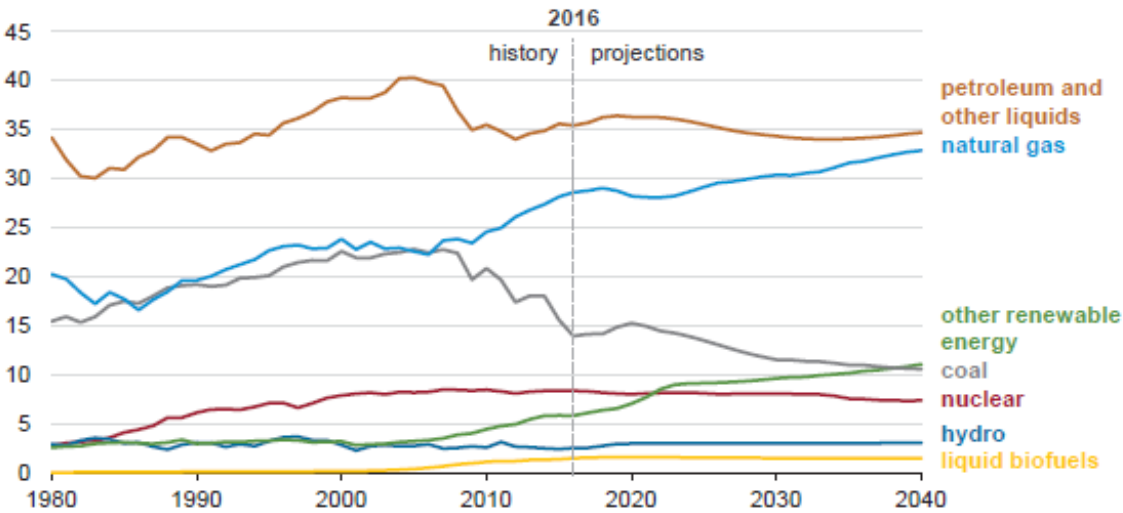


Figure 1.3 U.S. energy consumption history and projections. (quadrillion British thermal units) [6]

Among all the renewable energy sources, solar energy is most ubiquitous. This renewable energy is for free and could be found nearly in every country and region. In fact, 3,850,000 exajoules (EJ) of solar energy are absorbed by Earth's atmosphere, oceans and land. Specifically, the amount of energy absorbed by Earth in one hour is almost enough to cover the annual human consumption.[7] Encouraged by the potentiality of solar energy, the question how to effectively utilize light energy has become a hot research topic. Depending on the methods of capture, conversion and distribution, solar technologies could be characterized as either passive or active.[8] Active solar energy refers to energy harnessing using photovoltaic system, solar power concentration and water heating by means of solar radiation. Passive techniques usually refer to harnessing solar energy in the form of light and thermal utilization. Until now, the technologies related to application of solar energy has already been implemented in various fields, such as heating, electricity production, architecture, fuel production, etc.[9] It is to be assumed that the contribution of solar energy would be enhanced as research progresses in this area.

## 1.2 Photochemistry and fundamental mechanism

Solar energy conversion may be connected to photochemistry, which is a branch of chemistry concerned with the chemical effects of light. Generally, this subject mainly focuses on the chemical reaction caused by absorption of ultraviolet (100 - 400 nm) and visible light (400 – 750 nm) or infrared radiation (750– 2500 nm).<sup>[10]</sup> In photochemistry, light is of significance, not only because light can provide necessary energy to drive uphill processes, but also because some symmetry-forbidden state of molecular can only be made by excitation with light of a corresponding wavelength.<sup>[11]</sup>

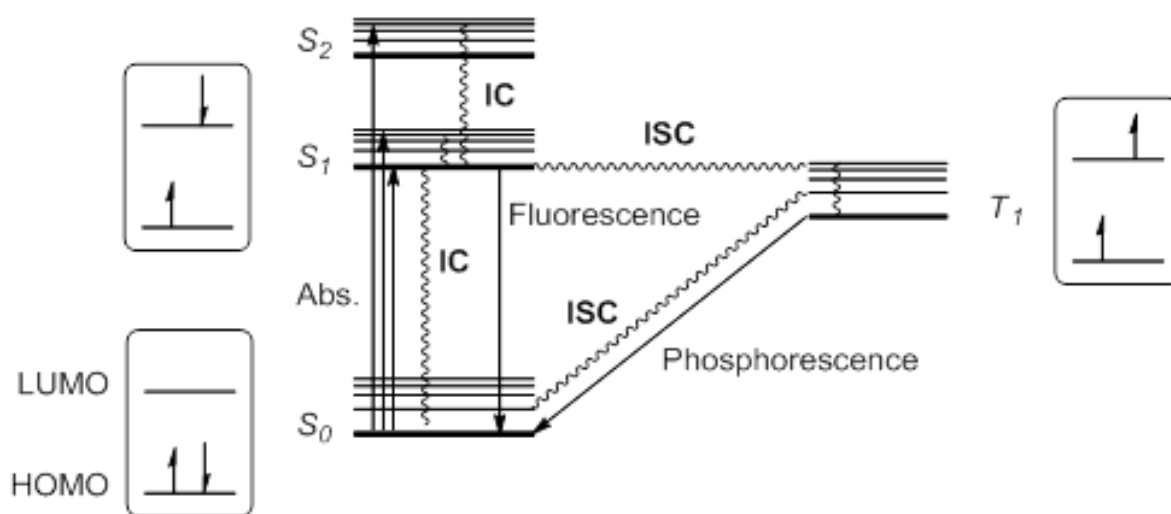


Figure 1.4 Jablonski diagram, a graphical depiction of the electronic states of a molecule and the transitions between those states. (The straight arrows mean radiative paths, while curly lines represent non-radiative paths.)<sup>[12]</sup>

Within a photochemical process, the first step usually is photoexcitation.<sup>[13]</sup> In order to elevate the chemical substance to the higher energy state, it is necessary for the reactant to absorb light according to the first law of photochemistry, known as the Grotthuss–Draper law. The energy of chemical substance and photon is quantified, that is, its energy can only adopt a specific value. In simple words, the substance can absorb photons with certain energy to reach the excited state.

When light is absorbed by a reactant molecule in the ground state ( $S_0$ ), one electron will be excited to a higher orbital level. During this excitation process, the electron still keeps its original spin. The singlet excitation can give rise to a series of excitation states ( $S_1$ ,  $S_2$ ,  $S_3$ , etc.) with different energies, because excitation to a higher level can occur for instance from the Highest Occupied Molecular Orbital (HOMO) to the Lowest Unoccupied Molecular Orbital (LUMO) or to another higher orbital. When the electron is excited to a higher state, it quickly relaxes *via* radiationless decay or internal conversion to the  $S_1$  state, which thus is the relevant excited state. The excited state  $S_1$  can further

lose energy and turn back to the  $S_0$  state *via* different paths. The most common pathway usually takes place within the molecular itself. The excited state  $S_1$  can also return to the ground state *via* radiative photon emission; this process is called fluorescence. It can also undergo spin inversion and to generate a triplet excited state  $T_1$ , and then relax to the ground state  $S_0$  by a radiation pathway called phosphorescence. No matter the excited molecular is in the form of  $S_1$  or  $T_1$ , it can also return to its ground state by radiationless internal conversion.<sup>[14]</sup>

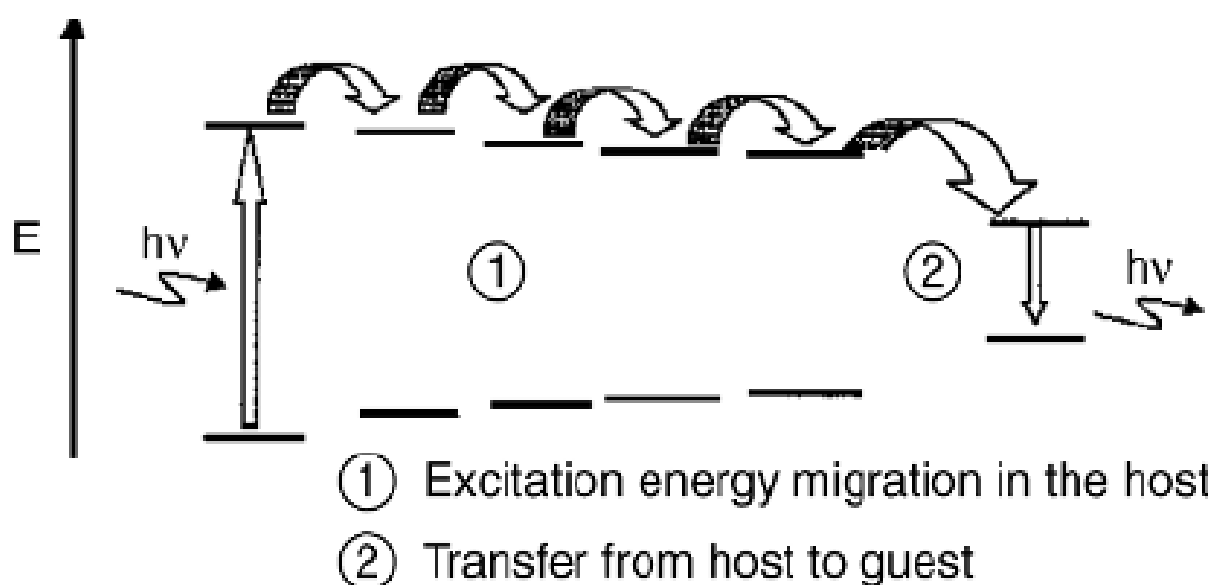


Figure 1.5 Excitation energy transfer and energy migration<sup>[15]</sup>

Besides, the energy of excited molecular can be transferred to another molecule as well, including vibrational relaxation, energy transfer and electron transfer.<sup>[16]</sup> The first possibility is vibrational relaxation, which means that the excessive vibration energy could be consumed by collision with other molecules. During energy transfer process, the excited molecule could pass the energy to another one to get itself into a lower electron energy level, while the acceptor turns into a higher electron energy state correspondingly.<sup>[17]</sup> The third method is electron transfer, during which the photo-excited donor interacts with an acceptor in the ground state to form an ion pair. This ion pair is likely to undergo a reverse electron transfer, thereby quenching the excited state. The fact that energy from photon can be transferred to other molecules provides foundation and more possibilities for photoreactions to take place.

### 1.3 Photocatalysis

Photocatalysis is defined as the acceleration of photoreaction in the presence of a catalyst.<sup>[18]</sup> In photocatalysis, photocatalyst can absorb light and get excited to create electron-hole pairs. During this process, free radicals can be generated, e.g. hydroxyl radicals  $\bullet\text{OH}$ , which will then boost the



secondary reactions and complete the whole photocatalysis cycle. Usually photocatalysis can be divided into two groups, homogeneous photocatalysis and heterogeneous photocatalysis.<sup>[19]</sup>

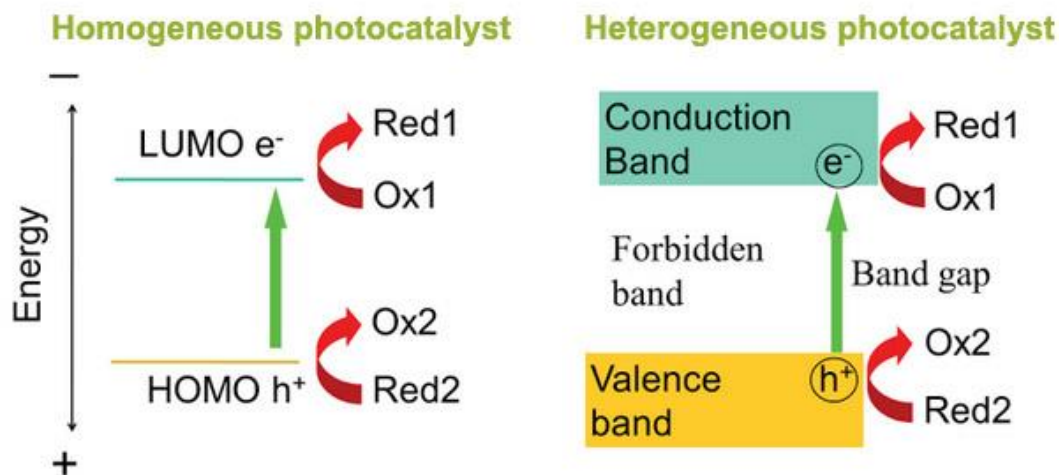


Figure 1.6 Photoexcitation and redox reactions of homogeneous and heterogeneous photocatalysts.<sup>[20]</sup>

In homogeneous photocatalysis, the reactants exist with the photocatalyst in the same phase. The homogeneous photocatalysts are typically presented by soluble metal complexes, such as porphyrin and  $[\text{Ru}(\text{bpy})_3]^{2+}$ , polyacids such as  $[\text{Si}(\text{W}_3\text{O}_{10})]^{4-}$  and dyes, e.g. eosin and rhodamine. In this photocatalysis, an electron from HOMO is excited to its LUMO under illumination, as shown in Figure 1.6.<sup>[20]</sup> Then, the photogenerated electrons and holes cause redox reaction and generate radicals. After radical generation, they can react with reactant substances in solution and complete the photocatalytic reaction.<sup>[21-23]</sup>

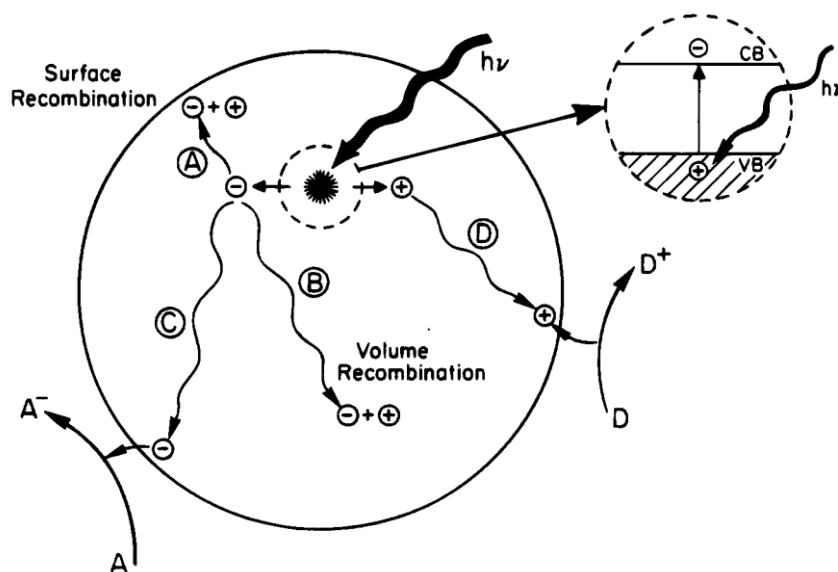


Figure 1.7 Schematic photoexcitation in a solid.<sup>[24]</sup>

For heterogeneous catalysis, the catalyst and the reactant are in different phases.<sup>[19]</sup> Most of heterogeneous catalysts are transition metal oxides and other semiconductors, which possess band structures.<sup>[19]</sup> The band occupied by electrons is named as valence band (VB) similar to HOMO, while the band not occupied by electrons is called conduction band (CB) similar to LUMO. Between VB and CB, there is a void energy region called band gap (BG), as shown in Figure 1.6b.<sup>[20]</sup> This region extends from the end of vacant conduction band to the top of the filled valence band. The existence of BG makes it unable to recombine electron and hole from the photoactivation, because they do not possess continuum of electronic states as metals do. When the absorbed photon has an energy equal or exceeding the band gap, an electron in the filled valence band is excited to the empty conduction band, leaving a photogenerated hole in the valence band.<sup>[24, 25]</sup> Figure 1.7 illustrates some recombination pathways for the separated electrons and holes. The photogenerated charges may migrate to the surface of the semiconductor, where they can react with absorbed substance or solvent. On the surface of the semiconductor, the electron can reduce an electron acceptor according to the path way C. Similarly, after migration, the photogenerated hole can combine with the electron from a donor, as shown in pathway D.<sup>[26]</sup> However, during this process, the photogenerated electron and hole can also recombine in the volume (pathway B) or on the surface (pathway A) of the semiconductor particle, which is of course undesired. The photoinduced charge recombination and photoinduced charge transportation occur in parallel, but the former one is often much faster than the latter one.<sup>[27]</sup> The influencing factors include crystal structure, crystallinity and particle sizes. In order to achieve a high photocatalysis result, it is significant to inhibit the recombination process. Methods related to the improvement of the photocatalytic activity include addition of metals, dopants, or combinations with other semiconductors, which have been proven to be effective to decrease recombination rate and thereby to increase photocatalytic efficiency. More details about possible modifications can be found in 1.7.<sup>[28, 29]</sup>

For homogeneous photocatalysts, the difficulty of photocatalyst separation from the reaction mixture becomes one of its shortcomings, which greatly inhibits application in industry. On the other hand, heterogeneous photocatalysis has its own advantages in practical applications, owing to their high photocatalytic performance and the ease of further separation from products by filtration or centrifugation.<sup>[30]</sup>

The research in the field of photocatalysis for energy generation has caught great attention, longing to mimic natural photosynthesis to utilize solar energy with artificial system. Because of the advantages mentioned above, the research in the field of on heterogeneous photocatalyst stays currently the central topic. A great deal of valuable academic research articles and patents have been published about the utilization and conversion of light energy under the action of heterogeneous photocatalysts.

An efficient and stable heterogeneous photocatalyst usually should satisfy several requirements.<sup>[26]</sup> In the first place, the catalyst itself must possess an appropriate band gap ( $3.5 \text{ eV} > E_g > 1.23 \text{ eV}$ ), which

is large enough to provide energetic electrons but still able to allow for efficient solar spectrum absorption.<sup>[31]</sup> Also, the qualified photocatalyst should effectively drive charge separation and realize electron transportation. Furthermore, it is quite necessary for the light harvesting antenna to be integrated with redox catalysts, which makes photogenerated charges able to participate in photoreaction. Finally, stability is also a key factor which ensures the photocatalyst is not poisoned or deactivated during the photoreaction.

The research boom in the field of heterogeneous photocatalyst can be traced back to the 1970s. In 1972, researchers found that  $\text{TiO}_2$  could decompose water into hydrogen and oxygen under UV light.<sup>[32]</sup> The photocurrent could flow from counter electrode to  $\text{TiO}_2$  electrode when  $\text{TiO}_2$  electrode is irradiated with UV light as shown in Figure 1.8. The current direction and further measurement indicated oxygen evolution reaction (OER) at the  $\text{TiO}_2$  electrode and hydrogen evolution reaction (HER) at the Pt electrode, when  $\text{TiO}_2$  electrode and Pt metal electrode are used as cathode and photoanode respectively. This observation shows water splitting does not have to rely on the application of an external voltage, instead water can be decomposed into  $\text{O}_2$  and  $\text{H}_2$  with  $\text{TiO}_2$  under UV light according to the scheme as follows.<sup>[33]</sup>

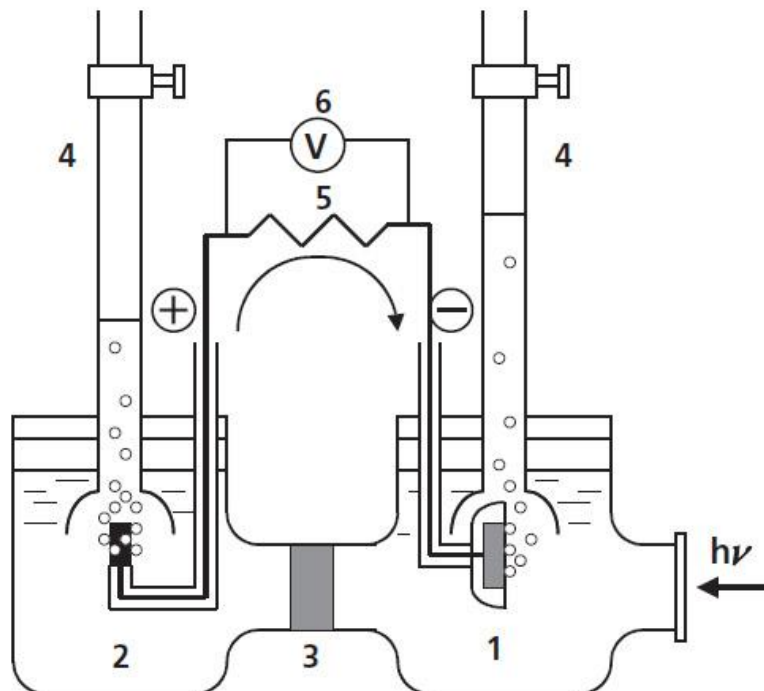


Figure 1.8 Schematic diagram of electrochemical photocell. (1) n-type  $\text{TiO}_2$  electrode; (2) platinum black counter electrode; (3) ionically conducting separator; (4) gas buret; (5) load resistance; (6) voltmeter.<sup>[33]</sup>



During that time, the price of crude oil kept increasing and potential energy lack became a central concern for human society. These factors greatly facilitated the development of the research using semiconductor based photocatalysis, owing to its potentiality in dealing with environmental and energy issues.

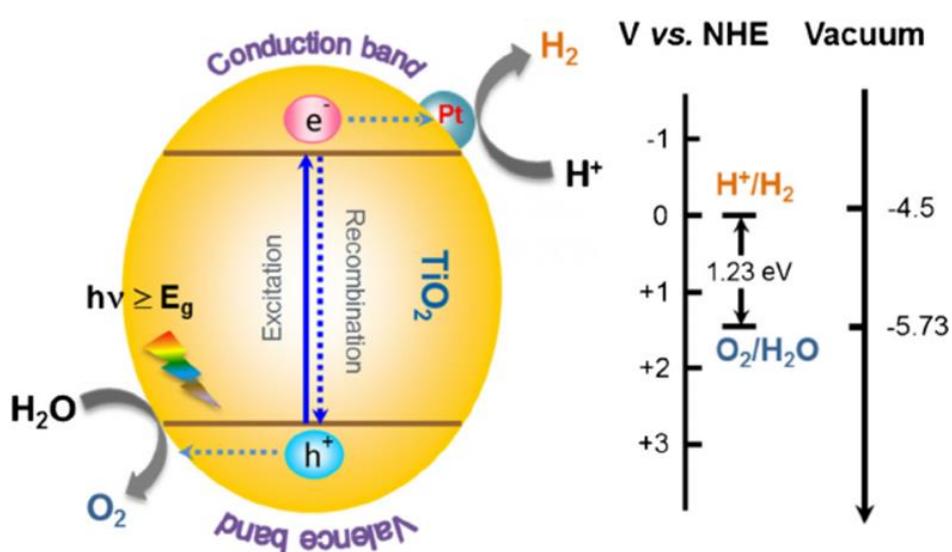


Figure 1.9 Schematic illustration of photocatalytic water splitting with  $\text{TiO}_2$  as photocatalyst.<sup>[34]</sup>

The too-large bandgap of 3.2 eV,  $\text{TiO}_2$  catalysts stimulated the creativity of researchers in photocatalysis. Considerable efforts have been devoted to promote catalysis performance by optimizing the catalytic system. In 1976, Carey reported that  $\text{TiO}_2$  aqueous suspension have strong photo-redox properties and could successfully degrade organic pollutant under illumination.<sup>[35-37]</sup> After that, various attempts have been made to utilize semiconductor to deal with pollutants in waste water.<sup>[38, 39]</sup> In 1980s, another application of photocatalysis has been discovered by Inoue and co-worker, namely that carbon dioxide can be reduced to various organic compounds under the action of photo-excited  $\text{TiO}_2$  powder.<sup>[40]</sup>

Represented by  $\text{TiO}_2$ , heterogeneous photocatalysis was extensively studied.<sup>[41]</sup> In recent 30 years, numerous reviews and reports have been published to show the achievements of highly efficient semiconductor-based photocatalysts fabrication.<sup>[42-45]</sup> Based on literature reports, the family of UV and visible light active photocatalysts is large, besides  $\text{TiO}_2$ , also including  $\text{ZnO}$ ,<sup>[46, 47]</sup>  $\text{Fe}_2\text{O}_3$ ,<sup>[48, 49]</sup>  $\text{CdS}$ ,<sup>[50, 51]</sup>  $\text{Bi}_2\text{WO}_6$ ,<sup>[52]</sup>  $\text{BiVO}_4$ ,<sup>[53]</sup>  $\text{Ta}_2\text{O}_5$ ,<sup>[54]</sup>  $\text{Ta}_3\text{N}_5$ ,<sup>[55]</sup> and others.<sup>[56]</sup>

## 1.4 Graphitic carbon nitride

In the recent decade, another type of heterogeneous photocatalyst has attracted interests of researchers, namely graphitic carbon nitride ( $g\text{-C}_3\text{N}_4$ ). Different from traditional  $\text{TiO}_2$ ,  $g\text{-C}_3\text{N}_4$  is a robust and visible-light-active polymeric semiconductor photocatalyst. More importantly, it possesses unique advantages, such as its facile synthesis, appealing electronic band structure, high thermal/chemical stability, and abundant precursors for preparation.<sup>[57-59]</sup>

In fact, the history of graphitic carbon dates back to the 1830s as one of the oldest synthetic polymer materials.<sup>[60, 61]</sup> At that time, it was first prepared by Berzelius and then named by Liebig as the embryonic form of melon, a linear polymer constructed from tri-*s*-triazine units and interconnected through tertiary nitrogen atoms.<sup>[62]</sup> As a heterogeneous catalyst, the utilization  $g\text{-C}_3\text{N}_4$  started around 2006.<sup>[63]</sup> In 2009 Wang and his co-workers first put forward the idea that  $g\text{-C}_3\text{N}_4$  can be used as a metal-free conjugated semiconductor photocatalyst for  $\text{H}_2$  evolution under visible-light irradiation in the presence of a sacrificial electron donor.<sup>[64]</sup> Since then, the research on photocatalyst has widened, and now includes not only inorganic semiconductors, but also polymeric conjugated semiconductor photocatalyst.

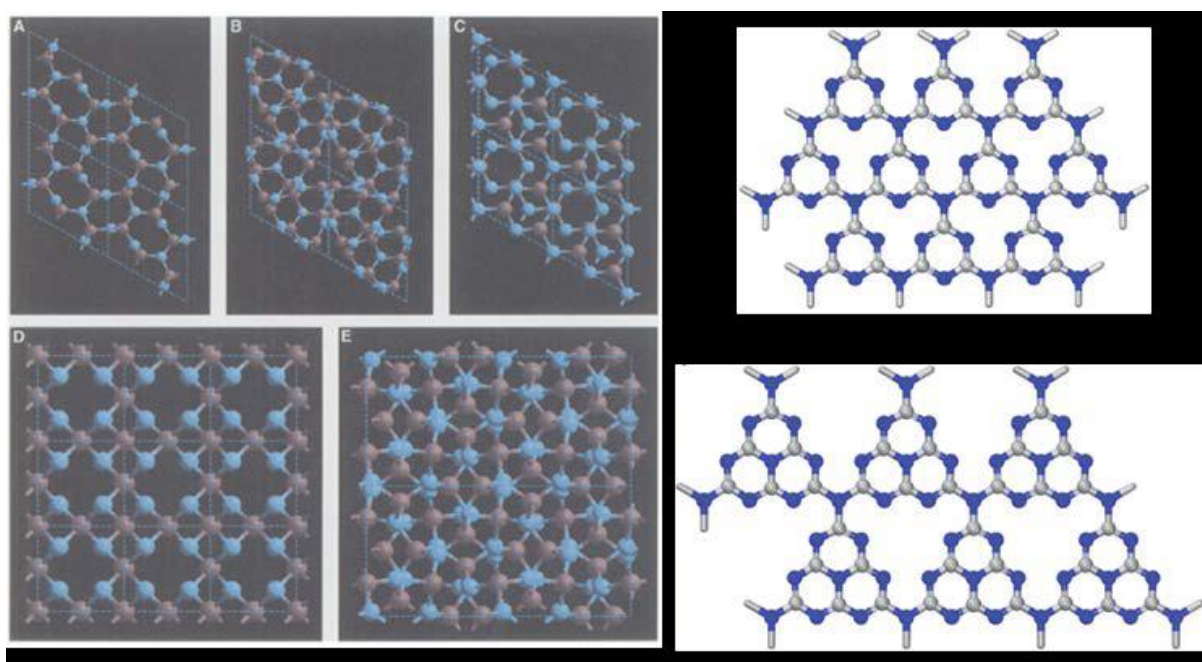


**Figure 1.10** Representation of (A)  $\beta\text{-C}_3\text{N}_4$ , (B)  $\alpha\text{-C}_3\text{N}_4$ , (C) graphitic- $\text{C}_3\text{N}_4$ , (D) pseudocubic- $\text{C}_3\text{N}_4$ , and (E) cubic- $\text{C}_3\text{N}_4$  structures down the [001] axis.<sup>[65]</sup> Schemes of idealized triazine ( $\text{C}_3\text{N}_3$ , up) and heptazine ( $\text{C}_6\text{N}_7$ , down) tri-*s*-triazine based  $g\text{-C}_3\text{N}_4$ ; blue and gray spheres represent nitrogen and carbon atoms, respectively.<sup>[65]</sup>

Carbon nitride has seven phase structures, which are  $\alpha\text{-C}_3\text{N}_4$ ,  $\beta\text{-C}_3\text{N}_4$ , cubic  $\text{C}_3\text{N}_4$ , pseudocubic  $\text{C}_3\text{N}_4$ , *g*-*h*-triazine, *g*-*o*-triazine, and *g*-*h*-heptazine as shown in Figure 1.10.<sup>[66]</sup> The basic tectonic unit

triazine ( $C_3N_3$ ) and heptazine ( $C_6N_7$ ) for  $g$ - $C_3N_4$  are presented in Figure 1.10. Even that there are different phases of carbon nitride, heptazine-based  $g$ - $C_3N_4$  is considered to comparatively more stable one as well as energetically favored one.<sup>[67]</sup>

As a semiconductor,  $g$ -carbon nitride has a band gap of 2.7 - 2.8 eV, with an onset visible light absorption of around 450 - 460 nm.<sup>[68]</sup> According to reports, the CB and VB of  $g$ - $C_3N_4$  are located at around -1.2 V and 1.5 V vs. NHE (pH = 7) respectively.<sup>[69]</sup> Among all  $C_3N_4$  structures,  $g$ - $C_3N_4$  is a very stable allotrope, which remains stable even up to 600 °C in air, owing to the stability of aromatic C–N heterocycles.<sup>[58]</sup> Also,  $g$ - $C_3N_4$  shows great chemical stability that it usually does not dissolve or react with acid, alkali, or organic solvents. Those excellent properties of carbon nitride have laid the base for the extensive research on it, as a promising metal-free semiconductor photocatalyst.

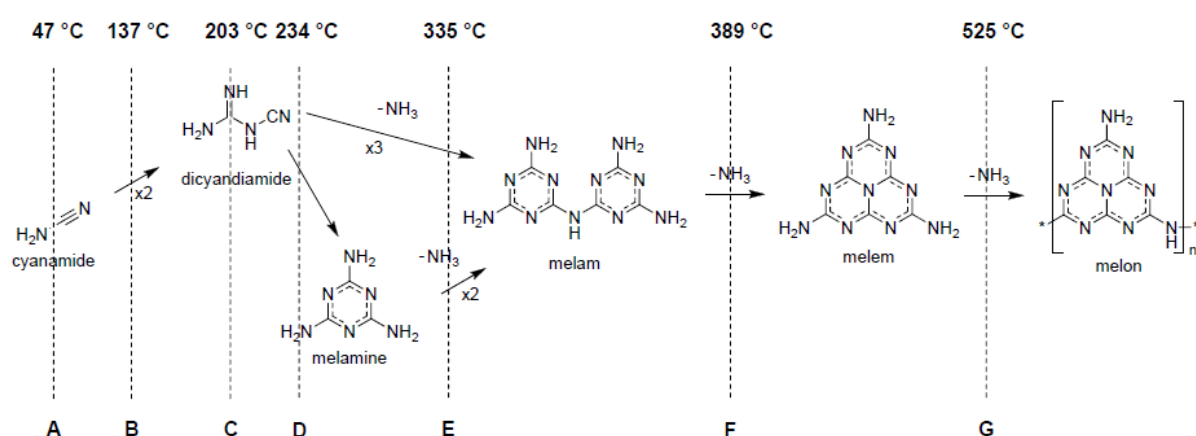


**Figure 1.11** The preparation of  $g$ - $C_3N_4$  from cyanamide: (A) melting of cyanamide, (B) dimerization of cyanamide to dicyandiamide, (C) melting of dicyandiamide, (D) condensation of dicyandiamide to melamine, (E) condensation of melamine to melam, (F) condensation of melam to melem, and (G) condensation of melem to melon.<sup>[70]</sup>

For preparation methods,  $g$ - $C_3N_4$  can be easily synthesized by thermal polymerization of abundant nitrogen-rich precursors. In fact, there are various precursors for  $g$ - $C_3N_4$  preparation, such as urea<sup>[59]</sup>, thiourea<sup>[71]</sup>, ammonium thiocyanate<sup>[72]</sup> and trithiocyanuric acid, guanidine thiocyanate, guanidinium chloride, and aminodichlorotriazine<sup>[73]</sup> and many more.<sup>[74, 75]</sup> Typical  $g$ - $C_3N_4$  synthesis from melamine usually involves multiple condensation processes. As shown in Figure 1.11, two molecules of cyanamide first condense into dicyandiamide at 137 °C and then dimerizes melamine at 234 °C. Afterwards, melam and melem are formed at 335 °C and 389 °C respectively with the release of ammonia. Then, melem could be further converted into polymeric  $g$ - $C_3N_4$  at around 525 °C. This material is commonly named as graphitic carbon nitride, despite it has only weakly ordered graphitic structures.<sup>[76]</sup> In fact, surface terminations and defects usually exist during its preparation process, because of potential incomplete condensation. However, these surface properties have been proved to

be the real active sites for electrons re-localization in heterogeneous catalysis, while the crystalline structure mainly contributes to its high thermal and chemical stability and electronic structures.<sup>[77, 78]</sup>

## 1.5 Application of carbon nitride

Many applications of carbon nitride have been explored, owing to its competent photocatalysis characteristics, such as, suitable band gap and CB/VB positions; satisfactory photocatalytic activity; thermal and chemical stability.<sup>[79]</sup> The enhanced performance of g-C<sub>3</sub>N<sub>4</sub>-based nanocomposites has been widely employed in environmental and energetic applications and exhibits outstanding catalytic performance in sacrificial water splitting, reduction of CO<sub>2</sub> into hydrocarbon fuels, and photodegradation of organic pollutants, *etc.*<sup>[80-84]</sup> In this section, this content will be briefly reviewed.

### 1.5.1 Photocatalytic water splitting

Owing to special properties of hydrogen as fuel, such as high efficiency, and being pollution-free, it has been considered as a promising alternative to tackle parts of the energy crisis. As most widespread substance, water is the best hydrogen resource, and water splitting becomes a promising method for energy acquisition. The suitable band gaps and CB/VB positions make g-carbon nitride an excellent candidate for water reduction and hydrogen generation.

The water splitting process could be described as follows. When absorbing light (energy larger than BG), photocatalyst would be excited and generate photoinduced electrons and holes at the CB and VB respectively. After the electrons are transferred to the active sites on the surface of semiconductor, it will act as reducing agents to drive substrate reduction, while the hole drives substrate oxidation on the surface. H<sub>2</sub>O molecules are reduced by a photoinduced electron, resulting in H<sub>2</sub> formation. On the other hand, H<sub>2</sub>O molecules are oxidized by the photoinduced holes to form O<sub>2</sub>. Besides, in order to effectively split water, the CB and VB of photocatalyst should satisfy some basic requirements. The CB bottom of the semiconductor has to be more negative than 0 V vs. NHE, which is the redox potential of H<sup>+</sup>/H<sub>2</sub>, while the VB top level should be more positive than 1.23 V vs. NHE (O<sub>2</sub>/H<sub>2</sub>O redox potential).

In the pioneering work of Wang and his coworkers, g-C<sub>3</sub>N<sub>4</sub> was for the first time successfully applied in water splitting. Even its photo-generated charges are prone to fast recombination, the half-reactions of water splitting (water reduction or water oxidation) could still be conducted separately in the presence of proper sacrificial agents.<sup>[85]</sup> For water reduction reaction, the common electron donors are ethylenediaminetetraacetic acid (EDTA), triethanolamine (TEOA), methanol, and ethanol, among which TEOA performs the best. In addition, the hydrogen evolution reaction typically relies on the help of cocatalyst. Thus, g-C<sub>3</sub>N<sub>4</sub> modified with 3 wt% Pt could generate 770 μmol H<sub>2</sub> under illumination after 72 h.<sup>[85]</sup> In order to realize water oxidation, AgNO<sub>3</sub> is usually the preferred



sacrificial electron acceptor. With the existence of electron acceptor and the cocatalyst RuO<sub>2</sub>, photocatalytic O<sub>2</sub> production amount was observed to reach 53 μmol under ultra violet illumination.<sup>[85]</sup>

In order to improve the photoactivity of g-C<sub>3</sub>N<sub>4</sub>, various approaches were employed in the water splitting experiment. First of all, the pH in the solution has been reported as one important factor. When the pH is turned to alkaline, there will be a significant enhancement in hydrogen evolution reaction.<sup>[86]</sup> In addition, the introduction of defects and disorder, such as create stacking defects, grain boundaries, surface termination sites, and heteroatom substitution, was also a reported to be an effective method.<sup>[87]</sup> Other approaches are doping with different elements, and utilization of artificial Z-scheme photocatalytic systems, noble metal deposition, and surface modification. Tremendous trials in the photocatalysis optimization lead to higher apparent quantum yield and much deeper understanding of semiconductor photocatalyst.<sup>[88-91]</sup>

### 1.5.2 CO<sub>2</sub> reduction reaction

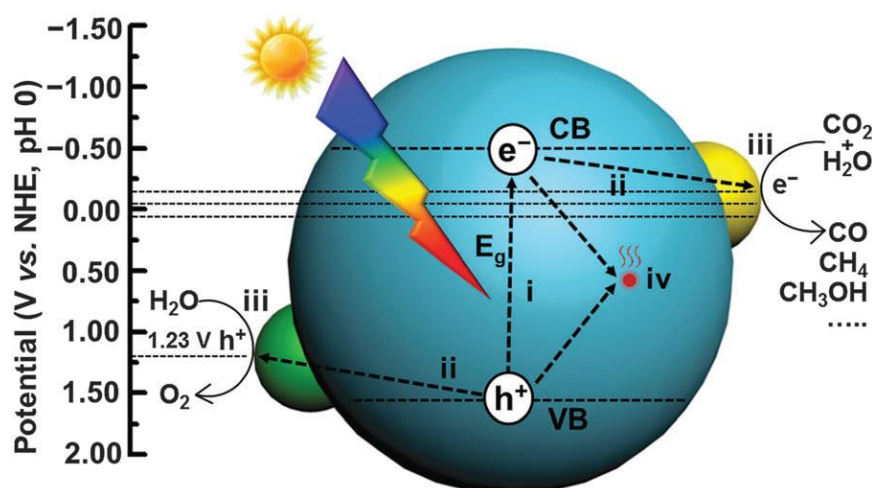


Figure 1.12 Schematic illustration of different steps in photocatalytic CO<sub>2</sub> reduction with H<sub>2</sub>O over a heterogeneous photocatalyst. The dotted lines indicate the thermodynamic potentials for water oxidation and CO<sub>2</sub> reduction into CO, CH<sub>4</sub> and CH<sub>3</sub>OH.<sup>[92]</sup>

Carbon fixation by artificial photosynthesis is considered as a potential route to solve current energy crisis and greenhouse effect. This process is quite difficult to accomplish, but valuable products of carbon dioxide into C1 compounds (containing one carbon atom) under solar illumination could be obtained, such as CO, CH<sub>4</sub>, CH<sub>3</sub>OH, HCHO, and HCOOH. As widely accepted, there are three crucial steps in photocatalytic system, which could be summarized as Figure 2.12.<sup>[92]</sup> In the first step, photocatalyst absorb photons with energy equal or higher than the band gap and electron-hole pairs are created. Then, the photogenerated electrons and holes independently migrate to the catalyst particle surface. These steps are very similar to water splitting mentioned above. Finally, CO<sub>2</sub> is reduced into fuels, such as CO, CH<sub>4</sub> or CH<sub>3</sub>OH by photogenerated electrons, while water molecules are oxidized into O<sub>2</sub> by photogenerated holes.<sup>[92, 93]</sup> Currently, the challenges for this process lie in the difficulty to



overcome the inert chemical structure of  $\text{CO}_2$ , the high overpotential for the  $\text{CO}_2^{\cdot-}$  intermediate formation and how to manage the proton coupled multiple electron processes. In order to improve photocatalysis performance, photocatalysts are usually modified with co-catalysts, like noble metal and metal oxides, which can effectively enhance the surface reaction kinetics by decreasing  $\text{CO}_2$  reduction overpotential.<sup>[94]</sup>

In recent years,  $\text{g-C}_3\text{N}_4$  has become one of the most promising photocatalyst for catalytic reduction of  $\text{CO}_2$ , owing to its high-lying CB minimum for reduction half-reaction.<sup>[95, 96]</sup> In 2012, Dong and Zhang reported the successful photoreduction of  $\text{CO}_2$  into CO over high porous  $\text{g-C}_3\text{N}_4$ .<sup>[97]</sup> After that, it was reported that  $\text{g-C}_3\text{N}_4$  nanosheets with a band gap of 2.97 eV gave  $\text{CH}_4$  as the main product, while  $\text{CH}_3\text{CHO}$  was the main product when bulk  $\text{g-C}_3\text{N}_4$  with a smaller band gap of 2.77 eV was employed.<sup>[98]</sup> In later reports, different approaches were applied, longing to enhance the  $\text{CO}_2$  reduction performance of  $\text{g-C}_3\text{N}_4$ , such as structure modifications, copolymerization, elemental doping and hybrid nano composites.<sup>[99-103]</sup> The reasons for these effective methods mainly result in improved  $\text{CO}_2$  adsorption and activation, promotion of visible light absorption, and better charge migration and separation.

Although current quantum efficiency is still not enough for industrial application,  $\text{CO}_2$  reduction to fuels over various types of  $\text{g-C}_3\text{N}_4$ -based materials has already established promising prospects in energy area. According to reports, till now significant achievements have been made in the photocatalytic reduction of  $\text{CO}_2$ . Those experiences accumulate and become the ambition of current researchers to design better photocatalysts and more efficient photocatalytic systems.<sup>[104]</sup>

### 1.5.3 Organic pollutants degradation

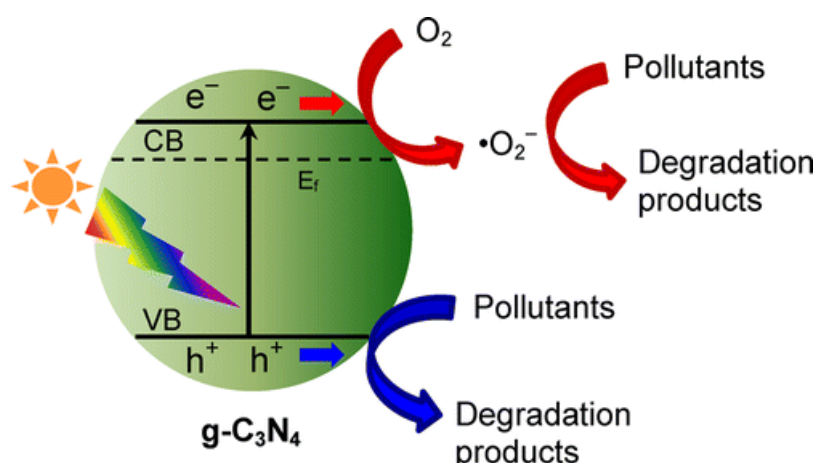


Figure 1.13 Schematic representation of photocatalytic pollutants degradation under light irradiation using pristine  $\text{g-C}_3\text{N}_4$  as a catalyst.

Research aimed to solve environmental issues caused by organic substances pollution is always a hotspot. Photocatalysts can be utilized to degrade organic pollutants into harmless compounds, or finally into CO<sub>2</sub> and H<sub>2</sub>O.<sup>[105]</sup> Generally in a typical pollution degradation process, the photo-generated holes oxidize water to form hydroxyl radicals and initiate a chain reaction. From the conduction band, photogenerated electrons can reduce O<sub>2</sub> first into superoxide radical O<sub>2</sub><sup>·-</sup> and then further into hydroxyl radical ·OH.<sup>[106]</sup> The hydroxyl radicals, on the other hand, attack pollutant molecules or their oxidation products, and boost the degradation process. In 2013, Sano and his co-workers reported that g-C<sub>3</sub>N<sub>4</sub> can be applied in NO oxidation.<sup>[107]</sup> According to other reports, g-C<sub>3</sub>N<sub>4</sub> also shows satisfying performance in formaldehyde removal.<sup>[108]</sup> Both NO<sub>x</sub> and formaldehyde are harmful pollutants in the atmosphere, therefore these discoveries make g-C<sub>3</sub>N<sub>4</sub> promising in environmental pollution control. Apart from gas pollutant degradation, another research focus on g-C<sub>3</sub>N<sub>4</sub> applied to pollutant degradation in the liquid phase. With organic dyes as model organic pollutant, g-C<sub>3</sub>N<sub>4</sub> is proved to be capable of generating reactive oxy-radicals, which in turn result in dye mineralization and further degradation of organic molecules. Till now, great advancements have been made, on the exploration of hybrid g-C<sub>3</sub>N<sub>4</sub> photocatalyst in organic degradation, such as Ag/g-C<sub>3</sub>N<sub>4</sub> systems,<sup>[109]</sup> WO<sub>3</sub>/g-C<sub>3</sub>N<sub>4</sub> systems,<sup>[110]</sup> ternary Fe(III)/graphene/g-C<sub>3</sub>N<sub>4</sub> composite,<sup>[111]</sup> H<sub>3</sub>PW<sub>12</sub>O<sub>40</sub>-modified g-C<sub>3</sub>N<sub>4</sub>,<sup>[112]</sup> etc. g-C<sub>3</sub>N<sub>4</sub> photocatalyst can be used not only for the treatment of organic pollution but also waste water contaminated with heavy metals.<sup>[113]</sup> With increasing reports on various organic models, carbon nitride shows a reliable degradation catalysis performance and point out a road to harness organic pollution problems.

#### 1.5.4 Photocatalytic organic synthesis

The preparation of organic chemicals is essential in the area of pharmaceuticals, pesticides, and food additives. However, as chemical industry is highly polluting, it becomes essential to find new green and environmental friendly steps and cascades within the chemical manufacturing processes. In recent reports, heterogeneous semiconductors seem to provide a green organic synthesis route for a number of industrially important chemicals.<sup>[114]</sup> After activation by light, the holes located at the VB of semiconductors are highly oxidizing and oxidize absorbed water or other substance, while photogenerated electrons would reduce dioxygen or take part in other reduction reactions.<sup>[114]</sup>

As metal free photocatalysts, CN materials recently also showed their potential in photocatalytic organic synthesis. The suitable band structures provide light-induced electrons with large reduction potential which can easily activate molecular oxygen to mediate energy and electron transfer. Moreover, the photogenerated holes possess a moderated oxidation potential which inhibit synthesized organic compounds being over oxidized. Thus, these features make CN materials gentle and ideal photocatalysts for organic synthesis.<sup>[115]</sup>

Throughout recent years, photocatalytic organic synthesis with CN materials has gradually become a hot research direction. It was first studied in photocatalytic oxidation reactions. With oxygen, carbon nitride can successfully transform aromatic and aliphatic alcohols into the corresponding aldehydes under visible light illumination ( $\lambda > 420 \text{ nm}$ ).<sup>[116]</sup> Under similar conditions, carbon nitride can also be employed to achieve metal-free aerobic oxidation of amines to imines, which can be used for effective preparation of benzoxazoles, benzimidazoles, and benzothiazoles.<sup>[115]</sup> Other examples are the oxidation of sulfides to sulfoxides and the selective oxidation of  $\alpha$ -hydroxy ketones to 1,2-diketones.<sup>[117, 118]</sup> Apart from those, there are also reports about CN materials being used in various reactions. For example, they are proven to be effective in Diels–Alder Reactions, in which the apparent quantum yield reaches a remarkable value of 47 % for the model reaction.<sup>[119]</sup>

### 1.6 Current challenges in photocatalysis

Even with so many great progress and research achievements, there are still some unsolved problems. Currently, the performance of heterogeneous photocatalysts still cannot satisfy the demands for solar utilization. The largest challenge lies in the improvement of the efficiency and stability of photocatalysts, which arise from the difficulties to control and balance the multiple competing processes, including carrier generation, charge separation and transportation.<sup>[26]</sup> The occurrence of photocatalytic reactions seriously depends on the transfer of photoinduced electrons and holes to the surface active sites of the semiconductor. Unfortunately, the photogenerated charge transfer process is much slower than the recombination process, which leads to lowered efficiencies. In order to overcome this shortcoming, several strategies have been applied, such as doping and heterostructure design.<sup>[120]</sup>

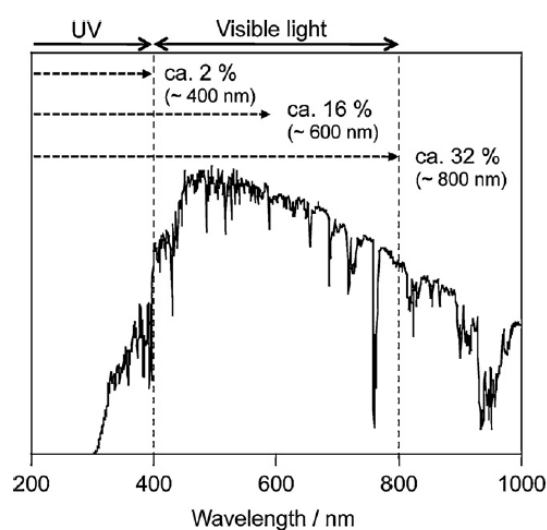


Figure 1.14 Solar spectrum and maximum solar light conversion efficiencies for water splitting reaction assuming 100% of quantum efficiency.<sup>[121]</sup>

The other reason for low efficiency originates from the poor solar energy utilization. Some available photocatalysts can only exhibit photoactivity in the ultraviolet or near ultraviolet range.<sup>[122]</sup> In the solar spectrum, 46% of its energy is however accounted for its visible part in the range 400-800 nm. As for UV light ( $\lambda < 400$  nm), it contributes only a tiny fragment, at around 4 % of the whole solar energy. If only UV light is utilized, the maximum theoretical solar energy conversion efficiency (SECE) is as low as 2 %, as shown in Figure 1.14. In fact, unmodified TiO<sub>2</sub> can only be excited by UV-photons, which greatly limits its application possibilities. Compared with TiO<sub>2</sub>, the absorption range of g-C<sub>3</sub>N<sub>4</sub> is wider and can absorb photons up to 460 nm, however it still cannot cover the full range of visible light. Therefore, further research on new photocatalysts are still of great significance, and no efforts should be spared to enhance photocatalytic efficiency in order to make better use of solar energy resources.

## 1.7 Methods to promote photocatalysis performance

For the photocatalyst preparation and modification, great deals of trials have already been used to improve the catalysis performance. In order to obtain photocatalysts with even better performance, the new generation should be elaborately designed to widen optical absorption, to improve charge carrier generation, separation, transportation and utilization.<sup>[123]</sup> Usually, the modification methods include morphology and size control synthesis, codeposition of noble metals, nonmetal-doping, semiconductor heterostructures, surface modification and so on.<sup>[26, 56, 124]</sup>

### 1.7.1 Morphology and size control synthesis

Morphology usually has a great impact on material properties, and similarly on its photocatalytic behavior. Represented by graphene and carbon nitride, the boom of two-dimensional materials progressively promotes the development of photocatalysis. However, other structurally different materials also have their own advantages in photocatalysis. Three-dimensional materials tend to possess high specific surface area, high adsorptive capacity, high structure stability, low gas resistance and a large number of exposed active sites for photocatalytic reactions. For example, 3-dimensional perylene monoimide amphiphilic supramolecular self-assembly shows enhanced photocatalytic hydrogen production<sup>[125]</sup> and porous g-C<sub>3</sub>N<sub>4</sub>-based composite hydrogels exhibit improved pollutant degradation behavior.<sup>[107, 126-128]</sup> As for one-dimensional materials, they show distinct chemical and structural behaviors and greater chemical reactivity, because they can directly help with quantum particle (photons, phonons, and electrons) transmission, such as TiO<sub>2</sub> nanostructure for organic degradation<sup>[129]</sup> and 1-d ZnO, and CdS for selective oxidation<sup>[130-132]</sup> Therefore, the research on the catalyst morphology indeed is of significance and may even boost the development of photocatalysts.

The size of photocatalyst also has a great influence on its photochemistry behavior. When the particle size of semiconductors drops to nanoscale, their properties can be greatly changed.<sup>[133]</sup> Compared with

normal bulk materials, nano-size materials usually possess high photostability, tunable absorption spectrum, larger potentially catalytic surface, and high fluorescence quantum yields. *Via* liquid phase exfoliation, Yang and co-workers prepared g-C<sub>3</sub>N<sub>4</sub> nanosheets which showed improved H<sub>2</sub> evolution performance, as well as enhanced quantum yield.<sup>[134]</sup> Nanosized g-C<sub>3</sub>N<sub>4</sub> can also be grafted onto other material, like single-crystalline TiO<sub>2</sub> and Metal Organic Frameworks, which demonstrated improved stable synergetic photoelectrocatalysis and photocatalytic CO<sub>2</sub> reduction, respectively.<sup>[135, 136]</sup> For instance, TiO<sub>2</sub> showed best photocatalytic activity at a particle width of 40 nm, which is because of the benefits provided by its size, such as optimized balance between efficient separation of redox sites and large specific surface area.<sup>[137]</sup>

### 1.7.2 Metal and non-metal doping

In order to obtain higher photocatalysis performance, different dopants are introduced to modify optical, electronic, luminescent and other physical properties of photocatalysts, which can generally be divided into metal and non-metal doping.

According to previous reports, Fe, Cu, Zn, and Ni have been broadly used to adjust optical and electronic properties of g-C<sub>3</sub>N<sub>4</sub>. These metal dopants can effectively promote photocatalytic activity by increasing light absorption range, changing band gap, and facilitating charges migration. A small amount of metal doping could effectively retard the recombination process, and improve the photocatalysis performance of catalysts.<sup>[138]</sup> In addition, high defect density, coming from suitable doping, may suppress the recombination process as well.<sup>[139]</sup> In 2009, Wang demonstrated that the inclusion of Zn<sup>2+</sup> and Fe<sup>2+</sup> into the framework could form a host-guest interaction with g-C<sub>3</sub>N<sub>4</sub>, which helped to increase light absorption and shift band gap.<sup>[140]</sup> After that, other transition metal dopants were reported with similar functions, such as Ni<sup>2+</sup>, Cu<sup>2+</sup>, Co<sup>3+</sup> and Mn<sup>3+</sup>.<sup>[141-144]</sup> Apart from that, alkali metal ions were also reported to be able to coordinate into the nitrogen pots of g-C<sub>3</sub>N<sub>4</sub> and enhance photocatalytic redox reactions.<sup>[145, 146]</sup>

As worth mentioning, non-metal doping is also a promising approach to overcome the drawbacks of photocatalyst. The non-metal (N, O, S, P, B, *etc*) elements can take sites in the original catalyst.<sup>[147]</sup> Compared with metal doping, this method avoids the thermal variation of chemical states of doped metal ions. The introduction of non-metal dopants proves to be effective in promoting charge separation rates and pollutant degradation efficiency during photocatalysis process.<sup>[148]</sup> For example, compared with carbon nitride, oxygen-doped g-C<sub>3</sub>N<sub>4</sub> can improve the visible-light absorption, produce more active sites and reduce the recombination of electron/hole pairs, while sulfur dopants promotes its effectiveness in photodegradation and H<sub>2</sub> evolution, CO<sub>2</sub> reduction and water oxidation.<sup>[149-151]</sup> However, it is necessary to point out that excessive doping would be harmful for photocatalyst, because excessive defects usually break the semiconductor structure and promote electron-hole pair recombination.<sup>[88, 152]</sup>

In general, element doping is an excellent method to adjust photocatalysis properties, which can be further applied to  $g\text{-C}_3\text{N}_4$  based materials to broaden its application in organic photosynthesis, and even photoelectrochemistry.

### 1.7.3 Semiconductor heterojunction

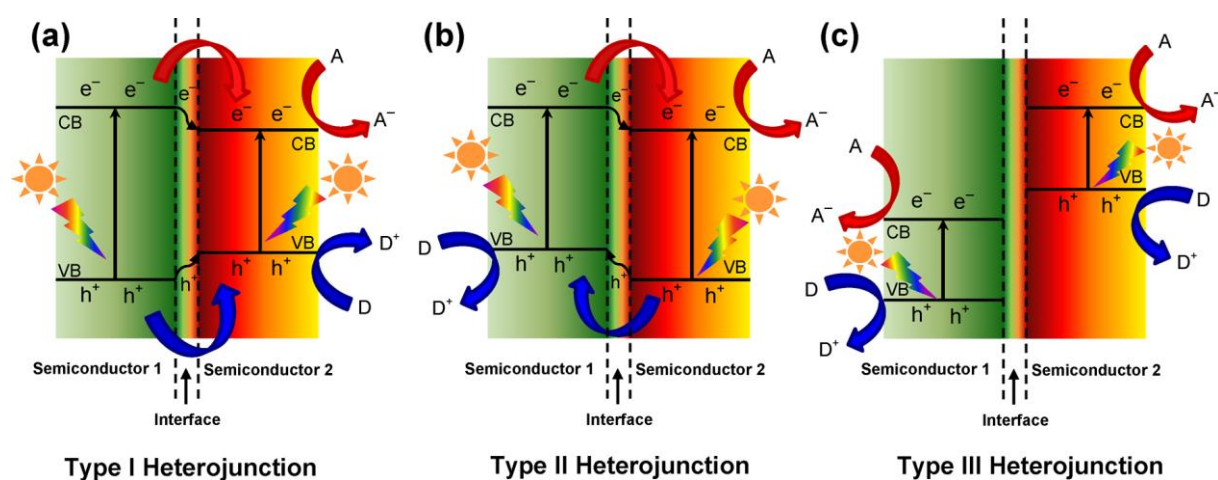


Figure 1.15 Three types of heterojunctions; A and D represents for electron acceptor and donor, respectively.

Although the preparation of single component catalysts can be controlled in the terms of chemical composition, size and morphology, the electronic properties of this material is confined to a certain range. In such case, heterojunction design seems to be necessary, because it makes up for the deficiencies in its each band gap position and effectively improve their photo-catalytic performance. For a typical  $g\text{-C}_3\text{N}_4$ -based heterojunction, the new photocatalyst is composed of a  $g\text{-C}_3\text{N}_4$  semiconductor photocatalyst and another semiconductor. For the  $g\text{-C}_3\text{N}_4$  based heterojunction nanocomposites, the VB and CB potentials of the other semiconductor can be different from  $g\text{-C}_3\text{N}_4$ . Depending on the band energy difference of these semiconductors, the new incorporated photocatalyst can be employed in different uses, such as  $\text{H}_2\text{O}$  splitting,  $\text{CO}_2$  reduction and pollutant degradation. After the hybridization between  $g\text{-C}_3\text{N}_4$  and the new coming semiconductor, a new electronic structure is formed because of potential difference and band bending.<sup>[153]</sup> This hybridization lead to a new electric field in the new catalyst which helps with the charge separation and migration in space.<sup>[154]</sup> According to the band gap position of the hybridized semiconductor, there are three heterojunction structures, namely Type I (straddling gap), Type II (staggered gap) and Type III (broken gap) heterojunctions as shown in Figure 1.15.<sup>[155]</sup>

$g\text{-C}_3\text{N}_4$  possesses an open 2 D flat morphology, of whose flexibility makes it an excellent material for heterojunction formation. In general, semiconductor heterojunction could provide better light utilization, lower redox overpotentials, more effective charge transfer and separation, and enhanced

system stability.<sup>[56]</sup> Based on recent references, there are seven main heterojunctions for g-C<sub>3</sub>N<sub>4</sub> based photocatalysts, which are (i) inorganic semiconductor/g-C<sub>3</sub>N<sub>4</sub> heterojunctions, (ii) metal/g-C<sub>3</sub>N<sub>4</sub> heterojunctions, (iii) isotype g-C<sub>3</sub>N<sub>4</sub>/g-C<sub>3</sub>N<sub>4</sub> heterojunctions, (iv) carbon/g-C<sub>3</sub>N<sub>4</sub> heterojunctions, (v) conducting polymer/g-C<sub>3</sub>N<sub>4</sub> heterojunctions, (vi) sensitizer/g-C<sub>3</sub>N<sub>4</sub> heterojunctions, and (vii) g-C<sub>3</sub>N<sub>4</sub>-based ternary nanocomposites.<sup>[56]</sup> According to these reports, incorporating two different catalysts together is considered as an effective method to promote charge transfer and separation when their VB and CB potentials are appropriate. Taking inorganic semiconductor/g-C<sub>3</sub>N<sub>4</sub> heterojunctions as an example, TiO<sub>2</sub> is a promising candidate to form heterojunctions with g-C<sub>3</sub>N<sub>4</sub>. It has been reported the formation of TiO<sub>2</sub>/g-C<sub>3</sub>N<sub>4</sub> heterojunction can promote its photocatalysis activity.<sup>[156, 157]</sup> Another example is the heterojunction with Metal Organic Framework (MOF) materials. As reported, it can result in the transfer of holes and electrons to the desired reactant molecules and initiation of photo-redox reactions.<sup>[158, 159]</sup> The high surface area and porosity of MOF materials can also benefit the MOF/g-C<sub>3</sub>N<sub>4</sub> heterojunction, which gives the hybrid catalyst with high surface area porous structure, improved visible light absorption and efficient charge transfer.<sup>[160, 161]</sup>

In summary, current engineering of g-C<sub>3</sub>N<sub>4</sub>-based heterojunction photocatalysts greatly help with strengthening and optimization of g-C<sub>3</sub>N<sub>4</sub> in the perspective of structure, optical properties and electronic features.

#### 1.7.4 Preparation methods

Different preparation methods usually result in different final photocatalysis performance. Therefore, exploring new synthesis strategy has become another way to improve photocatalyst.

The utilization of supramolecular assembly method is one of the novel preparation methods. A supramolecular assembly is defined as a complex of several self-assembled molecules by noncovalent bonds. Those bonds do not involve electron sharing, but rather depend on secondary electromagnetic interactions between molecules, including hydrogen bonds, dipole-dipole attraction,  $\pi$ - $\pi$  stacking, and van der Waals forces. It has become one of the most effective ways to prepare photocatalyst with a high yield.<sup>[162]</sup> One of the examples is the utilization of a cyanuric acid-melamine (CM) crystalline complex to prepare g-C<sub>3</sub>N<sub>4</sub>.<sup>[163]</sup> In this method, the new g-C<sub>3</sub>N<sub>4</sub> shows increased specific surface areas and improved photoactivity in hydrogen evolution reaction (HER) and RhB degradation.

Another method is the introduction of templates, *via* the selection of which different photocatalysts can be prepared. As for the g-C<sub>3</sub>N<sub>4</sub> synthesis, the porous templates provide material with which much higher specific surface area, porosity, and increased numbers of active sites for catalytic reactions on its surface.<sup>[164, 165]</sup> Through selection of porosity size, controllable g-C<sub>3</sub>N<sub>4</sub> can be synthesized, such as hollow g-C<sub>3</sub>N<sub>4</sub> nano spheres and 1D g-C<sub>3</sub>N<sub>4</sub>.<sup>[166-168]</sup> Another example is the templating with sulfur bubble, from which porous g-C<sub>3</sub>N<sub>4</sub> can be obtained with enhanced photocatalytic hydrogen evolution

performance.<sup>[169]</sup> Ionic liquids can be used as a soft template and also allow to tune the g-C<sub>3</sub>N<sub>4</sub> nano structure.<sup>[170]</sup>

In fact, there are several novel synthesis methods, such as liquid phase exfoliation,<sup>[134]</sup> microwave hydrothermal approach<sup>[171]</sup> and metal oxide cores<sup>[172]</sup>. All those novel methods extensively boosted the development of photocatalyst and bring more effective g-C<sub>3</sub>N<sub>4</sub>.

### 1.7.5 Surface modification

Surface modification in photocatalyst mainly refers to the act of modifying catalyst surface by bringing in functional groups or chemical substance. Based on reports, those surface functional groups prove to be an important factor in its photocatalysis performance, because the properties of these catalysts can be changed through modification process. Especially in photocatalytic CO<sub>2</sub> reduction reactions, the effects of catalyst modification seem to be significant. As CO<sub>2</sub> molecule is an acidic oxide, the modification with alkali sorbents could greatly enhance its CO<sub>2</sub> adsorption capacity.<sup>[173, 174]</sup> Moreover, surface modification can also modify the molecule structure and intrinsic electronic structure of catalysts. Those changes could lead to the variation of specific surface areas, the number of reactive sites, absorption range, conduction band position and photogenerated charge separation.

As reported, oxygen-modified g-C<sub>3</sub>N<sub>4</sub> shows larger surface areas, shifted CB position and higher charge separation effects, which greatly promote photocatalysis performance, especially in hydrogen evolution reaction.<sup>[175]</sup> The graft of azomethine ylides to g-C<sub>3</sub>N<sub>4</sub> roughens its smooth surface, broadens the light sorption range, and narrows the band gap, which provides it with better performance in the selective oxidation.<sup>[176]</sup> Surface modification of polymers by nickel oxide core-shell can greatly promote photocatalytic H<sub>2</sub> evolution activity under the light irradiation.<sup>[172]</sup>



## 1.8 Summary

In general, the development of photocatalysis has the potential to play a significant role in the new energy era, while the design and modification of photocatalyst holds the main focus in photocatalysis research. Whether a promising catalyst can be prepared, directly decides photocatalysis performance, functional use and its final application prospects.

As one of the most promising photocatalysts,  $g\text{-C}_3\text{N}_4$  has gained considerable attention. It has been extensively explored in photocatalysis applications, such as water splitting, organic pollutant degradation, and  $\text{CO}_2$  reduction. Even so, it also has its own drawbacks which inhibit its further application. Inspired by that, this thesis will mainly present and discuss the process and achievement on the preparation of some novel photocatalysts and their photocatalysis performance based on carbon nitride. These materials were all synthesized *via* the alteration of classic  $g\text{-C}_3\text{N}_4$  preparation method, like using different pre-compositions and functional group post-modification. In addition, these materials show different photocatalysis performance, which is worth to note and analyze. All the work mentioned above is finished during my Ph.D study period in Max Planck Institute of Colloids and Interfaces. The details about those interesting new photocatalysts can be found in Chapter 2, 3 and 4.

Here, at the end of the introduction, it has to be mentioned that, the most important value of these work lies in the proposal of new methods to prepare and modify photocatalysts. I hope these methods can inspire the other researchers in this area to synthesize better photocatalysts, improve the photocatalysis efficiency and finally achieve widely commercial uses.

## 2 New organic photoactive semiconducting scaffolds by supramolecular preorganization

This chapter is my original work, but was already published as Small 2016, 12 (44), 6090–6097, *New organic semiconducting scaffolds by supramolecular preorganization: dye intercalation and dye oxidation and reduction*.

### 2.1 Background and state-of-the-art

#### 2.1.1 From supramolecular assemblies to photoactive materials

As mentioned in the Chapter one, novel synthesis methods sometimes bring an unexpected improvement to photocatalysis performance. Among those advanced methods, supramolecular pre-assembly of the starting monomers seems to be a feasible way for photocatalyst preparation.

The notation “supramolecular chemistry”, focusing on chemical system, usually refers to the field of chemistry built on self-assembled molecules instead of molecules themselves. Different from traditional chemistry, it mainly works on the weaker and reversible noncovalent interactions between molecules, e.g. H-bonding, dipole-dipole attraction,  $\pi$ - $\pi$  stacking, and van der Waals forces, etc.<sup>[177, 178]</sup> In most cases, these comparatively weak forces are responsible for structure prealignment and collective properties.<sup>[179, 180]</sup> With the help of those secondary affinities among various subunits, the components can arrange themselves into new patterns with different crystal structures, electronic properties and morphologies.<sup>[178]</sup>

After its first postulation by J. D. Waals and H. E. Fischer, this concept of supramolecularity was not widely recognized by academia in the 19<sup>th</sup> century.<sup>[181]</sup> It took around a century for scientists to accept the theory that different molecules can form a defined system without covalent bonds. The discovery of H bond as well as other noncovalent bonds provided theoretical basis for this conception. Nowadays, supramolecular chemistry has already become a very important branch of chemistry as such, of which important value has been constantly excavated; covering a range from the basic understand of life science to novel synthesis methods selective "host-guest" complexes and even to molecular machinery. Since then, a bottom-up approach has been rapidly established from supramolecular to nanoscale systems, from biology, chemistry to materials science.<sup>[182]</sup>

#### 2.1.2 Photocatalysis based on supramolecular assembly

In recent years, supramolecular aggregates have been extensively introduced to prepare various materials, including photocatalyst.<sup>[163, 183]</sup> One of the most important breakthroughs is the preparation of carbon nitride based on cyanuric acid–melamine (CM) complex. In a typical reaction, equimolar amount (0.1 mol) of cyanuric acid and melamine are added in 100 mL water, and then stirred or

shaked overnight, giving the CM complex. After the heating at 550 °C, carbon nitride can be synthesized.<sup>[163]</sup> According to reports, this strategy has greatly improved the yield of carbon nitride, together with its photocatalysis performance. In fact, the utilization of supramolecular complexes provides this area with new possibilities of synthesis routines, and improved performance. Afterwards, different additives were added to the synthesis systems in attempt. It led to the formation of variety of supramolecular aggregates in various solvents, while CN materials with hollow, tube and rod-like morphologies were acquired after their calcination at high temperatures.<sup>[184-186]</sup> These new materials demonstrated higher photoactivity compared with the standard ones thanks to the local prealignment of tectons and the coupled alteration of their photophysical properties.<sup>[187, 188]</sup>

### 2.1.3 Carbon-nitrogen based materials

Carbon nitrogen materials, represented by g-CN, and nitrogen doped carbon, show excellent chemical and catalytic properties, which has attracted great attention since the beginning of 21<sup>st</sup> century.<sup>[189-192]</sup> The preference for those materials comes from their high thermal stability (at least 400 °C in air), as well as chemical stability against acid, base, and most of organic solvents and great performance as photo and electrocatalysts.<sup>[85, 193, 194]</sup> Not limited to these applications, they have also been reported with the potential to be used in other areas, such as sensing, biomedical applications, and solar energy exploitation.<sup>[195-199]</sup> This family of materials also shows promising activity in organic photovoltaics, photo/electro-catalysis, lithium ion batteries, supercapacitors, and more.<sup>[200, 201]</sup>

Even carbon nitrogen materials possess so many satisfactory properties, they are still not flawless. One of its disadvantages is the requirement of high temperature during synthesis. It is rarely reported that good photoactive materials can be prepared, employing low temperature for their synthesis.

### 2.1.4 A brief introduction to this chapter

Inspired by the excellent results of g-C<sub>3</sub>N<sub>4</sub> based on supramolecular assembly, in this chapter this method was employed to prepare new CN material. In order to modify the C/N ratio, 1,4-dihydroxy-2,5-benzoquinone (DBQ) was used to take the place of cyanuric acid (CA). A new assembled supramolecular structure and derived products are produced based on melamine and DBQ serving as the reaction precursor. When further heated at elevated temperatures, this series of products exhibit a sheet-like microstructure, because of the preorganization of the supramolecular aggregate. The morphology of these materials is so stable that two dimensional structures can be preserved even at the temperature of 800 °C. The sheet thickness, elemental composition, optical and electronic properties and photocatalytic activity can be adjusted by the calcination temperature. Among all those samples, the materials synthesized at 250 °C shows the best dye adsorption and degradation properties as a low temperature synthesized carbon nitride-based semiconducting polymer.

## 2.2 Synthesis and characterization of DBQ-M complex

All chemicals were purchased from Sigma-Aldrich. First, 492 mg melamine and 412 mg DBQ were shaken overnight in 40 mL water with a vibration speed of 350 times per minute. After that, the formed crystals were centrifuged, followed by water removal and drying at 60 °C, giving a solid powder with orange colour. This resultant supramolecular complex is named as B-DBQ-M, and the yield is about 74%.

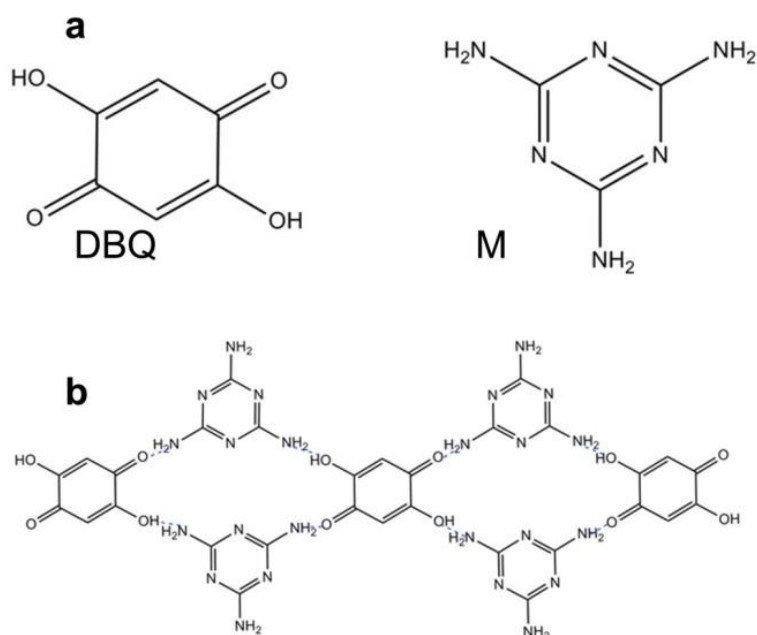


Figure 2.1 (a) The chemical formulas of two monomers; and (b) Simplified/idealized structure of the complex.

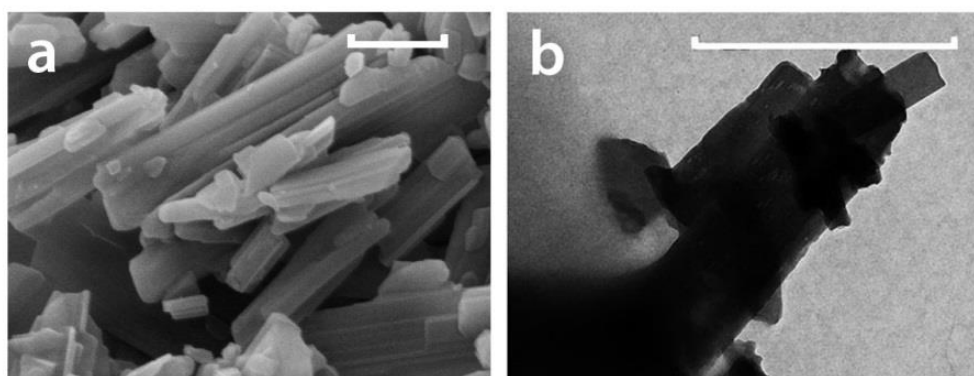


Figure 2.2 Scanning electron microscopy (a) and transmission electron microscopy (b) graphs of the complex B-DBQ-M; the scale bars are equal to 1 μm.

In order to confirm the morphology of this complex, it was first investigated by scanning electron microscopy (SEM) as well as Transmission Electron Microscopy (TEM). As shown in Figure 2.2, the

complex exhibits a plank-like morphology. The new and uniform morphology supports the view that a new supramolecular complex was aggregated.

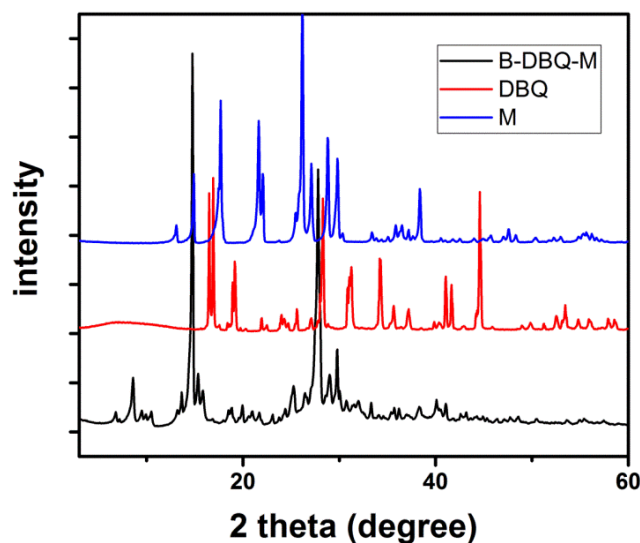


Figure 2.3 X-Ray diffraction patterns of the complex B-DBQ-M and the two monomers.<sup>[202]</sup>

The crystalline aggregates could also be proven by several other techniques. The X-ray diffraction (XRD) patterns of the complex B-DBQ-M differs from those of the monomers, especially creating new peaks in the range of  $3^\circ - 15^\circ$  (Figure 2.3). According to Bragg's law ( $2d\sin\theta = n\lambda$ ), new emerging peaks represent new distances between crystal planes, suggesting here larger structural repeats and indicating the formation of a new and ordered bimolecular crystal structure. Some peaks among them may be assigned to the repeating units within a 2D supramolecular assembly. The distance between the layers is defined by a very pronounced graphitic stacking peak at around  $28^\circ$  which corresponds to 0.328 nm. Compared with the minimal distance in carbons/graphite (0.336 nm), the lower graphitic layer distance of B-DBQ-M is remarkable, as this indicates that the layers of B-DBQ-M complex are not only bound by van der Waals interactions. Based on these results, it can be speculated that there are also strong charge polarization effects existing, which speaks for the strong interaction between the layers to enable the tight packing.

The solid state UV-vis absorption of the B-DBQ-M compared to the raw monomers further indicates that the new organization allows alternative electrons transport paths thanks to the establishment of additional electronic states (Figure 2.4a). The absorption of the complex is red shifted compared to the starting products and covers the range up to 700 nm, which can be assigned to  $\pi$ - $\pi$  stacking and intermolecular electron transitions. The formation of a hydrogen bonded complex is further evidenced by Fourier-transform infrared spectroscopy (FTIR) measurements (Figure 2.4b). The asymmetric stretching vibration of  $\text{NH}_3$  at  $3500\text{ cm}^{-1}$  in melamine disappears, while the O-H stretching vibration at  $3260\text{ cm}^{-1}$  and the C=O stretching vibration at  $1720\text{ cm}^{-1}$  of the DBQ monomers vanish (i.e. they have entered the new bonding scheme). At the same time new vibrations of intramolecular H-bonds at  $3330$

$\text{cm}^{-1}$  are formed. All the aforementioned information strongly suggest that 2,5-dihydroxy-1,4-benzoquinone and melamine successfully establish a new supramolecular structure.

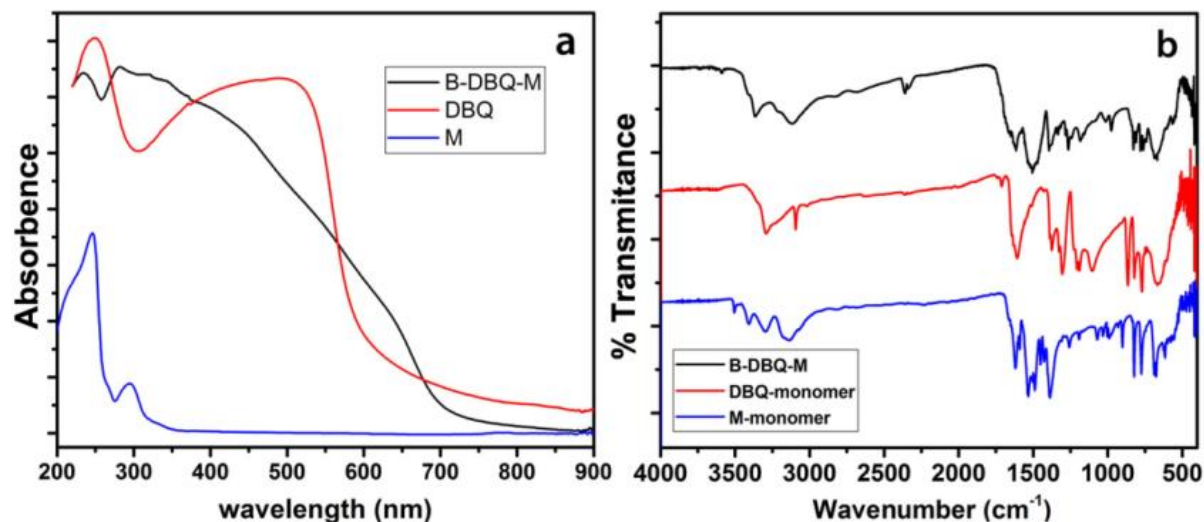


Figure 2.4 (a) Solid UV-vis absorption spectra and (b) FTIR spectra of the complex B-DBQ-M and two monomers.<sup>[202]</sup>

### 2.3 Characterization of the supramolecular assembly after condensation at different temperatures

Table 2.1. Yield and C/N ratio of the synthesized materials

Sample	Temperature (°C)	Yield (%)	C/N mass ratio
B-DBQ-M	25	74	1.104
DBQ-M-150	150	67	1.182
DBQ-M-200	200	66	1.150
DBQ-M-250	250	65	1.340
DBQ-M-300	300	59	1.573
DBQ-M-350	350	55	1.643
DBQ-M-400	400	51	1.715
DBQ-M-480	480	52	1.824
DBQ-M-550	550	47	1.904
DBQ-M-600	600	45	1.987
DBQ-M-650	650	41	2.042
DBQ-M-700	700	36	2.527
DBQ-M-800	800	37	3.176

The complex crystals were slightly ground and heated at different temperatures for 4 h. The heating rate was 2 °C per minute. The final products are named as DBQ-M heating temperature (i.e. DBQ-M 200 for one synthesized at 200 °C). The color ranges from orange *via* brown to black with increasing temperature. As shown in the Table 2.1, the yields of these materials are very high, which even accentuates the advantage of this method. This is because the utilization of its supramolecular assembly prevents melamine sublimation at elevated temperatures. The high yields emphasize the hindrance of melamine sublimation, thanks to a new, effective supramolecular hydrogen bond network.

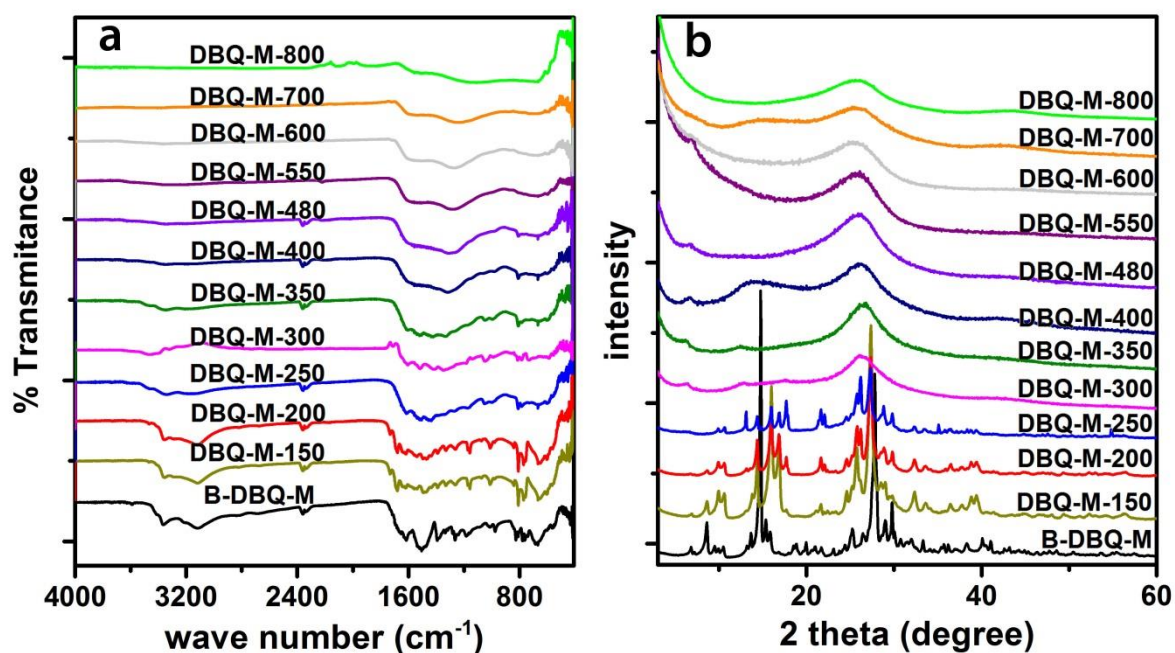


Figure 2.5 FTIR curves (a), and XRD patterns (b) of all the samples synthesized at different temperatures.<sup>[202]</sup>

With the increase of temperature, the ongoing reactions within the complex can be followed by FTIR (Figure 2.5 a). The typical vibration peaks of the melamine-DBQ complex are still visible for all samples below 250 °C. Above that temperature, the characteristic FTIR absorption peaks of the complex change into non-specific ones. First, the vibrations of intramolecular H-bonds at 3330 cm<sup>-1</sup> and the stretching modes of NH<sub>2</sub> or NH groups (at the range of 3100–3400 cm<sup>-1</sup>) disappear. The IR absorption peaks of the C–N and C=N, in the 1000–1400 cm<sup>-1</sup> and 1500–1600 cm<sup>-1</sup>, respectively, decrease with raising temperature, especially above 250 °C. Alongside, the vibration of the triazine ring at about 800 cm<sup>-1</sup> is rather stable, but gradually disappears when the temperature comes close to 550 °C. This is the known reversibility of the trimerization of nitriles and their consecutive involvement in larger aromatic structure. All these changes suggest that the monomer condensation is likely to start at a temperature around 250 °C, while ring rearrangement and carbonization sets at temperatures higher than 400 °C.



The structural consequences of this condensation/carbonization at elevated temperature were revealed by XRD measurements (Figure 2.5 b). In accordance with the results of FTIR measurements, the crystal structure altered at temperature higher than 250 °C, and new, broad peaks at 14.7° and 27.8° attributing to the in-plane and interplanar stacking of a weakly ordered polymeric structure can be observed. This reflects the dehydration condensation started at around 250 °C, while the tight stacking distance is essentially maintained. Interestingly, the distance between the layers enlarges again with further increase of the temperature, that is to say the material turns back into an ordinary carbonaceous material in further defunctionalization. It should be noticed that a new small angle peak at about 6.4° appears above 300 °C, presumably characterizing the annular condensation of the formed framework in the plane. We conclude that the specificities, due to the choice of monomers and their prearrangement, are lost above 550 °C, and only a disordered, nitrogen-doped carbon is left above this temperature.

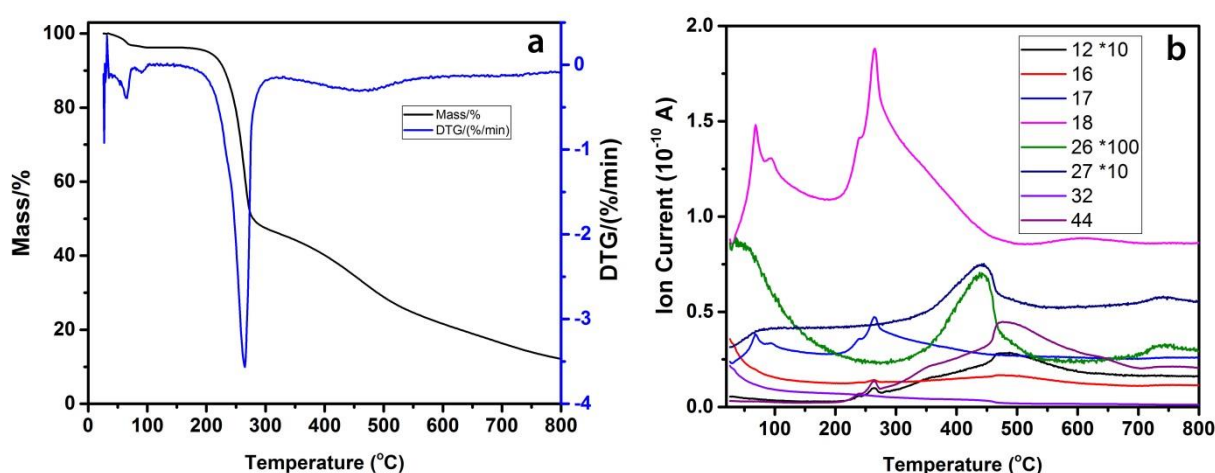


Figure 2.6 TGA curves of B-DBQ-M complex (a) and corresponding mass spectrometry (b).<sup>[202]</sup>

Further details about the transformation process are taken from elemental analysis and thermogravimetry coupled to Mass Spectrometry (TGA-MS). In Figure 2.6 a, TGA shows that the complex of melamine and DBQ loses 3.62% of its weight before 100 °C, and then keeps stable until 200 °C. This process could be referred as the release of water and adsorbed gases adsorbed to the surface of the crystals. Then a peak-like weight loss of about 50% up to 300 °C sets in accompanied mainly by elimination of water and some release of ammonia from amine hydrolysis. The second reaction is responsible for the increase of C/N ratio from 1.15 to 1.573 (stoichiometric water only elimination would result in a C/N = 1.25). This polymer intermediate is rather stable, and the rate of weight-loss slows down. At further elevated temperatures, (500 – 650 °C), the C/N ratio reaches a second plateau of stability at  $\sim 2$ , i.e. the composition is close to an intermediate already well known to be rather stable, the C<sub>2</sub>N fragments. Fragments along this process are, for instance, HCN and N<sub>2</sub>, in good agreement with the known reversible opening of the triazine ring towards nitriles.<sup>[203]</sup> Finally, at



even higher temperatures also  $C_2N$  is getting unstable, and the ratio of C and N gradually rises to 3.176 for DBQ-M-800.

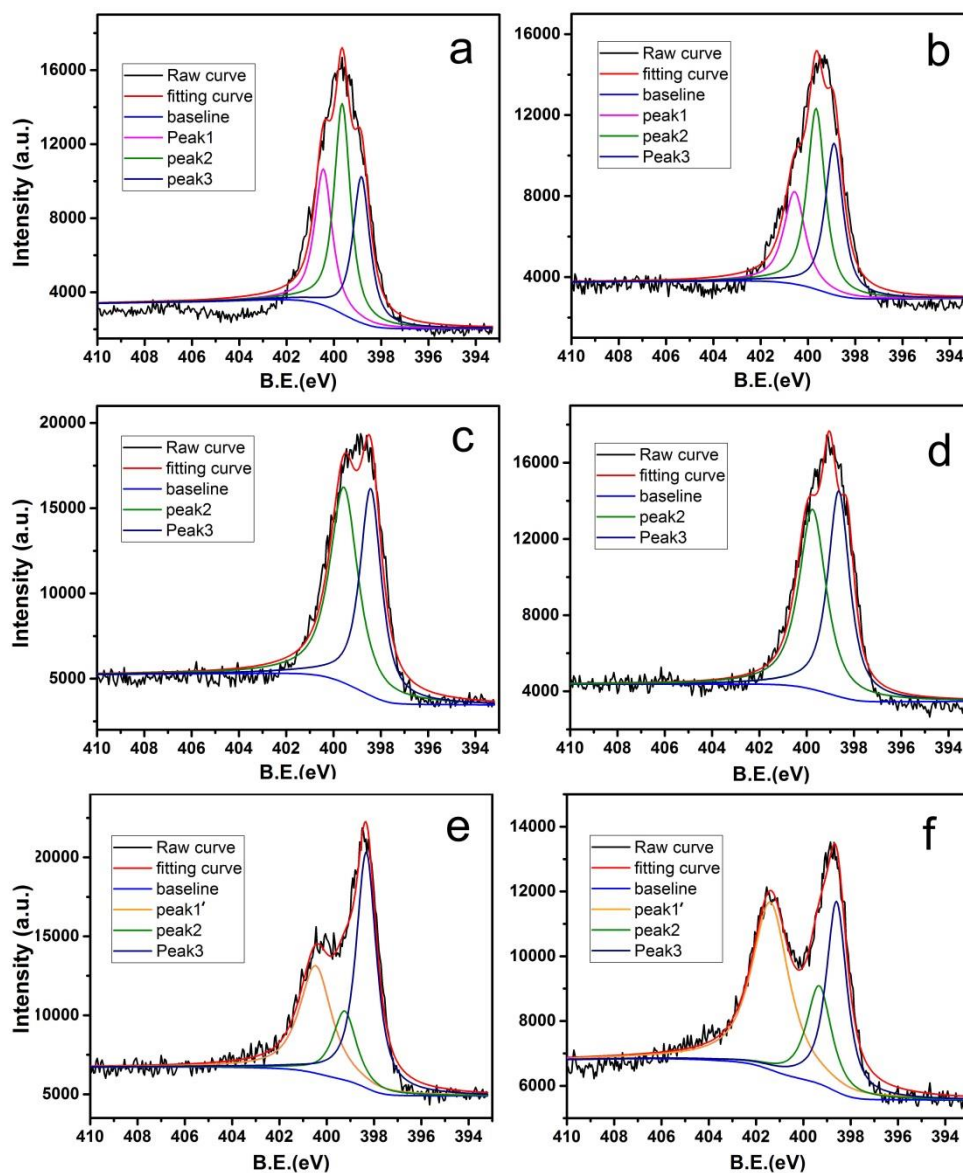


Figure 2.7 N1s XPS curves of B-DBQ-M (a), DBQ-M-200 (b), DBQ-M-250 (c), DBQ-M-300 (d), DBQ-M-550 (e) and DBQ-M-800 (f).<sup>[202]</sup>

Final details about chemical compositions and local connectivity motifs were revealed by X-ray photoelectron spectroscopy (XPS). Figure 2.7 depicts the N 1s XPS curves of the relevant stages under discussion. The N 1s signal peak of the primary B-DBQ-M could be divided into three main peaks at around 398.7, 399.7, and 400.7 eV, respectively. These three peaks can be referred as the occurrence of  $sp^2$ -nitrogen atoms in triazine ring, charge depleted amines and to partially hydrogenated N atoms of  $NH_x$  ( $x=1, 2$ ).<sup>[82, 204]</sup> While the material prepared at 200 °C keeps these nitrogen species, the dehydration condensation reaction at around 250 °C eliminates the peak at 400.7 eV, as found in Figure 2.7 c and d. In agreement with all other data, condensation obviously removes the free H-

bonded nitrogen species and created nitrogen conjugation. This polymer-like structure obviously starts to decompose due to the ring rearrangements of triazine at  $> 350^\circ$  and the changes in structure can be well characterized by the sample condense at  $550^\circ\text{C}$ . The new peak at  $401\text{ eV}$  reveals the gradual appearance of quaternary nitrogen, reflecting the onset of extended carbonization. All these data nicely support the trends observed in elemental analysis and the other techniques.

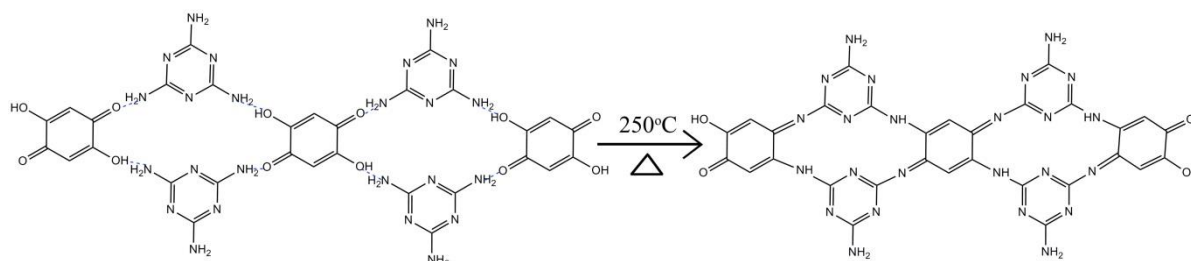


Figure 2.8 A simplified/idealized reaction scheme during heating at  $250^\circ\text{C}$  in agreement with the found compositions and mass eliminations.

From all these data we deduce that the most interesting product is the polymer product formed at around  $250^\circ\text{C}$ . The product of this temperature just goes through dehydration within supramolecular and major emphasis in all further application experiments is put on that. A possible schematic presentation of the original complex and a potential condensation path occurring at the stepwise water loss around  $250^\circ\text{C}$  is illustrated in Figure 2.8.

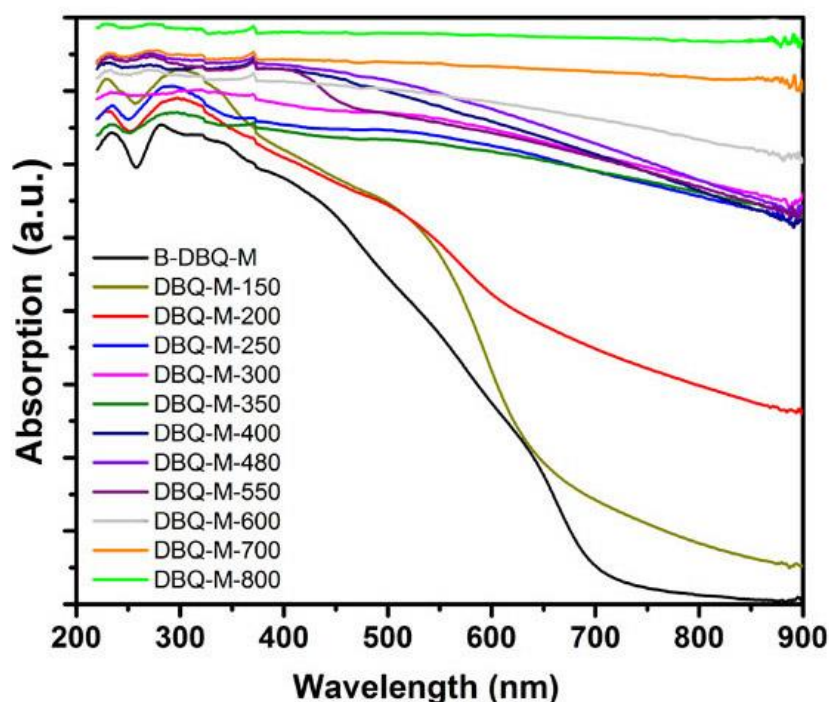


Figure 2.9 UV-vis absorption spectra of all the samples synthesized at different temperatures.<sup>[202]</sup>

Interestingly, these structural and compositional considerations are also reflected in the optical properties. Condensation leads to a red-shift of the absorption spectra of the synthesized materials (Figure 2.9) which has already fully developed at 250 °C, and the systems are good absorbers for the complete visible spectrum. At higher temperatures analytical data suggested C<sub>2</sub>N formation and the further loss of nitrogen at higher temperatures leads only to black carbon powder, that is either small band gap semiconductors or semi-metals are acquired.

Table 2.2 Surface area and Zeta potential of the synthesized materials

Sample	Specific surface area (m <sup>2</sup> /g)	Zeta potential (mV)
B-DBQ-M	12	-26.6
DBQ-M-150	20	-27.6
DBQ-M-200	23	-34.7
DBQ-M-250	20	-32.5
DBQ-M-300	23	-30.4
DBQ-M-350	22	-30.1
DBQ-M-400	26	-26.3
DBQ-M-480	50	-25.0
DBQ-M-550	80	-25.4
DBQ-M-600	110	-24.8
DBQ-M-650	170	-25.7
DBQ-M-700	180	-24.9
DBQ-M-800	126	-19.6

To relate the following adsorption and photocatalytic experiments, specific surface areas of the resulting samples were tested by using N<sub>2</sub> adsorption/desorption at 77 K (table 2.1). The surface areas of samples obtained below 450 °C are generally within 16-30 m<sup>2</sup>/g. For the materials at higher temperatures, the surface areas increase to 80 m<sup>2</sup>/g for DBQ-M-550 reaching up to 170 m<sup>2</sup>/g for DBQ-M-700 and 120 m<sup>2</sup>/g for DBQ-M-800. The low surface area of low temperature product proves the assumption above, that this series of materials are two-dimensional and without pronounced accessible porosity. Most of the N<sub>2</sub> adsorption comes from surface adsorption of these thin sheet-like objects. The zeta-potentials of all these structures are negative in pure water (see Table 2.2), suggesting that the surfaces are rich in acidic OH-groups (as cyanuric acid), generated by surface hydrolysis of amine groups. This is important for the further dye sorption and degradation analysis.

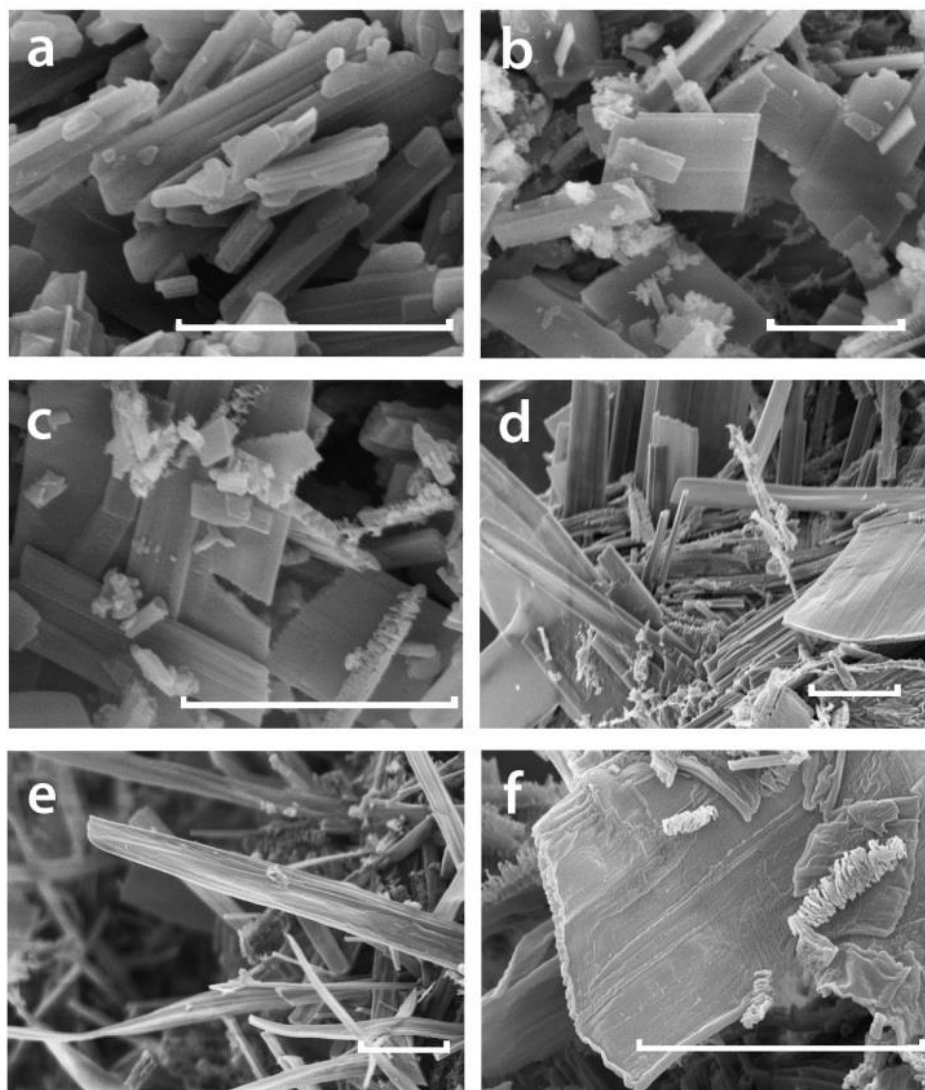


Figure 2.10 SEM images of B-DBQ-M (a), DBQ-M-200 (b), DBQ-M-250 (c), DBQ-M-300 (d), DBQ-M-550(e) and DBQ-M-800 (f). The scale bars are equal to 3  $\mu\text{m}$ .<sup>[202]</sup>

The morphology of the complex as well as the resulting materials was investigated by scanning electron microscopy (SEM). As shown in Figure 2.10, all the materials form stacked sheet structures, and this morphology remains unchanged, even when heated to 800 °C. This clearly indicates that no melting is involved in the process, and that the primary supramolecular preorganization influences all products throughout condensation reaction. The most significant variation amid those samples lies in the thickness of these sheet-like structures. With the raise of temperature, the sheets tend to become thinner, less smooth and expose more wrinkles. This can also be well observed from the Transmission Electron Microscopy (TEM) images (Figure 2.11 (a-f)) in which the paper-like structure tends to be more transparent at higher calcination temperatures, typical for the thickness declining to a few nanometer. We deduce that the condensation progresses *via* layer delamination, potentially in surface layers peeling of the primary crystallites.

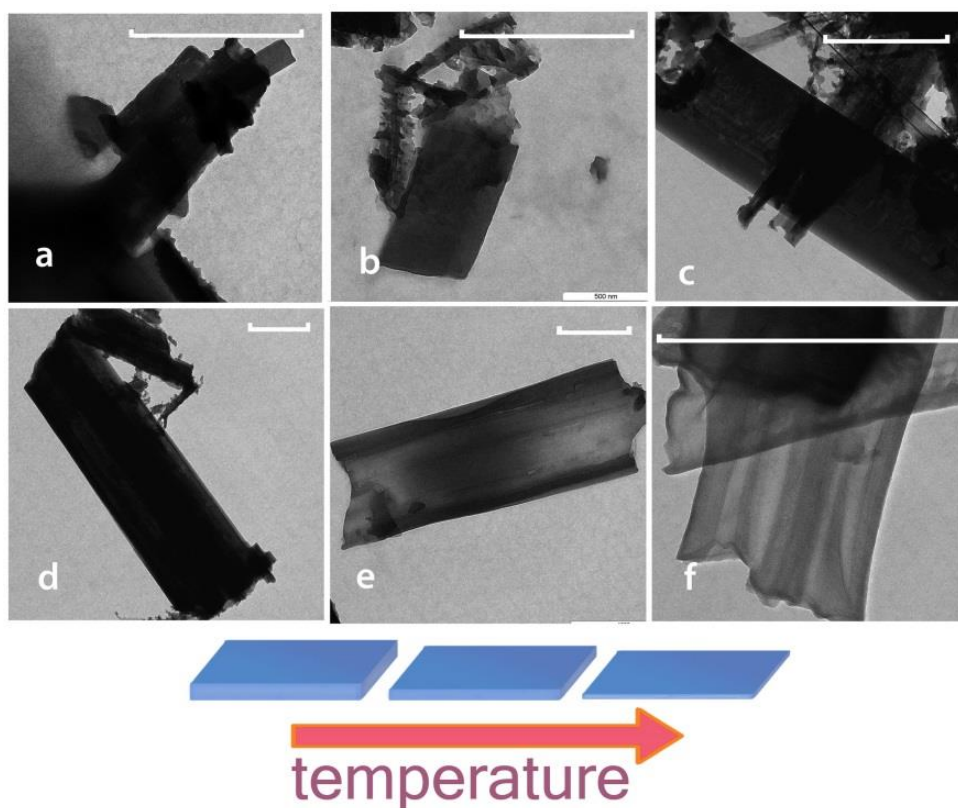


Figure 2.11 TEM images of B-DBQ-M (a), DBQ-M-200 (b), DBQ-M-250 (c), DBQ-M-300 (d), DBQ-M-550 (e), and DBQ-M-800 (f). The scale bars are equal to 1  $\mu\text{m}$ .<sup>[202]</sup>

#### 2.4 Photochemical performance of DBQ-M materials

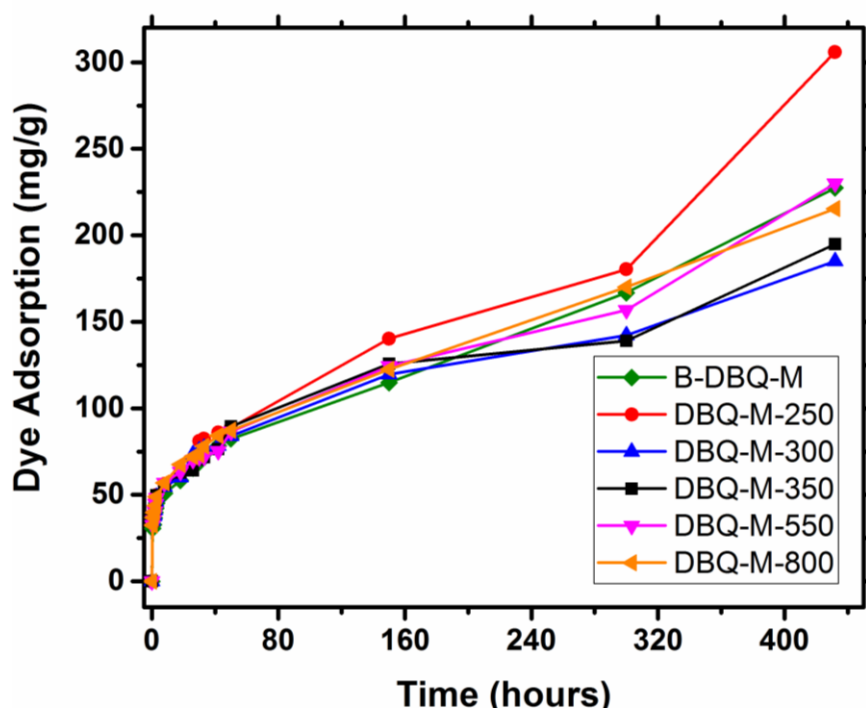


Figure 2.12 Methylene Blue adsorption curves of DBQ-M materials with time.

Degradation of organic substances is an important method to assess the activity of photocatalysts. Here, dye degradation was employed to show the photocatalysis performance of DBQ-M materials. As the materials in this work are all with negative charges, cationic methylene blue (MB) was selected as a model adsorbent and pollutant and both MB adsorption and photodegradation experiments were measured.

Before the degradation experiment, the adsorption of MB was measured first. In the dye adsorption experiment, MB (Methylene Blue) solution was prepared in advance from deionized water (100 mL) and solid MB (10 mg). The pH of this MB solution is about 7.5. For a typical dye adsorption measurement, about 5 mg DBQ-M-materials were added into 20 mL MB solution ( $100 \text{ mg L}^{-1}$ ). After stirring in the dark for a defined time, the remaining concentration of MB was calculated by its absorption at 664 nm. After two days, almost 80% of MB was successfully adsorbed to the materials. To our surprise, this was followed by a slower but constant adsorption for at least two weeks. Amid all the materials, DBQ-M-250 exhibits the highest MB adsorption capacity, about  $95 \text{ mg g}^{-1}$ , while DBQ-M-350 can take up  $65 \text{ mg g}^{-1}$  in 2 days. These are definitely not saturation values, as after an exponential type decreases, the second much slower process sets in.

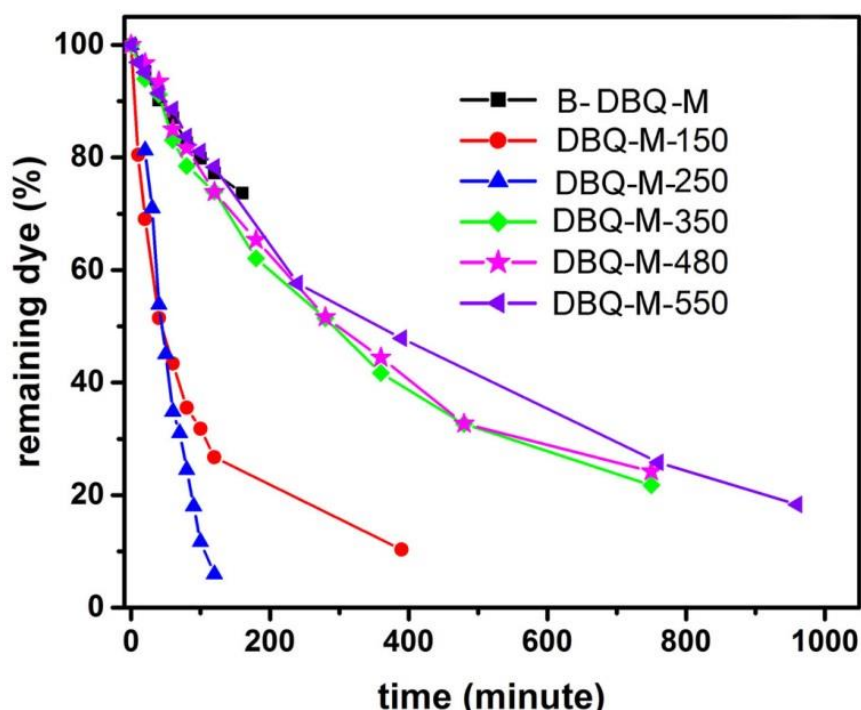


Figure 2.13 Photochemical degradation curves of MB with different catalysts.

For the photodegradation test, 5 mg of the photocatalyst was dispersed in 20 mL water with 0.02 mg MB. After saturation in the dark for 2 days, the reaction system was illuminated by 50 W LED light with constant stirring. (Figure 2.12). Dividing the available surface area by the number of adsorbed dye molecules gives a dye footprint of  $0.12 \text{ nm}^2$ , i.e. a much too small value. This and the very special adsorption kinetics clearly point to the intercalation of the dye within the layered polymer structure:



the dye is delaminating the species while adding between the layers. This of course is interesting, as it points to a potential additive supported delamination and the coupled processing of these two-dimensional polymers.

As the polymers are conjugated, stable semiconductors, their chemical photo activity was tested by dye degradation experiments under visible light. In the dye degradation experiment, MB (Methylene Blue) solution was the same with MB adsorption experiments. After stirring in the dark for 12 h, the remaining concentration of MB in solution was calculated by its absorption at 664 nm. Among all the different condensation stages, the polymer-like, DBQ-M-250 demonstrates the best photodegradation performance. Within 120 min, 90% of the dye was degraded, while the other materials show only inferior performance (Figure 2.13 ).

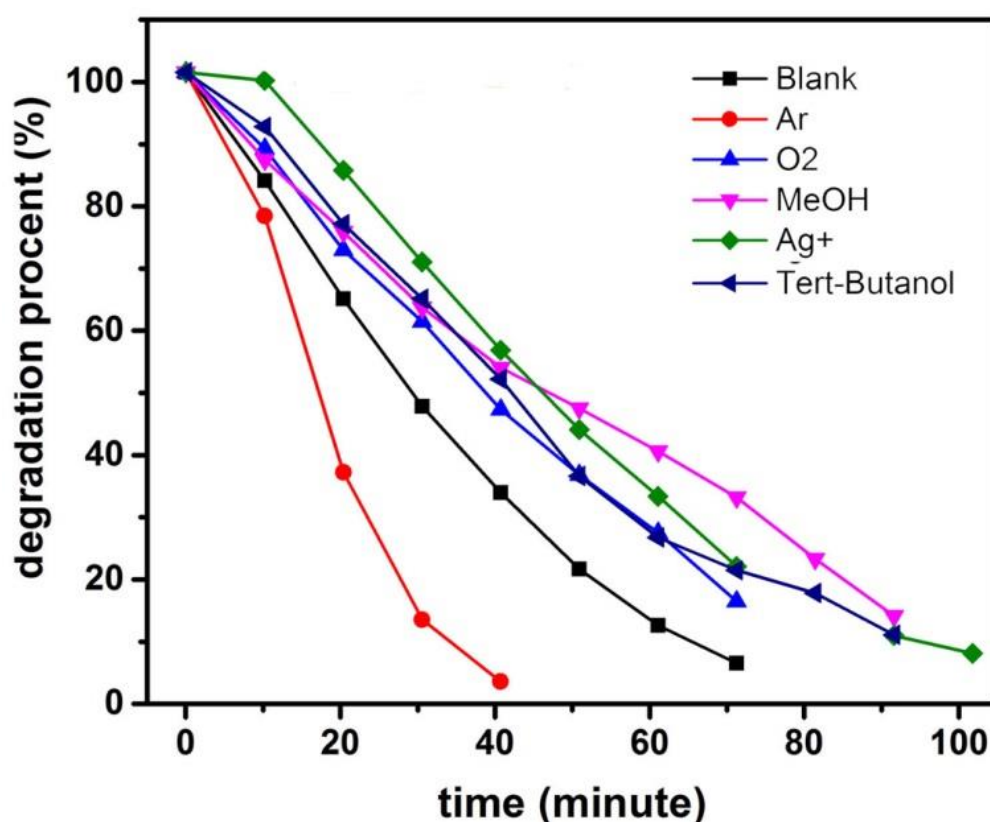


Figure 2.14 Photochemical degradation curves of MB with DBQ-M-250 as well as different additives.<sup>[202]</sup>

In order to elucidate the mechanism of MB degradation, it is necessary to affirm whether the dye degradation occurs *via* photogenerated holes or by electron transfer. Thus, we measured the photodegradation by DBQ-M-250 (with a 100W LED light) in the presence of hole and electrons acceptors such as methanol, *tert*-butanol, AgNO<sub>3</sub>, and under Ar or O<sub>2</sub> environment to unveil the possible mechanism (Figure 2.14).

Among them,  $\text{Ag}^+$  and oxygen can capture electrons first, while methanol and *tert*-butanol act as hole scavengers. The introduction of 0.1 mL 0.1 mol L<sup>-1</sup>  $\text{Ag}^+$  resulted in a significant decline of the photo degradation process; similarly the degradation process was inhibited by the introduction of oxygen. On the contrary, the flushing with the inert Ar accelerated the photodegradation rates, due to the removal of dissolved oxygen. These results strongly suggest that the reduction of MB under illumination plays a significant role in photodegradation, i.e. the positive MB is turned into the non-coloured leuco-methylenblue. On the other hand, with methanol inside, the rate of degradation has been reduced to around 75 % of the genuine experiment, and also *tert*-butanol leads to a significant decline of dye degradation. These results above imply that these hole scavengers probably competes in the hole combination position with dye molecules, i.e. the dye is not only photoreduced, but also photooxidized. With standard assays, we could neither detect the production of oxygen,  $\text{H}_2\text{O}_2$  or OH-radicals; thus MB is the only possible sink of the generated holes. Overall, this means that the surface bound cationic MB both take up the electron and holes, however at different sites. In other words, both dye decoloration mechanisms are active at the same time.

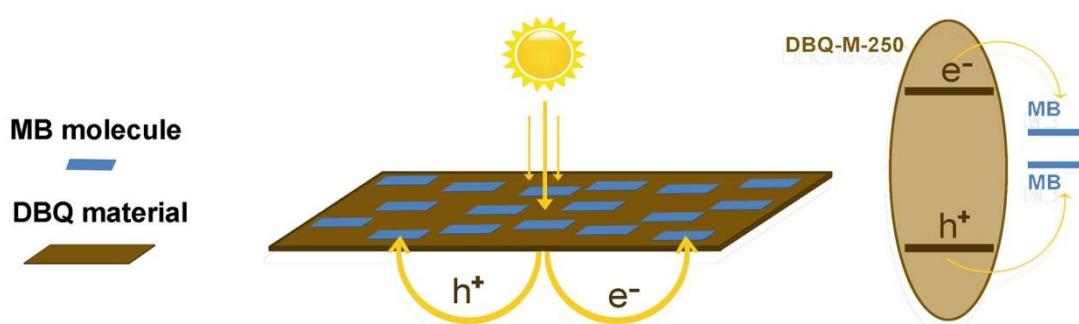


Figure 2.15 The possible MB degradation mechanism of degradation.<sup>[202]</sup>

All those results nicely illustrate that the two-dimensional condensation polymer synthesized at 250 °C is an active photocatalyst for both photooxidation and photoreduction, while certainly Coulomb interaction and the coupled charge transfer interaction to the electron rich materials surface promotes the electron transfer in absence of any metal center. (Figure 2.15)

## 2.5 Conclusion

By employing the supramolecular crystals of melamine and 2,5-dihydroxy-1,4-benzoquinone (DBQ) for monomer prealignment, photoactive organic solid state materials with good adsorption properties were formed at condensation temperatures as low as 250 °C. The sheet-like morphology of the starting assembly can be preserved throughout all steps even up to a final carbonization temperature of 800 °C, while the layer thickness and the C/N ratio change, covering thus the range from polymeric-like materials to ordered carbon–nitrogen frameworks up to nitrogen doped carbon. The synthetic path was studied with a variety of techniques, showing a clear transition from the supramolecular organization



with crystal-like order into a condensed oligomeric or polymer structure from temperature above 250 °C.

Especially the polymer structure gained at 250 °C turns out to be very effective in dye adsorption, while the amounts of dye as well as the special kinetics point to dye intercalation between negatively charged layers. With methylene blue as a model compound, it was shown that the material performs dye reduction photochemically with visible photons, while at the same time the photogenerated holes oxidize the dye towards small molecular fragments. This is one of the very rare reported cases where a simple system can avoid sacrificial agents as well as the presence of oxygen, i.e. both hole and electron are used for a meaningful photochemical reaction.

We believe that this synthesis strategy can lead to the synthesis of other photoactive carbon-nitrogen based polymers and frameworks with high photocatalytic activity at condensation temperatures lower than the synthesis of the current reference material, carbon nitride.

### **3 1D photoactive semiconductors from chlorine substituted supramolecular assemblies and their improved photocatalytic performance**

This chapter is my own original work, but was already published in *Journal of Materials Chemistry*, 2017, 5, 18502-18508, *Surface polycondensation as an effective tool to activate organic crystals: from “boxed” semiconductors for water oxidation to 1d carbon nanotubes*.

#### 3.1 Background and state-of-the-art

##### 3.1.1 Energy and oxygen evolution reaction

This chapter is about the generation of hydrogen within photosynthetical water splitting schemes. As discussed in the general introduction, it is important for human beings to seek for new and environmentally-friendly substitutes for fossil fuels, like hydrogen energy made by sunlight.<sup>[205, 206]</sup> Water, as the most wide hydrogen compound in the world, is the ideal hydrogen production source with no doubt. It is a promising method to product H<sub>2</sub> by light-driven water splitting, especially considering the abundance of solar radiation.<sup>[207, 208]</sup> In the water splitting reaction, a water molecule is decomposed into hydrogen and oxygen while transferring four electrons. Compared with hydrogen production, the oxygen evolution reaction (OER) is considered to be more challenging, because this reaction is sluggish in kinetics and it is hard to transfer four electrons and four protons at the same time.<sup>[209]</sup> Therefore, currently the limiting factor for the whole photo-induced water splitting cascade mainly lies in the efficiency of OER and the corresponding research for better oxygen generating system plays a core part in artificial photosynthesis.<sup>[210]</sup>

In order to promote OER efficiency, scientists all over the world made huge efforts to prepare and modify photocatalysts in recent years. As reported, diverse carbon nitride based materials (referred here as g-CN), sometimes coupled to earth-abundant co-catalysts, showed the potential to produce oxygen under illumination with visible light.<sup>[153, 211, 212]</sup> For instance, the integration of cobalt oxide within graphitic carbon nitride was reported to be an effective method to improve the photocatalytic oxygen evolution process from water.<sup>[213]</sup> The nanocomposite of carbon nanodot–carbon nitride (C<sub>3</sub>N<sub>4</sub>) was also reported as photocatalyst for water splitting, with partly impressive performance.<sup>[213, 214]</sup> Because of those outstanding results discussed above, it is reasonable to believe further variations of catalysts could bring more improvement in oxygen evolution reaction, such as the modification of electronic structures, local order, and nanotexture.

### 3.1.2 Photocatalyst modification *via* monomer substitute

As well discussed in the last chapter, supramolecular method is a feasible and effective way to prepare g-CN materials by effective organization of starting co-monomers and this leads to impressive results.<sup>[215-217]</sup> g-C<sub>3</sub>N<sub>4</sub> can be prepared in this method with cyanuric acid (CA) and melamine (M) as the initial monomer. A series of 2D page-like materials (DBQ-M) could be synthesized *via* supramolecular poly-condensation at different temperatures by starting with melamine (M) and 2,5-dihydroxy 1,4-benzoquinone (DBQ), instead of M and CA as monomer. As demonstrated in the former chapter, this series of g-CN materials shows the possibility to obtain photoactive organic frameworks by a similar construction principle at relatively low condensation temperatures (~250 °C).<sup>[202]</sup> Those materials varied from supramolecular assembly, polymer frameworks to carbon materials with the increase of temperature. Even when synthesized at comparatively low temperature where the polymerization reaction just sets in, the material DBQ-M-250 shows good photocatalytic activity in dye degradation. Just through a simple monomer substitute from cyanuric acid to DBQ, the supramolecular complex as well as resulting condensation products exhibit very different properties. It makes this method promising to yearn for further monomer modifications.

According to previous reports, one-dimensional (1D) semiconductor materials are usually favored and show satisfying performance in energy conversion, because it facilitates quantum particle transmission and localizes consecutive photooxidation/photoreduction at different ends of the structures.<sup>[132]</sup> Thus, it is meaningful to search for similar one-dimensional photocatalysts, especially by modifying the classic monomer to improve its photoactivity. The geometry structure of a supramolecular assembly is strongly tied to the functional groups of monomers and the interaction between them. This makes it possible to change the geometry structure from 2D to 1D by adding some special functional side groups on the starting monomer of DBQ-M materials. In fact, halogen atoms can form secondary interaction with amino groups.<sup>[218, 219]</sup> Apart from that, as an electron withdrawing group, the introduction of halogen would significantly increase the acidity of hydroxyl group nearby, which may lead to more directional growth. Inspired by the information above, we decide to use chloranilic acid (CLA) instead of DBQ in the supramolecular complex, hoping to obtain one-dimensional materials with better photocatalytic activity.

### 3.1.3 Brief introduction to this chapter

In this chapter we present a new series of materials based on the supramolecular alignment of melamine (M) and chloranilic acid (CLA). Those materials range from organic crystals and cross-linked polymer semiconductors at lower calcination temperatures to semimetals at higher temperatures. Different from the morphology of DBQ-M materials, this series of materials exhibits a wire-like morphology, which can be maintained up to 800 °C. Similar with DBQ-M materials, the C/N ratio increases with condensation temperature. These materials show good photoactive performance in

methylene blue (MB) and rhodamine B degradation. Among this series of materials, M-CLA-250 shows unexpected high photocatalysis performance in both RhB degradation and even in oxygen evolution reaction.

### 3.2 Synthesis and characterizations of M-CLA complex

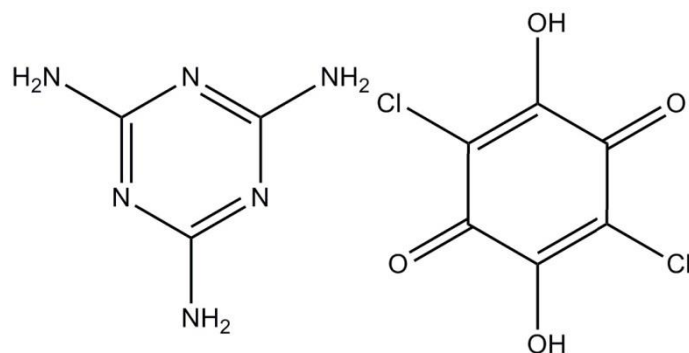


Figure 3.1 Structural formulae of monomers.

All chemicals in this experiment were purchased from Sigma-Aldrich Inco without further treatments. The molecular structures of the two monomers are depicted in Figure 3.1. First, 492 mg melamine (M, 3.9 mmol) and 408 mg chloranilic acid (CLA, 3.9 mmol) were mixed together in 40 mL water and shaken overnight with a vibration speed of 350 times per minute. After overnight crystallization, the liquid changed color to purple while orange crystals precipitated. Then, the formed crystals were centrifuged with a speed of 8000 r/min, and fully dried at 60 °C. Finally, an orange solid powder is obtained and named as B-M-CLA. The yield of this supramolecular may change with the input ratio of CLA and M (shown in Table 3.1), and the yield reaches its highest point of 99% when the ratio of CLA and M is 1:2. Thus, the intramolecular ratio between CLA and M could be safely assumed to be 1:2.

**Table 4.1** the yield of B-M-CLA with different CLA/M molar ratio

CLA (mg)	M (mg)	molar ratio of CLA:M	Yield
408	82	3:1	37%
408	123	2:1	49%
305	246	3:4	89%
204	246	1:2	99%
153	367	1:4	48%
108	367	1:6	24%

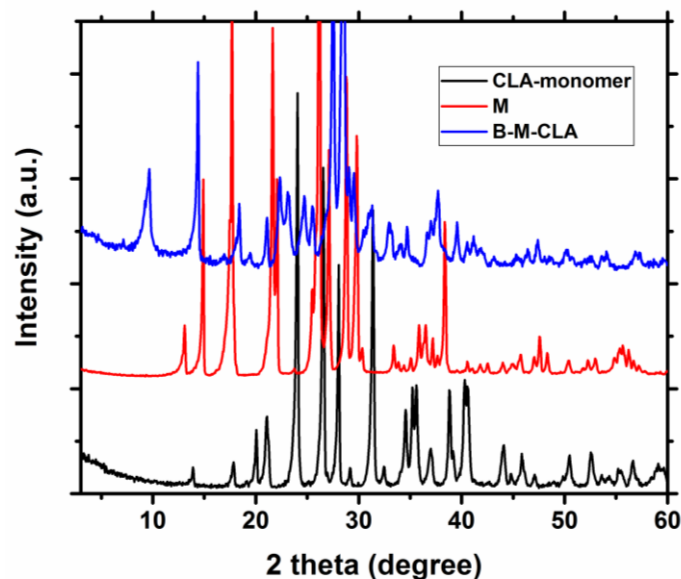


Figure 3.2 XRD patterns of the B-CLA-M complex and the two starting raw monomers.<sup>[220]</sup>

As a new and distinct entity, the formation of B-CLA-M supramolecular aggregate is identified with several characterizations methods. In Figure 3.2, the XRD pattern of B-M-CLA has completely changed from two monomers, especially in the range of small angles. There are almost no overlapping peaks at  $2\theta < 20^\circ$  between the complex and monomers. These differences indicate the existence of new larger repeat units within the highly ordered crystal structure. In the XRD pattern of B-CLA-M complex, there are two strong and sharp peaks at  $26.5^\circ$  and  $28.0^\circ$  respectively, which may be relevant to the later condensation and electronic interactions. Through calculation, the positions of these peaks correspond to a graphitic d-spacing of 0.335 nm and 0.328 nm, respectively. Compared with the d-spacing of graphite (0.336 nm), these tighter structures indicate the strong donor-acceptor charge interaction between different crystal layers.

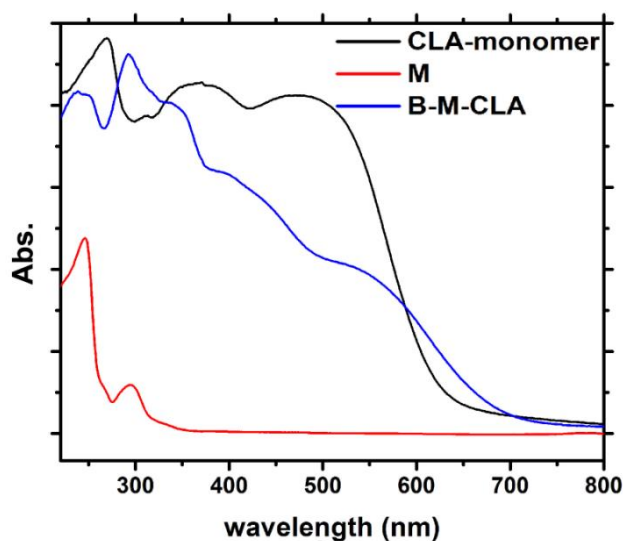


Figure 3.3 Solid UV-vis absorption spectra of the complex and two raw monomers.<sup>[220]</sup>

Similar to the characterization of B-DBQ-M, the solid B-M-CLA complex as well as monomers were measured by UV-vis absorption. As shown in Figure 3.3, there are significant differences in absorption curve between the complex and two monomers. The difference is extremely significant in the range of 400–700 nm, where an enhanced absorption and a red-shift of the key absorption are observed. The huge difference in this range reflects the appearance of better electron delocalization and polarization within the complexes. Because of the pre-organization of the two monomers, the noncovalent interactions, including H-bridges and the tight mutual packing with extended  $\pi$ - $\pi$  stacking, leads to interlayer electronic transitions and a joint electronic system, which greatly increase its electronic conductivity. Within this joint electronic system, an organic crystalline semiconductor was constituted with two monomers as very stable building units, already prior to condensation.

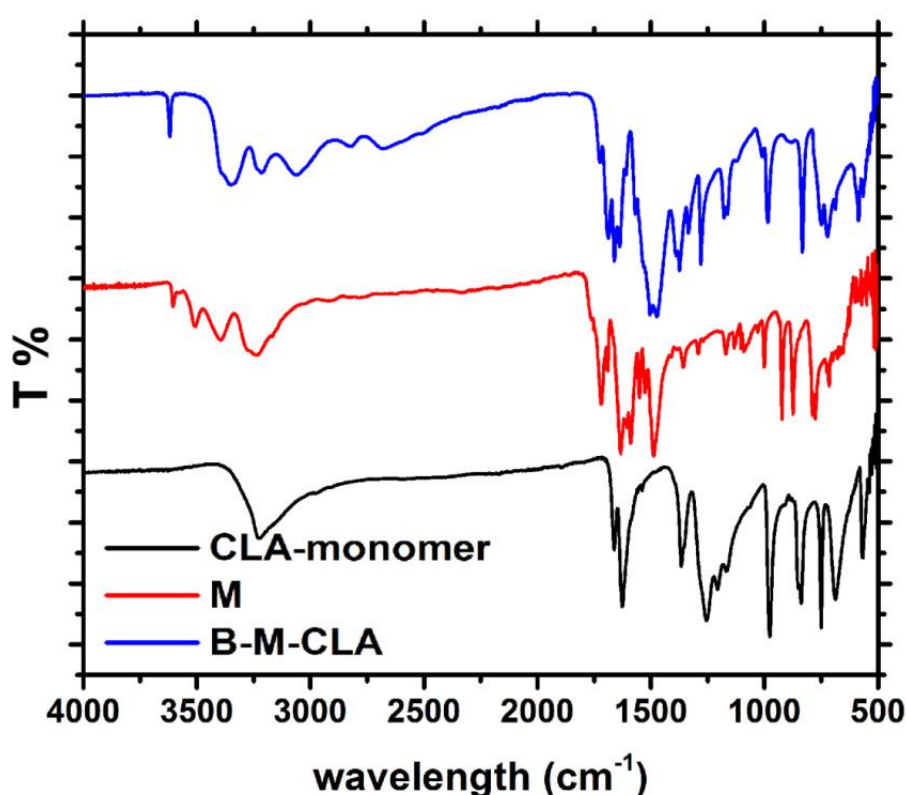


Figure 3.4 FTIR spectroscopy spectra of the complex and two raw monomers.<sup>[220]</sup>

The formation of B-CLA-M aggregate is also proven with Fourier Transform infrared spectroscopy (FTIR) measurements, as shown in Figure 3.4. First, for the complex, some characteristic absorption peaks of CLA disappear during the supramolecular formation, e.g. the phenol C-OH stretching vibration at 1260-1180  $\text{cm}^{-1}$  and the C=O stretching vibration at 1725-1705  $\text{cm}^{-1}$ . The disappearance of these peaks can attribute to the interaction with melamine. Similarly, in the FTIR spectra of B-CLA-M there is also no N-H stretching (at around 3500  $\text{cm}^{-1}$ ) vibration of the  $\text{NH}_2$  group. These disappearances of the functional group stretching vibration imply that they are strongly involved in the newly formed structure. It further indicates that H-bonds are established between amino groups and hydroxyl (or carbonyl) groups, which constitute the supramolecular assembly. Consistent with the

above statement, new peaks are observed at around  $3700$  and  $3330\text{ cm}^{-1}$ , indicating new vibrations of intramolecular H-bond. In addition, as reported,  $-\text{Cl}$  can interact weakly with the amino group of melamine. In Figure 3.4, the C-Cl stretching of CLA monomer is found at around  $600\text{ cm}^{-1}$ , which is clearly weakened in the spectrum of the complex. This proof shows that  $-\text{Cl}$  also interact with  $\text{NH}_2$  group, resulting in additional non-covalent bonds. All the information above refer to the possibility that noncovalent interaction is established between two monomers and that the supramolecular structure is successfully formed.

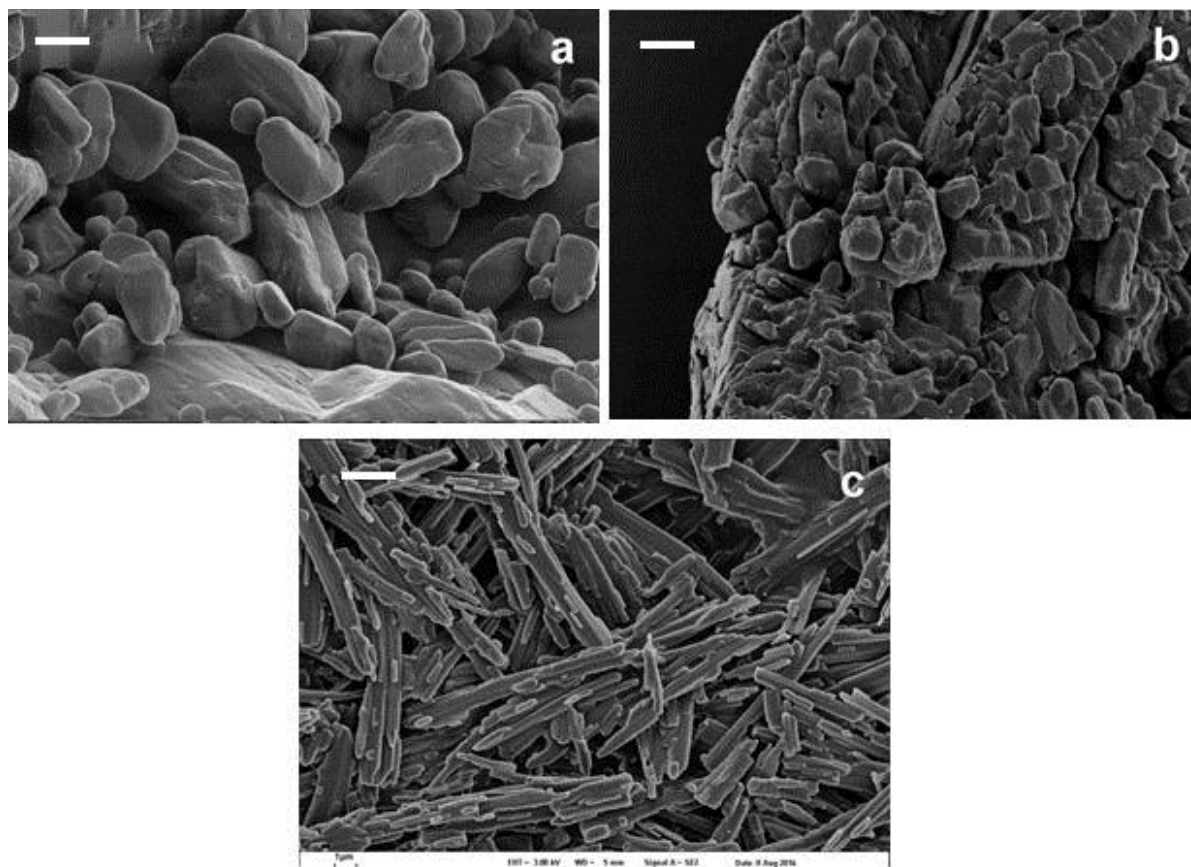


Figure 3.5 SEM images of monomer melamine (a), chloranillic acid (b) and the complex of B-CLA-M (c). All the white scale bars are equal to  $2\text{ }\mu\text{m}$ .<sup>[220]</sup>

In fact, there are also other more intuitive ways to show the formation of CLA-M supramolecular complex. The comparison SEM photographs of the monomer and the complex can clearly support a structure change as shown in Figure 3.5. Before and after the recrystallization, the morphology changes from an irregular bulk structure into stick-like structures. This could be considered as a proof about formation of the new complex and the interaction between the monomers.

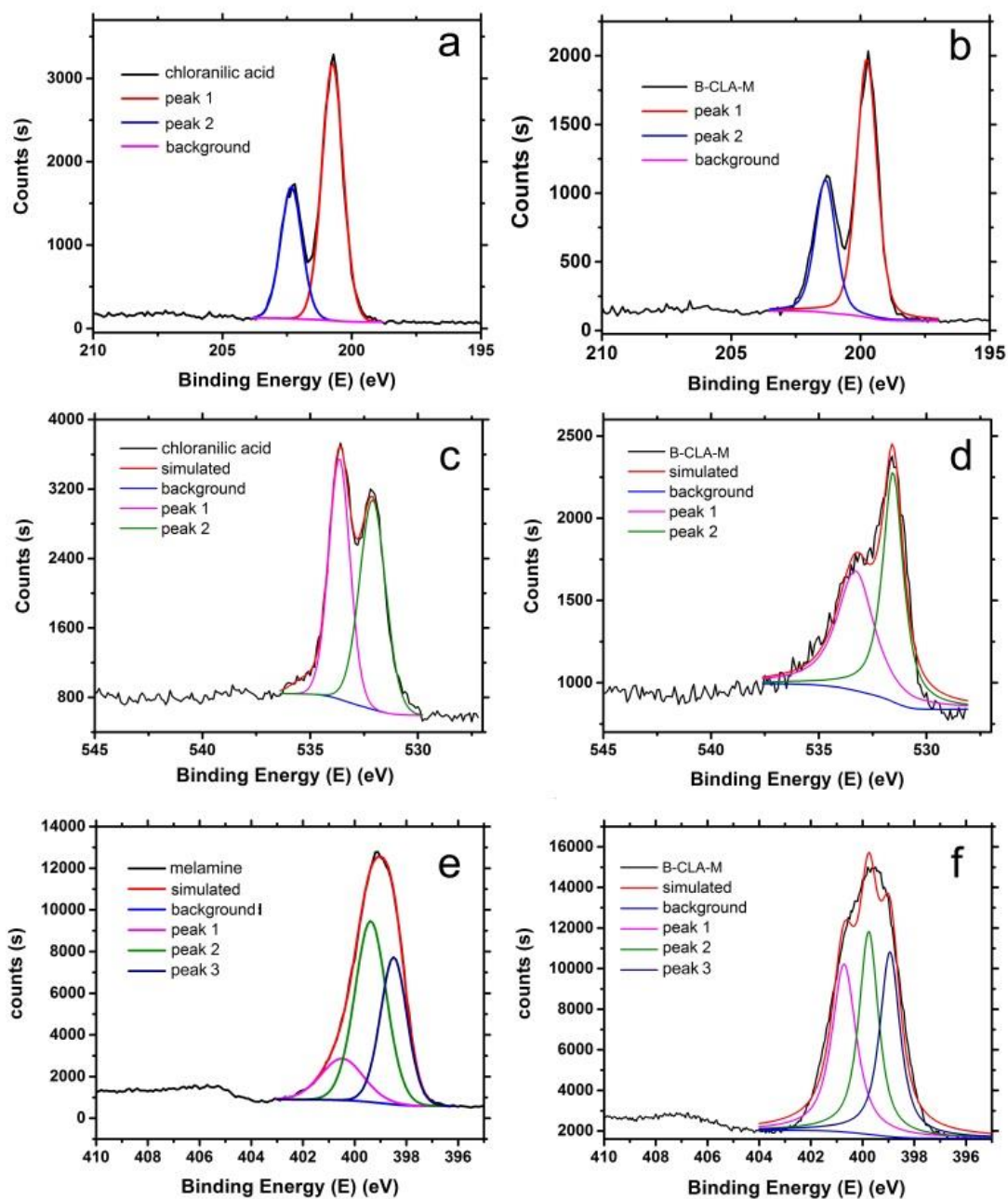


Figure 3.6 Cl 2p XPS curves of chloranilic acid (a) and the complex B-CLA-M (b); O 1s XPS curves of chloranilic acid (c) and the complex B-CLA-M (d); N 1s XPS curves of melamine (e) and B-M-CLA (f).<sup>[220]</sup>

In addition, X-Ray photoelectron spectroscopy (XPS) can also be used to elucidate the forming of supramolecular complex (B-M-CLA). As shown in Figure 3.6, the binding energies of N, O and Cl have been adjusted after the formation of the B-M-CLA complex. First, the Cl 2p peaks of the complex experience an obvious shift, compared with chloranilic acid. They varied from 202.5 and 200.6 eV to 201.7 and 199.8 eV, which just correspond to



the interaction between Cl and NH<sub>2</sub> groups.<sup>23</sup> In Figure 3.6 c and d, the O 1s binding energy spectra at 533.5 eV (C=O bond) is also significantly moved during the formation of supramolecular aggregates. This variation implies the strong hydrogen bond interaction between C=O and NH<sub>2</sub> group. This inference can be proved by the N 1s peak as well, whose position is shifted to higher binding energy area. This is because the electro density around N decreases during supramolecular formation, and transfers to the surrounding of O atom of chloranilic acid.<sup>[221]</sup>

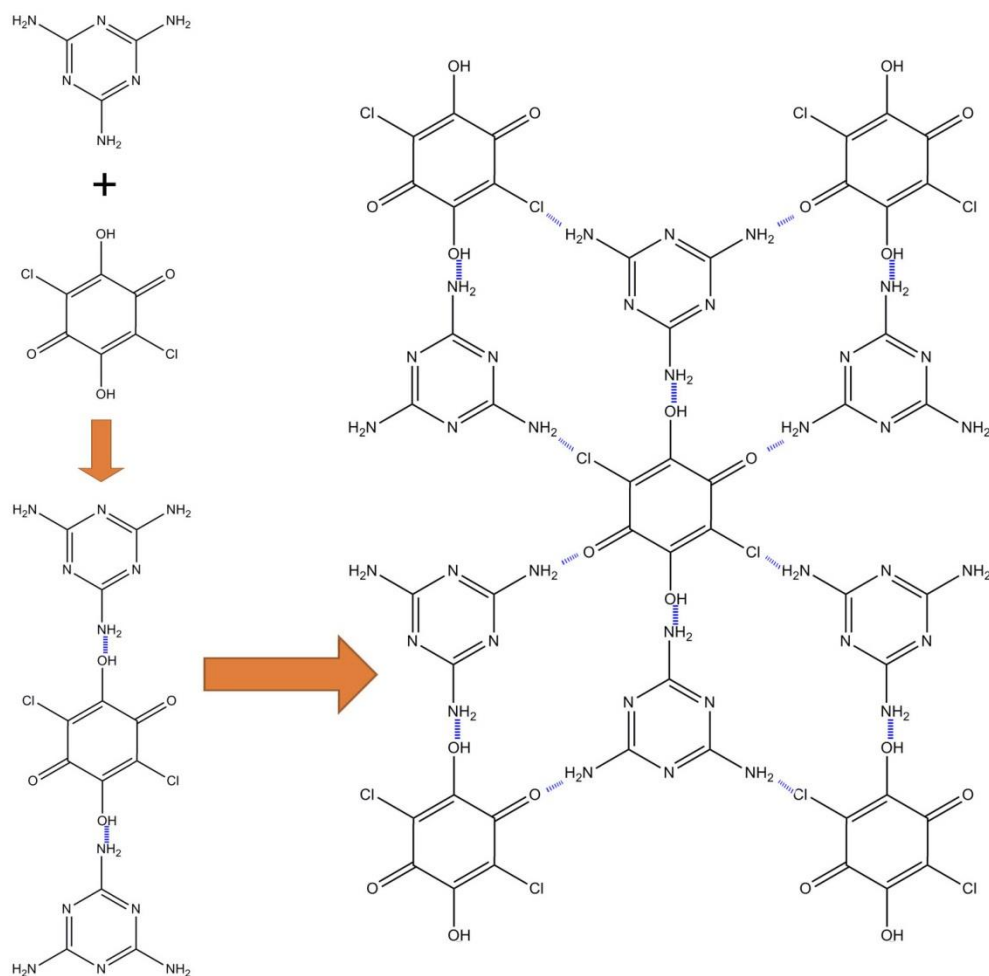


Figure 3.7 Schematic complex structure of B-M-CLA.

Based on all the information, an illustrative simplification of the supramolecular assembly of CLA and M is shown in Figure 3.7. In this structure, molarly two melamine molecules (with three secondary bonds) interact with one CLA molecule (with six secondary bonds), and they are connected *via* noncovalent forces, which is consistent with the result of the intramolecular ratio of CLA and M.

### 3.3 Characterization of B-M-CLA condensed at different temperatures

A series of condensation M-CLA products could be obtained *via* heating B-M-CLA. These new materials are named as M-CLA-X, when X is defined as the reaction temperature (°C). The details about reaction temperatures and yields are summarized in Table 3.2. Usually materials involving melamine as a precursor have low yields, because they are prone to sublime easily or degrade. However, the yields of M-CLA materials are relatively high, owing to the hindrance of the easy sublimation and degradation of melamine, thanks to the strong multiple hydrogen bond networks.

Table 3.2 Specific surface areas, Zeta potential and C/N ratio of the resulting materials

	Temperature (°C)	BET (m <sup>2</sup> g <sup>-1</sup> )	Zeta potential (mV)	C/N mass ratio	Yield
B-M-CLA	25	8.6	-1.56	0.879	0.994
M-CLA-200	25	8.6	-1.56	0.874	0.917
M-CLA-250	250	12.3	-21.6	0.874	0.886
M-CLA-300	300	19.7	27.8	0.845	0.629
M-CLA-550	550	16.8	-28.9	1.159	0.464
M-CLA-800	800	87.8	-16.8	2.680	0.131

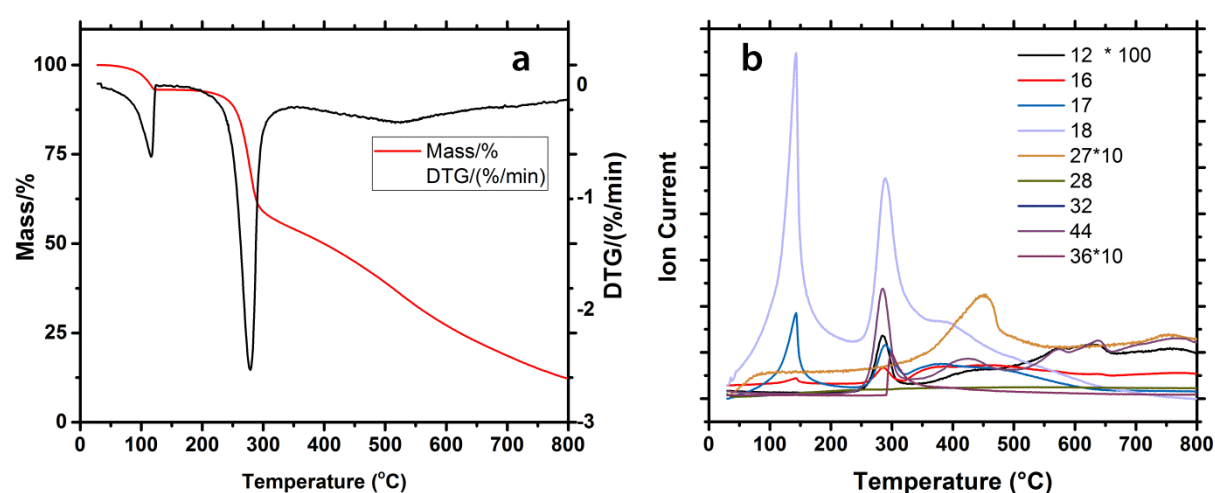


Figure 3.8 TGA (a) and TGM-MS (b) curve of B-M-CLA complex.

The gradual variation of the complex with temperature could be well followed by the analysis of thermogravimetry-mass spectrometry (Figure 3.8). Together with elemental analysis results, a general condensation process could be revealed. Before 100 °C, almost no weight loss for the supramolecular complex was observed, after which its weight slowly loses 8.2 % of general slowly before 130 °C. This weight loss within 100–130 °C could likely be referred as the loss of water bound to the structure, potentially within the crystalline system. Then, its weight reaches the second platform and remains unchanged until 200 °C. Within the range of 200–260 °C, the complex slowly lost 8.3% of its weight, which could be referred to water loss during condensation. The weight ratio of carbon and nitrogen maintain at 0.875 in the range of 25–260 °C close to the starting situation and is in full agreement with the speculation about water as the only molecule evolved. The temperature of 260 °C is very likely to be the melting point of the system. This conversion point is of significance for further discussion, because such water loss below the melting point can be formed only by condensation in lower melting structures, for instance surfaces and more disordered grain boundaries. This phenomenon is very common in polymerization of solid state, such as hexamethylene adipate salt (AH-salts) for polyimide synthesis, of which polymerization only occurs *via* molten surface layers within carefully heating protocols.<sup>[222]</sup>

Afterwards, the weight loss rate greatly accelerates with the reaction rather sharply setting in. The aggregate system was greatly reduced to 60% of the remaining mass up to 300 °C. At this temperature, the ratio of C/N decreases only slightly to 0.844, but with a great increase of the zeta potential (from negative to positive), in agreement with the further release of water through completion of polycondensation and release of CO<sub>2</sub> as a side reaction followed by MS (Figure 3.8, b). According to the MS graph and element analysis reports, a large amount of chlorine is lost during 250–300 °C, most likely in the form of HCl. The water elimination reaction as well as this secondary condensation could just bridge the ring system to extended aromatic systems, which nicely explains the massive narrowing of the band gap. At higher temperature, the weight loss keeps mildly increasing, together with the C/N ratio reaching 1.16 for M-CLA-550 and 2.72 for M-CLA-800. This process is a slow, iterative decomposition of the primary material, and the decomposition mainly occurs *via* the release of HCN and N<sub>2</sub>.

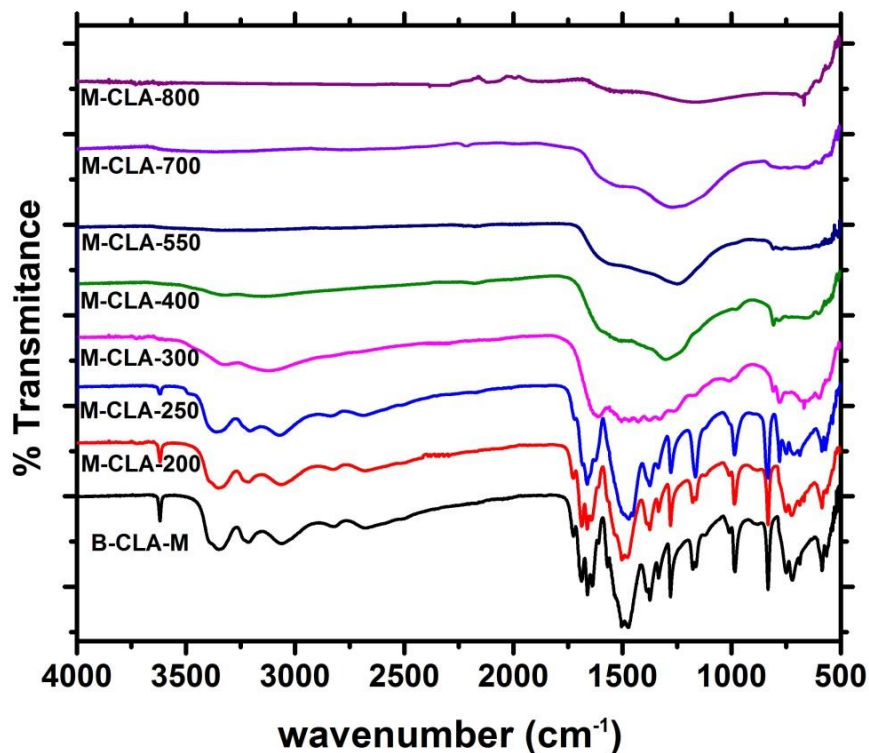


Figure 3.9 FTIR curves of materials obtained at different condensation temperatures.<sup>[220]</sup>

More details about the whole condensation process could also be told by FTIR (Figure 3.8). Compared with the complex B- M-CLA, M-CLA-200 and M-CLA-250 almost show all the infrared characteristic peaks, which proves that the main aggregate structure is unchanged at less than 250 °C. Around 12 % weight loss is attributed to drying and surface condensation. For the materials obtained at higher temperature, the variations in FTIR become more obvious, for instance the N-H out of plane deformation vibration of M-CLA-300 vanishes in the range of 650–900  $\text{cm}^{-1}$ . For M-CLA-300, the other significant difference is the great decrease of peak intensity at 3670  $\text{cm}^{-1}$  reflecting H-bonding. The disappearance of H-bonding vibration elucidates the fact that dehydration between hydroxyl and amino groups is almost completed. In general, all vibration peaks become less distinct, reflecting loss of order and the presence of a polymeric state. Above 300 °C, the aggregate turns from a polymeric structure into a carbonaceous resin, owing to vanishes of typical IR vibrations of functional groups. At this temperature, only several peaks remain, such as the vibration of triazine ring at about 800  $\text{cm}^{-1}$ , C–N at 1000–1400  $\text{cm}^{-1}$  and C=N stretching vibrations at 1500–1600  $\text{cm}^{-1}$ . The intensities of those peaks decrease step by step along with further increasing temperature. Above 550 °C, most of the characteristic peaks disappear, even including the vibration of triazine ring, which realigns into larger aromatic structures as a usual behavior for triazine materials. With all those data and information above, it can be speculated that the condensation may take place at about 250 °C, while 550 °C is the starting temperature for ring rearrangement and the formation of the final N-doped carbon.

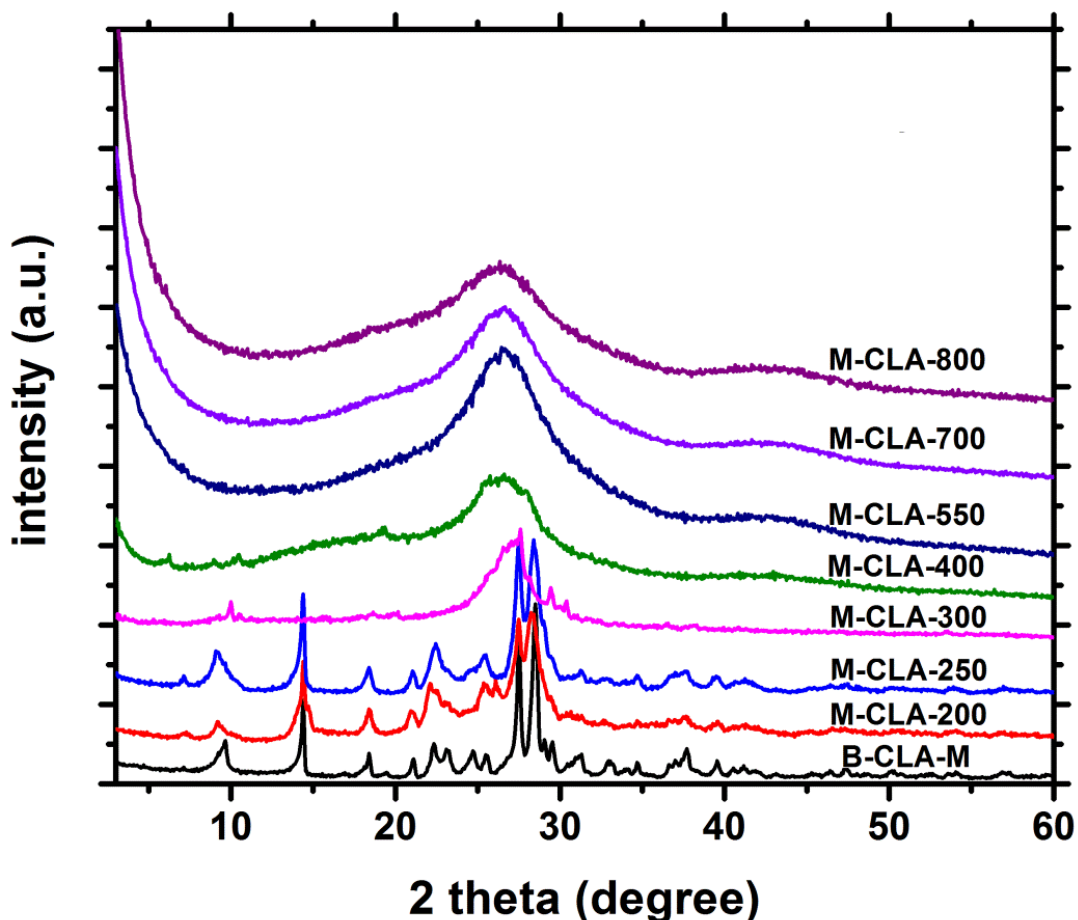


Figure 3.10 XRD of materials obtained at different condensation temperatures.<sup>[220]</sup>

The structure variation of these materials can be characterized by powder XRD, as shown in Figure 3.10. The XRD patterns of these materials are consistent with the FTIR results above. The patterns of the materials below 250 °C are very similar to the starting assembly pattern, which indicate the maintenance of the main crystal structure. There are only some minor differences, such as the strengthened peak at around 7.7°, and broadened peak at around 9.3 °C, which is probably derived from the starting dehydration within the network during this range. Above 300 °C, the patterns differ from low temperature materials obviously, revealing the melting of the whole crystal structure to form an all-polymeric skeleton. At the temperature higher than 550 °C the temperature for carbonization and ring rearrangement start, and the diffraction peaks change further until only a board peak at about 27° remains. This XRD pattern is typical and common for the interlayer stacking of weakly ordered graphitic carbons, obviously indicating the polymers' gradual condensation of polymers into N-doped carbon materials.

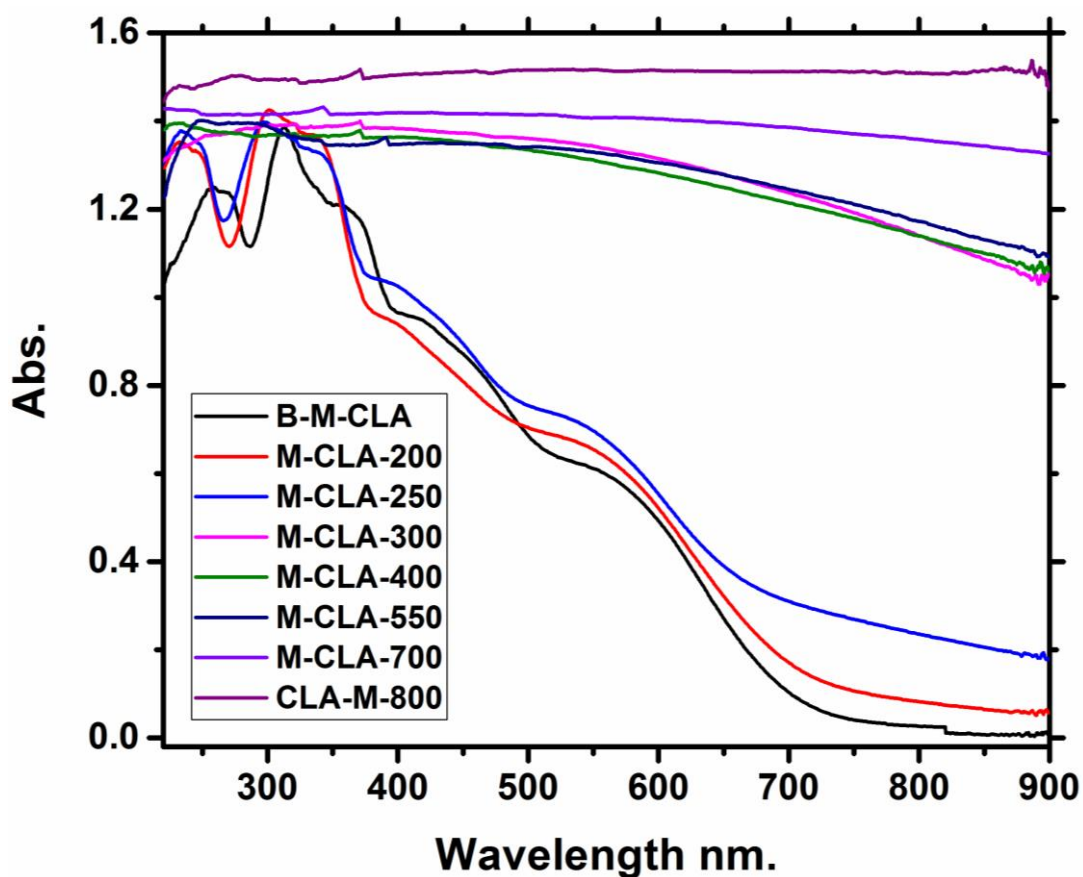


Figure 3.11 Solid UV-vis spectra of CLA-M materials obtained at different condensation temperatures.<sup>[220]</sup>

Another important characterization method is solid UV-vis absorption (Figure 3.11), which can nicely follow the electronic changes of those synthesized materials during the condensation process. There are only some slight red-shifts on the spectra occurred with condensation temperature below 250 °C, which shows weak changes in the bulk structure. For the special transition material CLA-M-250, the UV curve only has a small shift compared with the primary crystal. This variation just complies with the opinion of “a-crystal-in-a-box”, while the minor red shift and the tail towards red can be explained by a thin layer of polymer and heterojunction effects. In accordance with all the structural characterizations, the most significant variation of the light harvesting properties take place within 250-300 °C. Over 300 °C, the complex gradually turned into a black polymer resin, presumably a small bandgap semiconductor. For even higher temperatures, the product turns totally black, as typical for N-doped carbon and semi-metallic state.

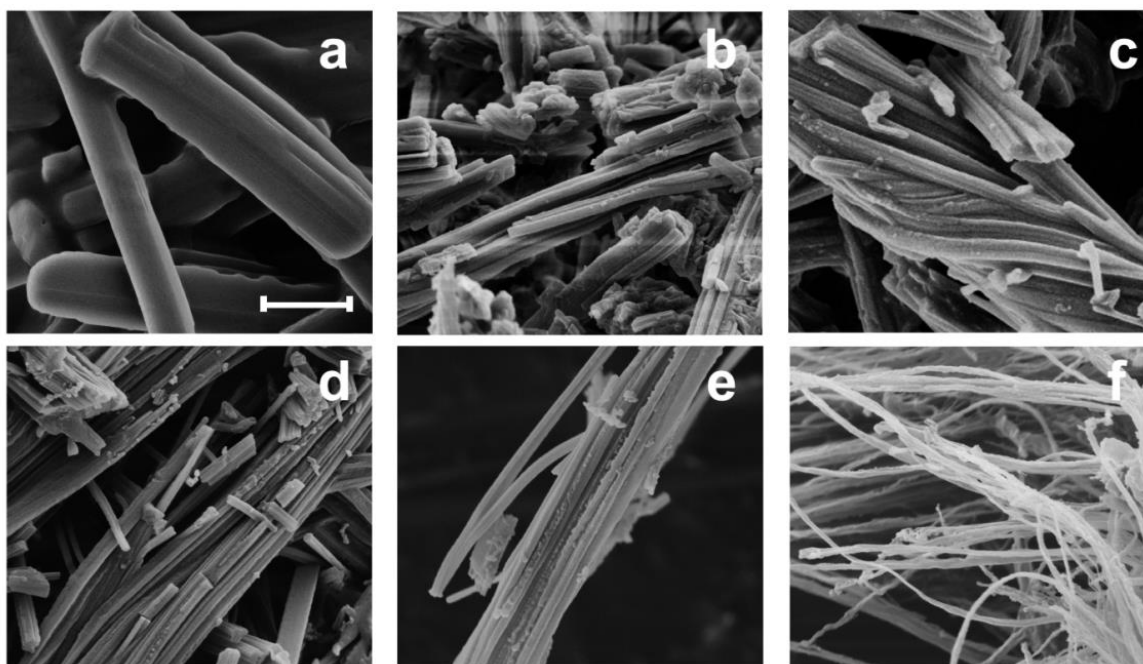


Figure 3.12 SEM images of B-M-CLA (a), M-CLA-200 (b), M-CLA-250 (c), M-CLA-300 (d), M-CLA-550 (e), and M-CLA-800 (f); (scale bar equal to 500 nm for all images)<sup>[220]</sup>

The M-CLA series was further investigated by SEM. As shown in Figure 3.12, the initial morphology of the B-M-CLA shows rod-like structure. Through whole temperature range, the structures do melt passing the melting transition, but rather gradually debundle into twisted nanowires at elevated temperatures. The SEM image of M-CLA-250 is maybe the most prominent proof that the sample indeed undergoes surface and grain boundary polycondensation at 250 °C: the melting does not lead to droplets, but rather fills these boxes under preservation of the highly anisometric structures. With the even increasing of temperature, these fibers gradually turn into hollow nanotubes, corresponding to the highest mass loss and degree of densification of these structures. These assumptions could be also proved by TEM. With the increase of temperature, the complex gradually changes from solid bulk into hollow fibers at 800°C *via* twisted-wire like structure. (Figure 3.13)



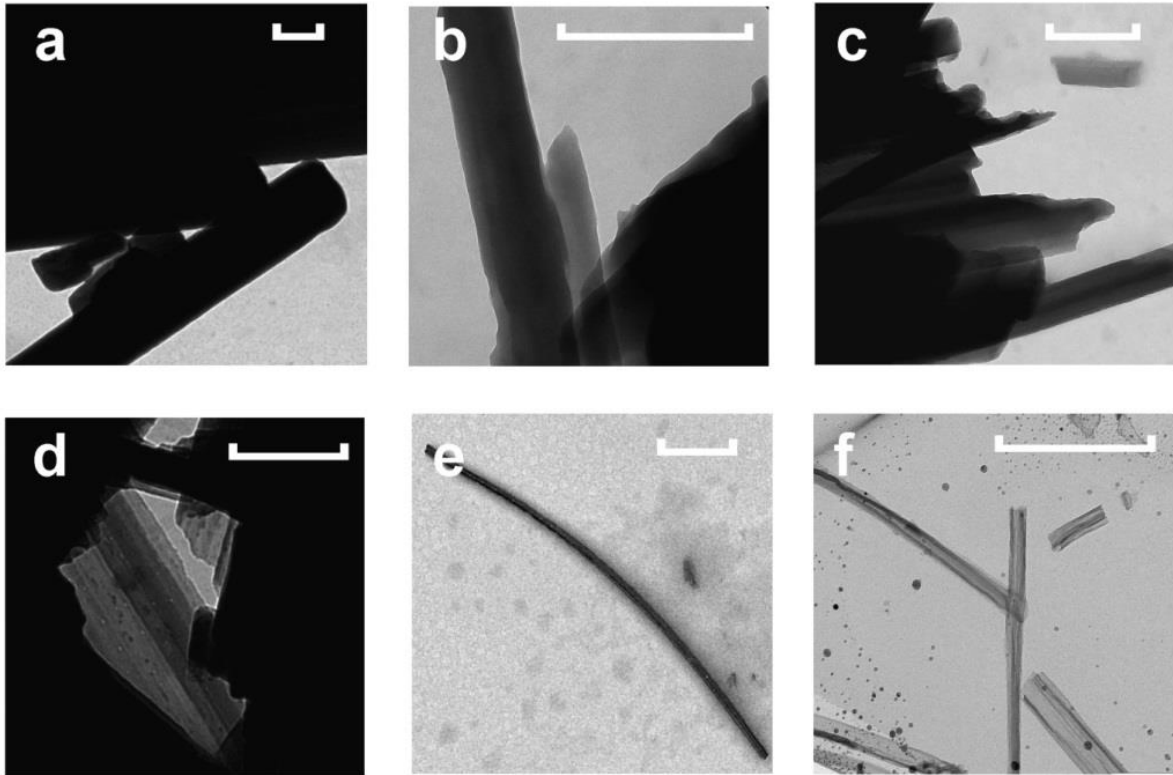


Figure 3.13 TEM images of B-M-CLA (a), M-CLA-200 (b), M-CLA-250 (c), M-CLA-300 (d), M-CLA-550 (e), and M-CLA-800 (f); all the white scale bars are equal 1  $\mu\text{m}$ .<sup>[220]</sup>

In order to provide more details about the transition material CLA-M-250, another high resolution TEM photograph was also taken to exhibit the exact structure of high temperature M-CLA materials as shown in Figure 3.14. It can be clearly observed that the tube-like solid material is enwrapped in a half transparent cover of around 5 nm thickness. This cover can be attributed to the polymer cover layer we described before.

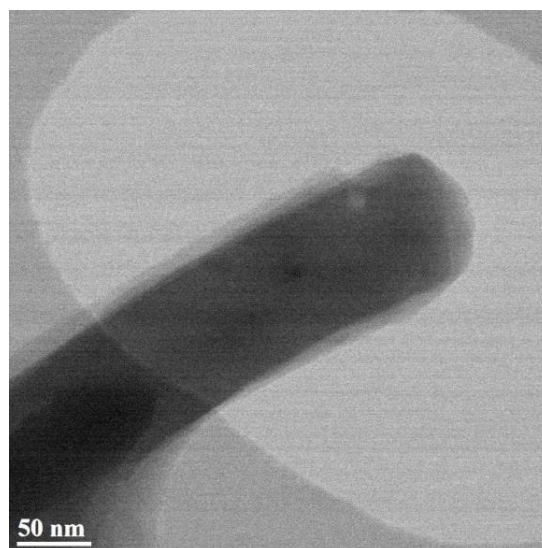


Figure 3.14 High resolution TEM images of CLA-M-250.



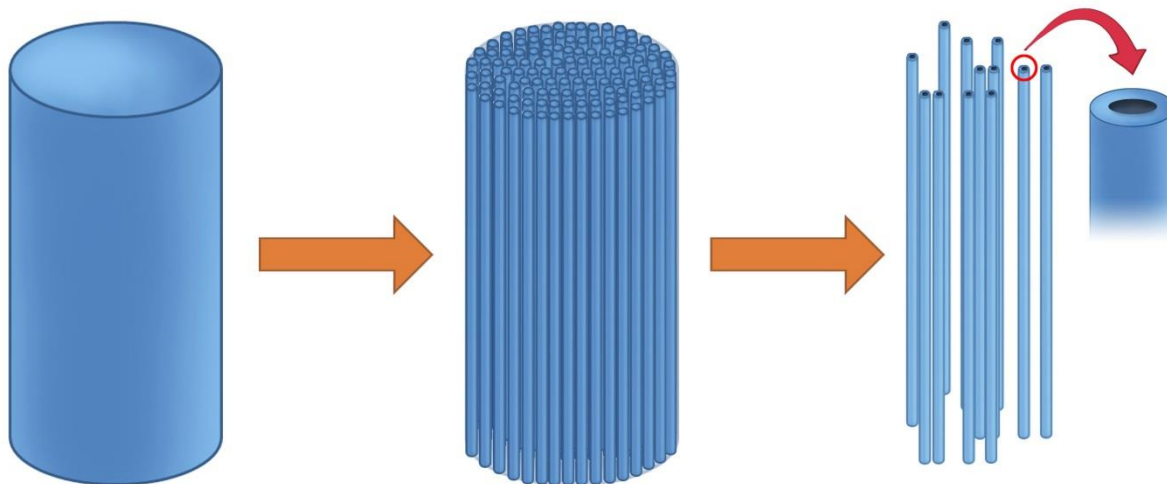


Figure 3.15 Simplified scheme of the variation of the morphology with temperature.<sup>[220]</sup>

Based on the image information from both SEM and TEM, a simplified structural variation procedure is proposed in Figure 3.15. The rod-shape complex first surface/grain boundary melted and polymerized into tight stacked fibers. Then with the further increase of temperature, those fibers become hollow while they are separated from each other. Compared with the supramolecular complex of DBQ and M described in the last chapter, the morphologies of resulting materials in this protocol show fiber-like instead of sheet-like structure. This significant morphology variation must result from the only difference between the two systems, which is the introduction of two chloride atoms in CLA monomer. As an electron withdrawing group, the presence of Cl greatly decrease the electron density of the six-atom ring, which leads to more simple ionization of hydroxyl groups. This is also seen by the fact that CLA monomer is with acidity while DBQ monomer is not. Thus, the interactions are getting stronger between hydroxyl groups of CLA and amino groups. Under this condition, the growth of the primary supramolecular is more likely to take place in the OH/NH<sub>2</sub> direction, and gets restricted to the lateral noncovalent bond direction. The higher crystallization yield of B-CLA-M is a further sign for the stronger connection than in B-M-CLA.

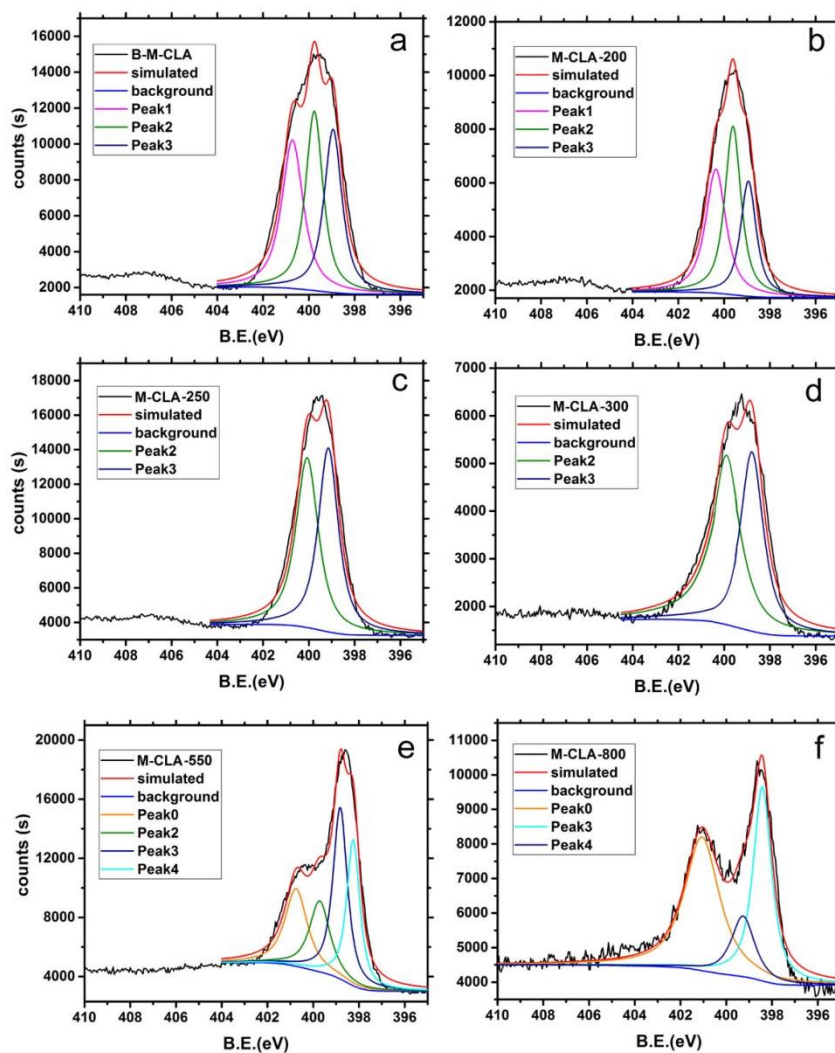


Figure 3.16 N1s XPS curves of B-M-CLA (a), M-CLA-200 (b), M-CLA-250 (c), M-CLA-300 (d), M-CLA-550 (e) and M-CLA-800 (f).<sup>[220]</sup>

XPS measurement was employed to elucidate the local structural changes on the bond level during the heating process as shown in Figure 3.16. The structure variation could be clearly followed with the N 1s XPS curves presenting different connection modes with other atoms. The original N 1s peaks for the complex can be divided into 3 groups, which represent hydrogenated nitrogen at 400.8 eV, charge depleted amine at around 399.8 eV and nitrogen in the triazine ring at around 398.8 eV. For the complex as well as M-CLA-200, the peak at 400.8 eV reflects the presence of NH<sub>2</sub>, which interacts with OH from CLA. This peak disappears at higher temperatures (e.g. 250 and 300 °C), indicating the possible pathway of dehydration within the supramolecular crystal. A new peak of aromatization region at 401 eV would appear with further elevation of temperature for M-CLA-550 and M-CLA-800, revealing the formation of quaternary nitrogen. Together with that, another new peak emerges at 398.3 eV, indicating nitrogen in C-N, which reflects the disintegration of triazine rings and aromatic rearrangements.

### 3.4 Photoactivity of CLA-M materials

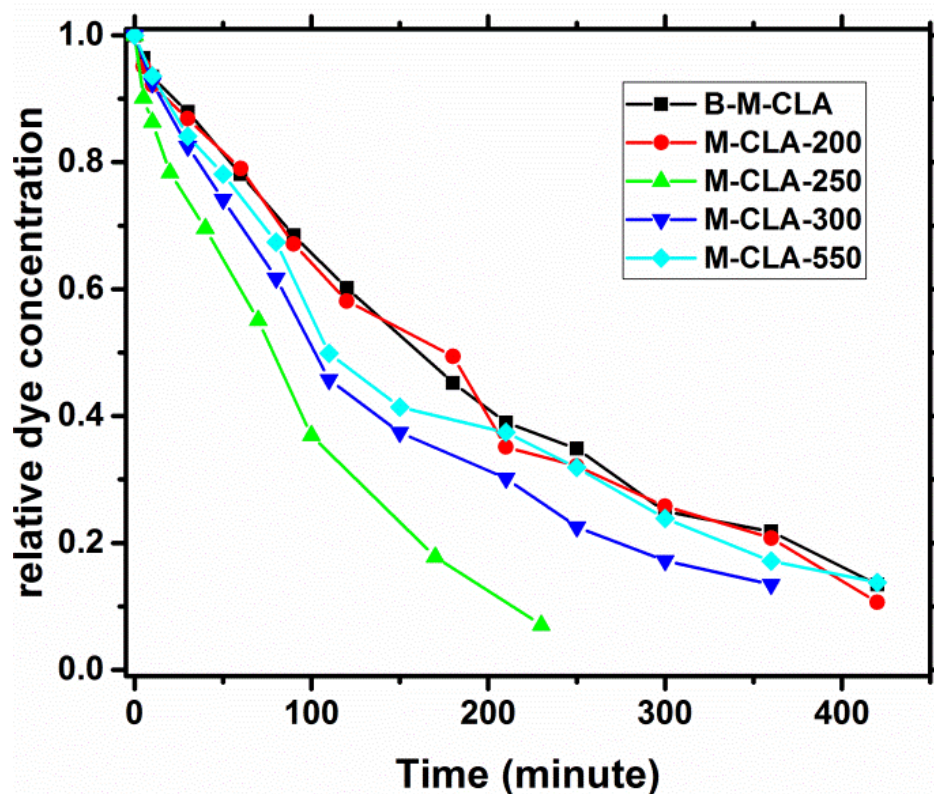


Figure 3.17. Photochemical RhB degradation curves with different photocatalysts.

Dye degradation is the most intuitive method to show the photoactivity of catalysts. Therefore, all the resulting materials were tested in the degradation of Methylene Blue (MB) and Rhodamine B (RhB) under white light illumination (420 nm- IR Infrared). Different from DBQ-M materials, CLA-M materials can not only degrade MB but also RhB, which is more difficult. Thus, here all the following degradation experiments were conducted with RhB as the model organic material. For the degradation experiments, about 5 mg of M-CLA materials were added into 30 mL glass bottle with 20 mL RhB solution ( $1 \text{ mg L}^{-1}$ ). After 2 hours' stirring in dark environment, the reaction bottle was placed under illumination by 50 W LED light with constant stirring. For a typical time length, part solution was taken to be centrifuged first and then measure the remaining dye concentration by UV-vis spectra at the wavelength of 554 nm (RhB). Although showing different degradation rates, almost all those materials successfully decomposed the dye molecules. As the degradation of RhB could reveal more information about the photo reaction mechanism, the degradation results were analyzed in detail. Most relevant and unexpected, among all the samples, M-CLA-250 showed the best degradation performance. 5 mg M-CLA-250 could degrade 90% of 20 mL 1 mg/L RhB in 4 hours, in spite of the fact that the bulk of the material and the corresponding light absorbance is still of the same as in the primary material. As shown in the graph, the supramolecular B-CLA-M crystal is already visible light active as an H-bridge stabilized, organic semiconductor. RhB degradation by B-CLA-M takes about

twice the time of M-CLA-250, which probably results from its structural properties. As mentioned in Figure 3.3, M-CLA-250 possesses a tiny layer of polymer on the top with its different electronic structure. This polymer layer here can act as a heterojunction and improves effectivity of charge separation and subsequent charge transfer. This “boxed” organic semiconductor obviously outperforms all other species, as it combines crystalline order and coupled excellent charge transport with the stability of a polymer for stabilization and charge transfer.

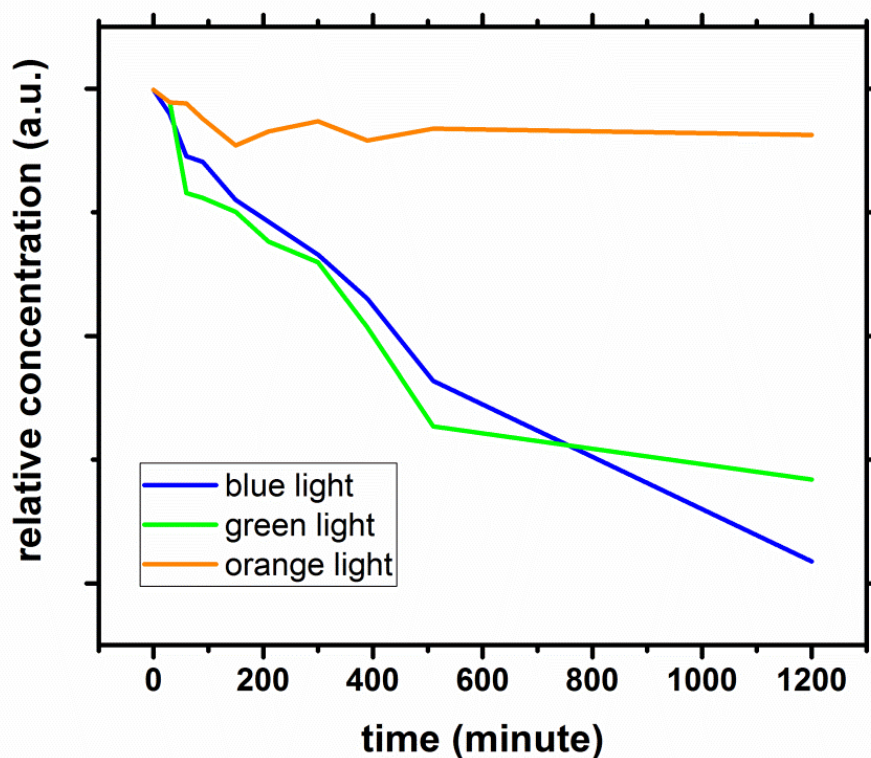


Figure 3.18 Photochemical RhB degradation curves with different narrow light illumination (445 nm blue light, 520 nm green light and 590 nm orange light).

With the best degradation performance, M-CLA-250 was thus used to further explore photoactivity. In order to confirm its activity in pure visible light, the RhB degradation experiments were conducted under narrow visible light. In this experiment, the 50 W white light was replaced by 50 W blue light (445 nm), green light (520 nm) and orange light (590 nm), respectively. Similar to the experiment above, the dye concentration was measured after certain time of illumination. As shown in Figure 3.18, under the illumination of green light and blue light, M-CLA-250 can successfully degrade RhB and their degradation rates are close. However, under orange light (590 nm), it seems impossible for M-CLA-250 to degrade organic dyes, which is in the agreement with its UV-vis spectrum in Figure 3.11.

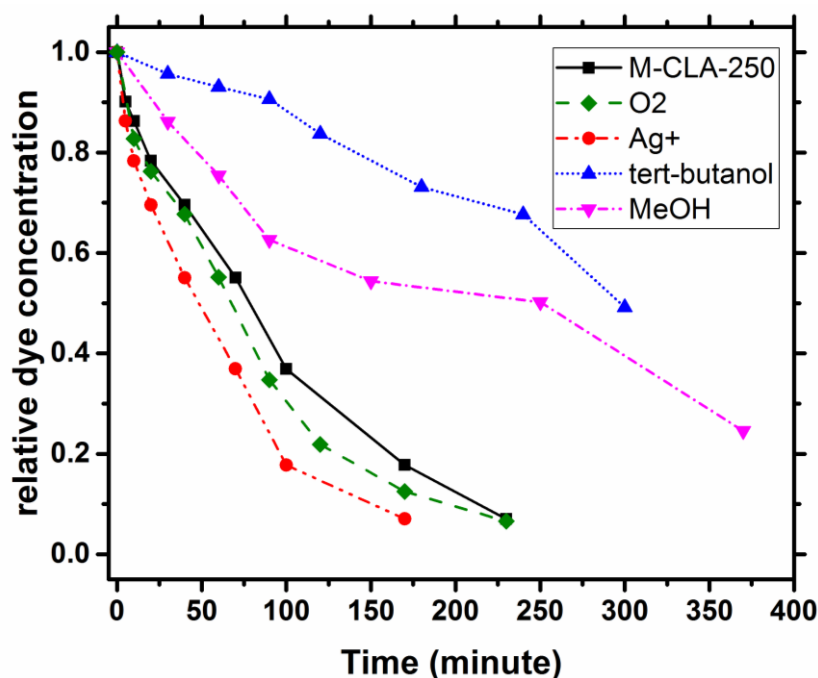


Figure 3.19 Photochemical RhB degradation curves with different additives.<sup>[220]</sup>

The affirmation of the photodegradation path *via* photogenerated holes or by electron transfer is important for mechanism of RhB degradation. Thus, electron acceptors and hole scavengers, like tert-butanol and methanol, were introduced in the degradation system (Figure 3.19). As a result, electron acceptors, such as Ag<sup>+</sup> and oxygen, can help accelerate the degradation process, while the introduction of hole scavengers strongly hindered the dye photodegradation. Based on these results, it can be confirmed that RhB degradation is mainly through the photogenerated holes.

At the end of a typical RhB degradation experiment, a peroxide stripe test was dipped into the already colorless solution for one second. Then the test was compared with standard color card and unveiled the existence of OH radicals in a concentration of  $\sim 3 \mu\text{g/L}$ . Their existence indicate the photogenerated holes can obviously oxidize water, resulting first in the formation of OH radical that can further recombine to peroxide, which both oxidize RhB molecules into colorless fragments. Moreover, the fact that even peroxide was formed indicated that the valence band (VB) of CLA-250 is significantly more positive than 1.763 eV *vs.* NHE - the minimum energy that is required to form peroxide.

In order to further examine the oxidation power of the photocatalysts, CLA-M-250 was also used to degrade the colorless organic compounds phenol. 20 mg CLA-250 were added into 30 mL glass bottle with 20 mL 1mg/L phenol water solution. After stirring in dark for 1 h, the whole system was placed under 50W white light illumination for one day. With the process of photo reaction, the solution was measured with gas chromatography-mass spectrometry (GC-FID), the peak area of phenol could be observed slowly to decrease with time as shown below. Before and after the degradation, both of the

solutions were checked with GC-MS. Before that, the signal of phenol could be detected, however after that this signal disappears. In addition, the pH of this system drop to 4 from 5.5 at the beginning, which could represent the final degradation products, could be acidic substances, such as oxalic acid or succinic acid. This information could be used to prove the fragmentation of phenol.

Table 3.3 Peak area of phenol in solution with the process of photoreaction

Time (h)	Integral Peak area (unit: million)
0	6.62
4	6.44
12	5.97
16	5.77
24	5.34
36	4.06

With more positive than 1.763 eV vs. NHE valence bond, CLA-M-250 should be able to fully oxidize water into molecular oxygen, because it is energetically easier than the formation of peroxide. However, whether it can successfully realize oxygen production still requires to be proved, because it usually gets kinetically hindered as it requires the simultaneous transfer of four electrons and four protons. Indeed, we found out that M-CLA-250 without cocatalyst can generate very low amounts of oxygen. Using cobalt oxide as a cocatalyst one can accelerate the four electron process.

The cocatalyst doped M-CLA-250 was synthesized by using 400 mg M-CLA-250 and 48 mg  $\text{Co}(\text{NO}_3)_2$  that were mixed together with 50 mL water. Then the solution was constantly stirred while heated at around 80 °C for 2 h. After that,  $\text{Co}(\text{NO}_3)_2$  was converted to CoO at 200 °C. For the oxygen evolution reaction measurement, 100 mg Co doped M-CLA-250 material was added into the reaction flask together with 200 mg  $\text{AgNO}_3$  and 100 mL water. Then the whole reaction system was flushed with nitrogen for 5 minutes to remove dissolved oxygen. During the experiment process, an oxygen sensor was inserted under the water level while nitrogen was continuously coming above the liquid level to prevent oxygen leakage from the outside. The experiment setup was exposed to visible light at around 20 °C, while the oxygen content was monitored by oxygen dipping probe sensor from PreSens. The control experiments were conducted also as above mentioned, only without one factor each time, such as illumination,  $\text{AgNO}_3$  or cocatalyst. (Figure 3.20)



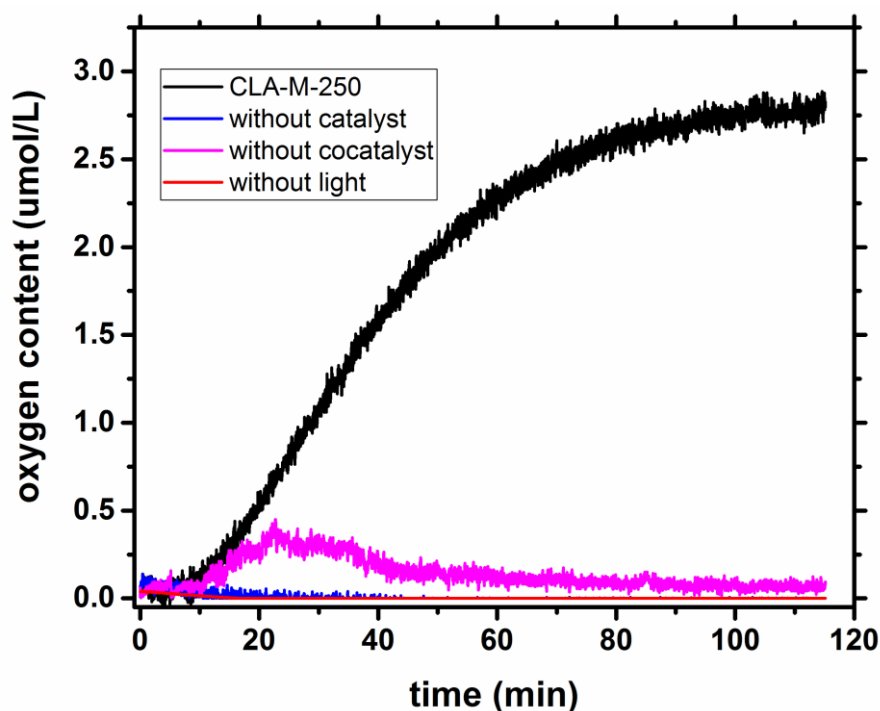


Figure 3.20 Oxygen production under illumination with M-CLA-250 as catalyst.<sup>[220]</sup>

In a typical oxygen production experiment, the concentration of oxygen in water increases with illumination time and reached a maximum amount of 2.8  $\mu\text{mol/L}$  after 110 min. In the first 50 min, the oxygen generation showed the highest rate at around 0.05  $\mu\text{mol L}^{-1} \text{min}^{-1}$ . After that, the oxygen production process slows down, probably due to the deposition of Ag on the photocatalyst surface that inhibits the water oxidation process.

### 3.5 Conclusion

In this chapter, a series of new materials are synthesized through supramolecular preorganization of DBQ and M at different condensation temperatures, after careful selection of starting monomers. In this work, highly ordered fiber-like structures were prepared, using chlorine substitution to restrict lateral growth. The optical and catalytic properties as well as the carbon and nitrogen ratio of the materials can be tuned by calcination temperature while the fiber-like morphology is preserved up to 800 °C. Among all the obtained materials, CLA-M-250 underwent polycondensation only on grain boundaries and its surfaces, which generates a “boxed” crystalline organic semiconductor. This material shows the highest photocatalytic activity of the whole series in degradation of dyes, driven by a very high VB stability and the corresponding strong oxidation power. This ability is so strong that OH-radicals and finally oxygen can be produced from water under illumination with white light, a process that previously only the more stable g-CN materials can accomplish. We believe that this work can open many opportunities for rational nanorod semiconductor design as well as for new materials for photooxidation reactions for both organic synthesis and environmental remediation.

## 4 Photocatalytic cyanation of graphitic carbon nitride scaffold: tuning band structure and enhancing the performance in green light driven C-S bond formation

### 4.1 Background and state-of-the-art

#### 4.1.1 Post modification of photocatalyst

In last two chapters, two series of photoactive materials (DBQ-M materials and CLA-M materials) are prepared with different supramolecular pre-compositions. It will be shown that this is a feasible way to improve the performance of photocatalyst simply by adjusting its starting monomers. This method usually changes both the structural and functional properties thoroughly. For some photocatalysts with excellent photocatalysis performance, they only require to be strengthened on their own basis to promote its current photocatalysis efficiency, for instance g-C<sub>3</sub>N<sub>4</sub>. As elaborated in Chapter 1.6, low solar utilization efficiency is still one of the most significant challenges for photocatalyst. Therefore, it becomes important and meaningful to seek for post-modification methods to further improve the performance of photocatalysts.

Among various post modification methods, an effective way to modify carbon nitride is the introduction of defects.<sup>[223]</sup> In fact, the defects can alter the electronic structure, which leads to additional visible light absorption. Moreover, they can also serve as active sites for photocatalytic reactions and provide trapping sites to retard the recombination of charge carriers.<sup>[85, 224]</sup> Recently, nitrogen deficient carbon nitride materials by introducing nitrogen defects in the framework were found to significantly expand the visible light response of such materials.<sup>[225-227]</sup> This process remarkably enhances the photocatalytic activity but harsh reaction conditions are required for modification, such as high temperature reduction in hydrogen flux, calcination in the molten KOH, and hydrothermal conditions etc. An alternative pathway with milder reaction conditions and more facile operations was to our opinion still desirable.

#### 4.1.2 Modification *via* functional groups

Given the conjugated system of the g-C<sub>3</sub>N<sub>4</sub> and learning from the long history of dye chemistry, color can be tuned by expanding the conjugated systems with small donor and acceptor substituents.<sup>[228, 229]</sup> We thus propose a strategy of grafting e.g. cyano groups on g-C<sub>3</sub>N<sub>4</sub> scaffold, thus lowering the relative nitrogen content chemically, as opposed to the previous approaches of reducing the nitrogen contents by partially destroying the g-C<sub>3</sub>N<sub>4</sub> frameworks (and potentially creating the nitriles indirectly as leftover groups). The challenge here is, in spite of the known chemical/thermal stability of the tri-*s*-triazine unit and the carbon nitride, to develop efficient approaches for grafting the selected functional groups.



It has been reported that cyano groups can be photocatalytically grafted onto N-containing heterocyclic rings.<sup>[230]</sup> Moreover, thiocyanate salts, which could be converted to cyanates by oxidation, are widely used as a safe cyanation reaction reagent.<sup>[231-233]</sup> Inspired by those facts, we employed thiocyanate salt as the cyano group source *via* a facile photocatalytic reaction. To our delight, cyano groups were successfully grafted on g-C<sub>3</sub>N<sub>4</sub> by a facile photocatalysis reaction.

#### 4.1.3 Brief introduction to this chapter

This chapter demonstrates a novel strategy for g-C<sub>3</sub>N<sub>4</sub> post-modification. In this strategy, thiocyanate ions are first photocatalytically converted to cyano radicals by carbon nitride; which recombine with the carbon nitride scaffold afterwards, forming cyanated g-C<sub>3</sub>N<sub>4</sub> (g-C<sub>3</sub>N<sub>4</sub>-xCN. Here, where x represents the content of CN group in the sample by weight percentage). It is worth noting that the C/N ratios (or the CN group content in the sample) and the substitution degree can be facilely controlled by varying the reaction conditions, such as irradiation time and NaSCN concentration of the reaction mixture. Most importantly, the band gap is directly affected by the cyano group content in g-C<sub>3</sub>N<sub>4</sub>-xCN. The samples with a higher CN content show a narrower band gap. The band gap could be tuned down to 2.29 eV, as compared to 2.73 eV for the pristine g-C<sub>3</sub>N<sub>4</sub>, expanding the visible light response to an adsorption edge of 590 nm. It is shown that the photo-induced charge-carriers separation is improved as well, and that g-C<sub>3</sub>N<sub>4</sub>-xCN exhibits significantly enhanced performance under green light (520 nm) irradiation, as exemplified with a model reaction, the photocatalytic C-S coupling reaction towards alkenyl sulfones. This can be set in stark contrast with the negligible activity of the pristine carbon nitride at this wavelength.

#### 4.2 Preparation methods of cyanation of graphitic carbon nitride scaffold

All the chemicals in this chapter were purchased from Sigma Aldrich. Unless specified, all the chemicals have not been subjected to further processing.

*The preparation of g-C<sub>3</sub>N<sub>4</sub>:* 0.01 mol (1.26 g) melamine and 0.01 mol (1.29 g) cyanuric acid were added into a 250 mL beaker with 100 mL H<sub>2</sub>O inside. The mixed suspension was stirred overnight while the stirring speed is 500 rpm. Then, the solid matter was separated by centrifuge at 8000 rpm for 5 minutes, and dried in vacuum oven at 60°C for 10 hour. Fully dried materials is CM (cyanuric acid and melamine) complex, which was polymerized at 550 °C for 4 hours in an oven under N<sub>2</sub> flow. The as synthesized light yellow powder is the g-C<sub>3</sub>N<sub>4</sub>.

*Cyanation of carbon nitride:* the cyanated carbon nitride samples with varying CN modification are denoted as g-C<sub>3</sub>N<sub>4</sub>-xCN, where x represents the content of CN group in the sample by weight percent. In a typical synthesis of g-C<sub>3</sub>N<sub>4</sub>-16CN, 60 mg g-C<sub>3</sub>N<sub>4</sub> and 180 mg NaSCN are added to 20 mL acetonitrile in a 50mL photoreactor. The photoreactor was irradiated by 100W

white LED for 8 hours in air under room temperature. The solid product was collected and washed with H<sub>2</sub>O and ethanol. For the samples with various CN contents, only the concentration of NaSCN was changed, while all other parameters are kept the same.

#### 4.3 Characterization of g-C<sub>3</sub>N<sub>4</sub>-xCN materials.

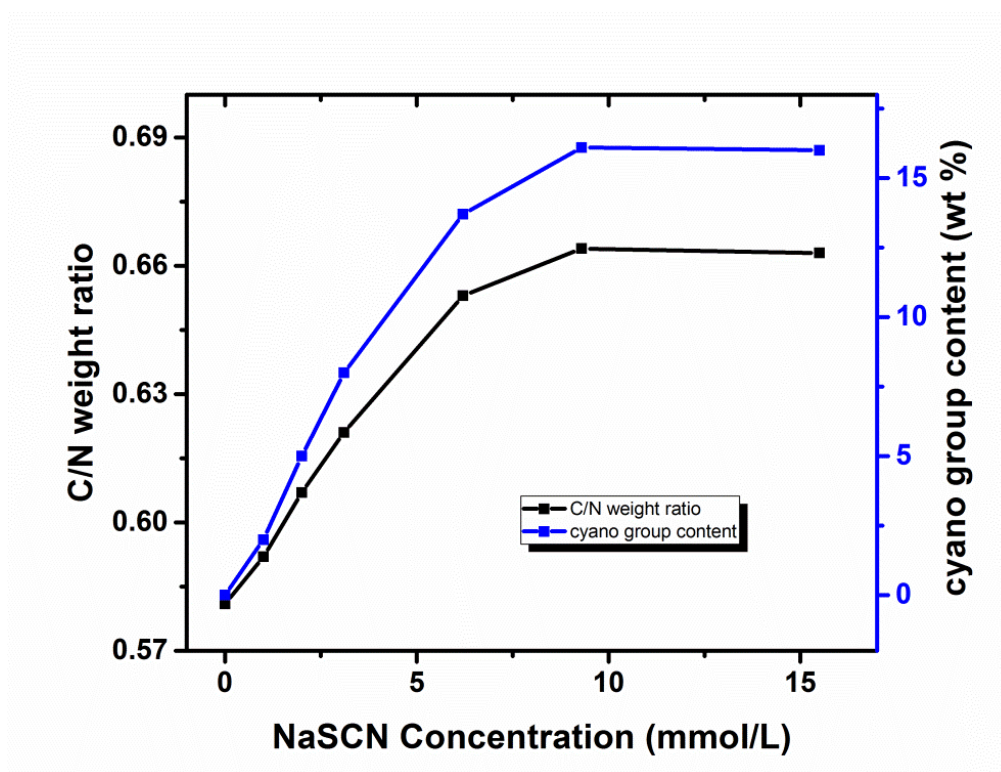


Figure 4.1 The C/N weight ratio and cyano group weight content of g-C<sub>3</sub>N<sub>4</sub>-xCN materials.

In order to measure the amount of grafted cyano group, inductively coupled plasma mass spectrometry (ICP-MS) was used to analyse the element composition of these g-C<sub>3</sub>N<sub>4</sub>-xCN materials. As no S content was detected, we are sure that the grafted group should be cyano group. With the photocatalytic cyanation reaction, the content of grafted CN groups can be transcribed from elemental analysis. In Figure 4.1, the weight ratio of C/N increases with the input of NaSCN; and the cyano group weight percentage reaches a maximum value of 16% (C/N molar ratio of 0.664). Further increase of NaSCN concentration with elongated irradiation time could not raise C/N ratio any more, indicating that all the possible reaction sites on g-C<sub>3</sub>N<sub>4</sub>-16CN scaffold have been substituted by cyano group. This reaction can thereby be easily used to evaluate the incompleteness of the condensation of the tri-s-triazine units, and the as-made polymeric carbon nitride is obviously rather a melon than a completely condensed g-C<sub>3</sub>N<sub>4</sub>.

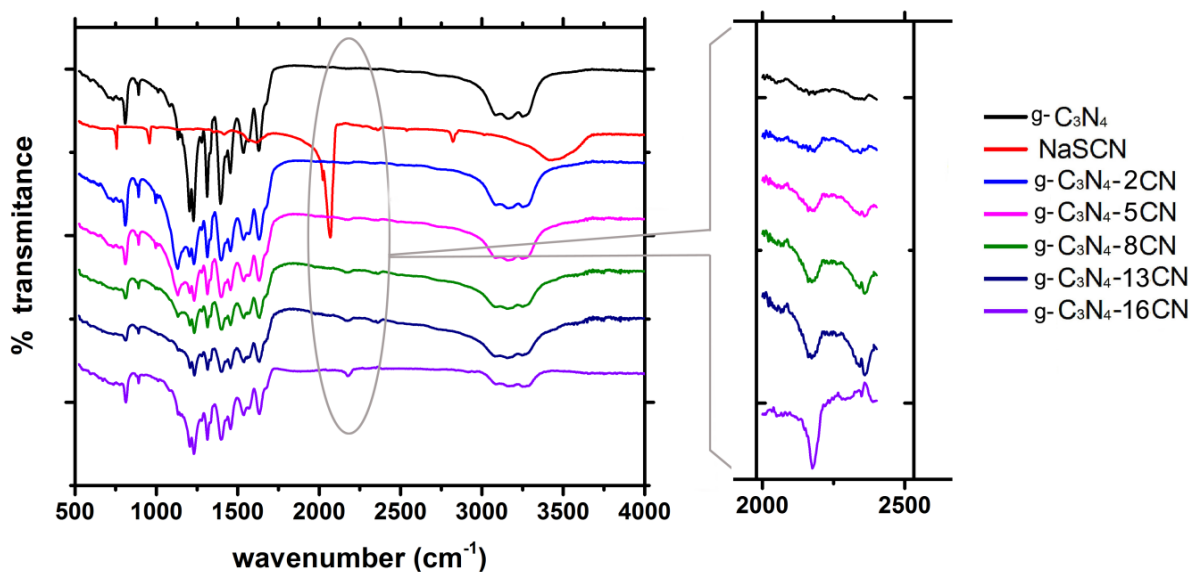


Figure 4.2 FTIR spectra of  $g\text{-C}_3\text{N}_4\text{-xCN}$  samples.

The samples were characterized by Fourier transform infrared (FTIR) spectra to understand the changes in fundamental structure of the  $g\text{-C}_3\text{N}_4$  scaffold caused by cyanation (Figure 4.2). As for the starting chemical, NaSCN shows a sharp absorption peak at  $2100\text{ cm}^{-1}$ , while for all the  $g\text{-C}_3\text{N}_4\text{-xCN}$  samples, this peak is absent, which states that all the  $g\text{-C}_3\text{N}_4\text{-xSCN}$  samples are free of NaSCN residues. It is worth noting that there are two distinctive peaks varying in intensity with cyano group contents in the samples. One is the absorption peak at  $2230\text{ cm}^{-1}$ , which is corresponding to the carbon-nitrogen triple bond ( $\text{C}\equiv\text{N}$ ) vibration and consequently increases with cyano content in the samples. The other is the multiple broad peaks at  $3000\text{--}3300\text{ cm}^{-1}$ , which are assigned to the N-H stretching vibration of the amine group ( $-\text{NH}_2$ ). With the increase of cyano group content in the samples, this N-H vibration peak is massively diminished. These data strongly support the proposed substitution of amino group ( $-\text{NH}_2$ ) by the cyano group ( $-\text{CN}$ ). All the other typical vibration peaks of the  $g\text{-C}_3\text{N}_4$  scaffold keep unchanged, indicating that the carbon nitride framework stays intact.

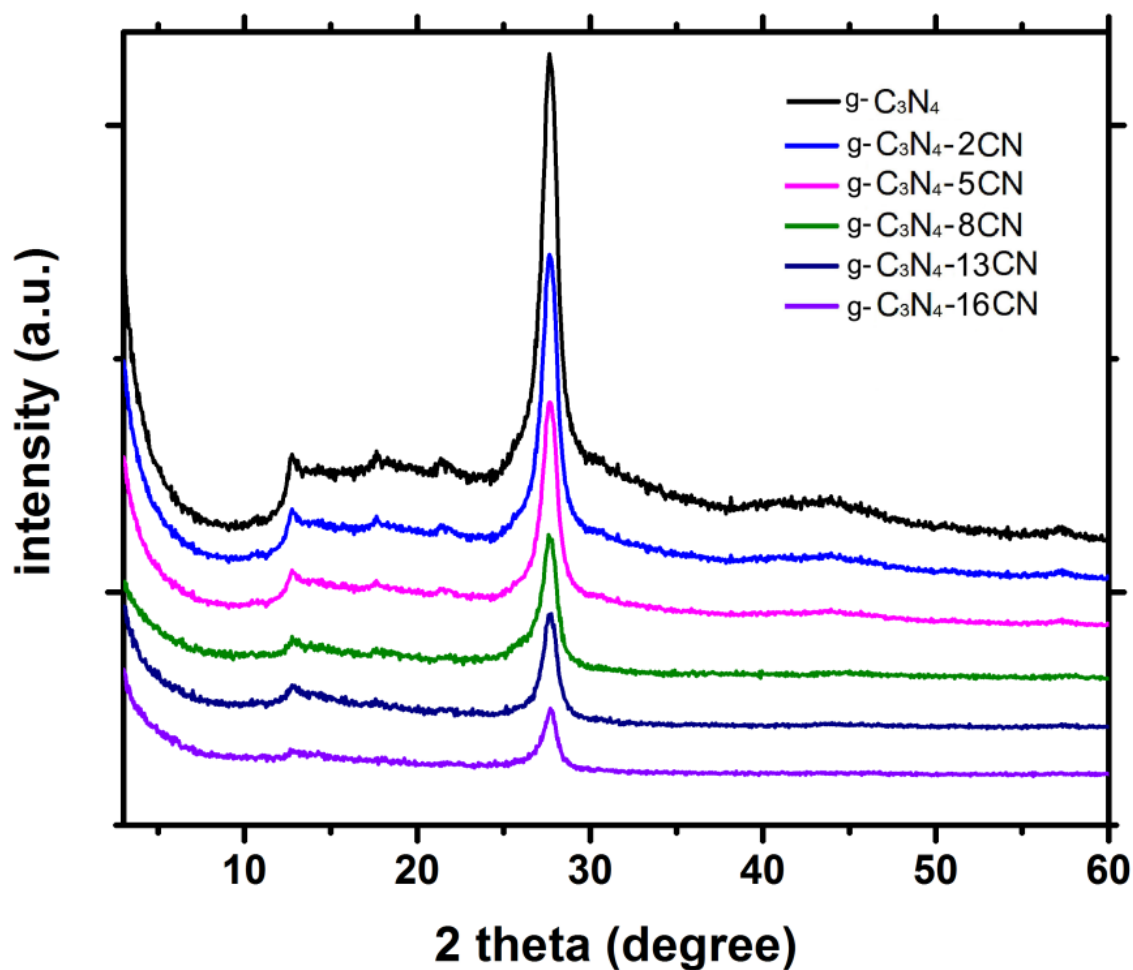


Figure 4.3 X-ray diffraction patterns of g-C<sub>3</sub>N<sub>4</sub>-xCN samples.

To study the effect of the cyanation on the crystallinity of the materials, these samples were further characterized by X-ray diffraction (XRD, Figure 4.3). The diffraction intensity from the sample with higher cyano group content is lowered, but in spite of the changes in peak intensity, all the samples show the characteristic diffraction from (002) crystal plane at 27.5°, without any displacement. This states that reaction potentially delaminates the sample, but that otherwise the in-plane packing and inter-plane stacking situation of C<sub>3</sub>N<sub>4</sub>-xCN did not change at all; even the distance between layers is kept the same. This further proves our assumption that that cyano group (-CN) replace amino group (-NH<sub>2</sub>), and that g-C<sub>3</sub>N<sub>4</sub> scaffold is preserved after photocatalytic cyanation reaction.

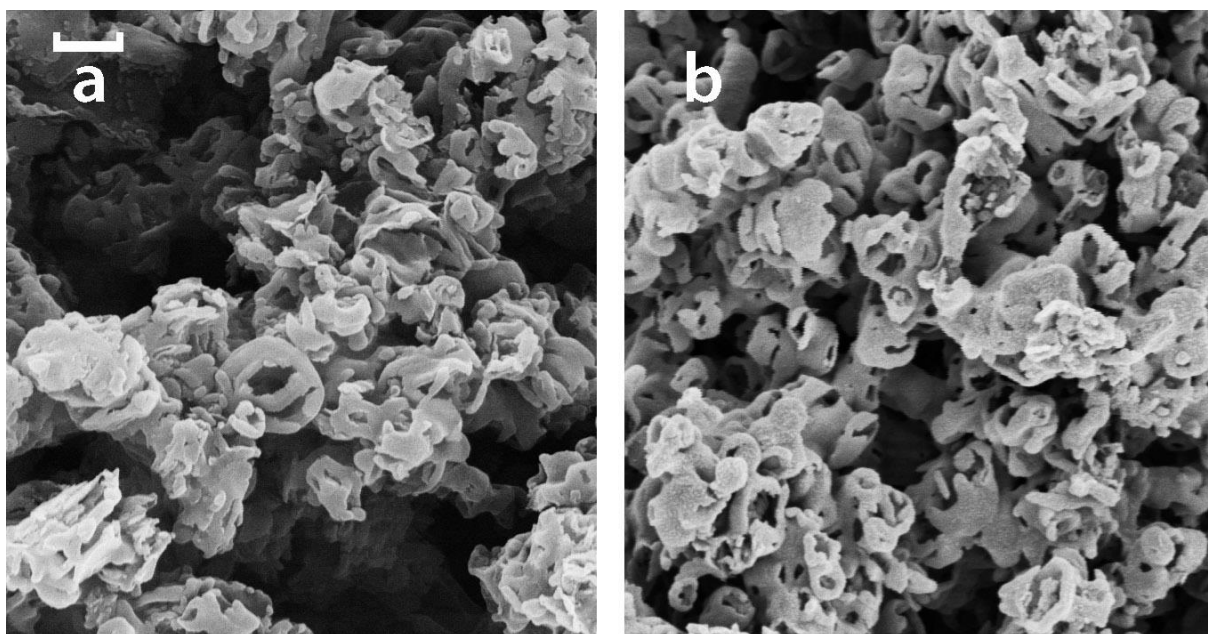


Figure 4.4 SEM graphs of g-C<sub>3</sub>N<sub>4</sub> (a) and g-C<sub>3</sub>N<sub>4</sub>-16CN. (Scale bar equal to 1 μm)

Scanning Electron Microscopy was used to help better understand the morphology variation after cyanation reaction. As shown in Figure 4.4, there is no obvious difference on morphology of g-C<sub>3</sub>N<sub>4</sub> and cyanated carbon nitride. This shows the cyanation reaction just takes place on the peripheral sites of g-C<sub>3</sub>N<sub>4</sub> and does not influence the general main morphology at all.

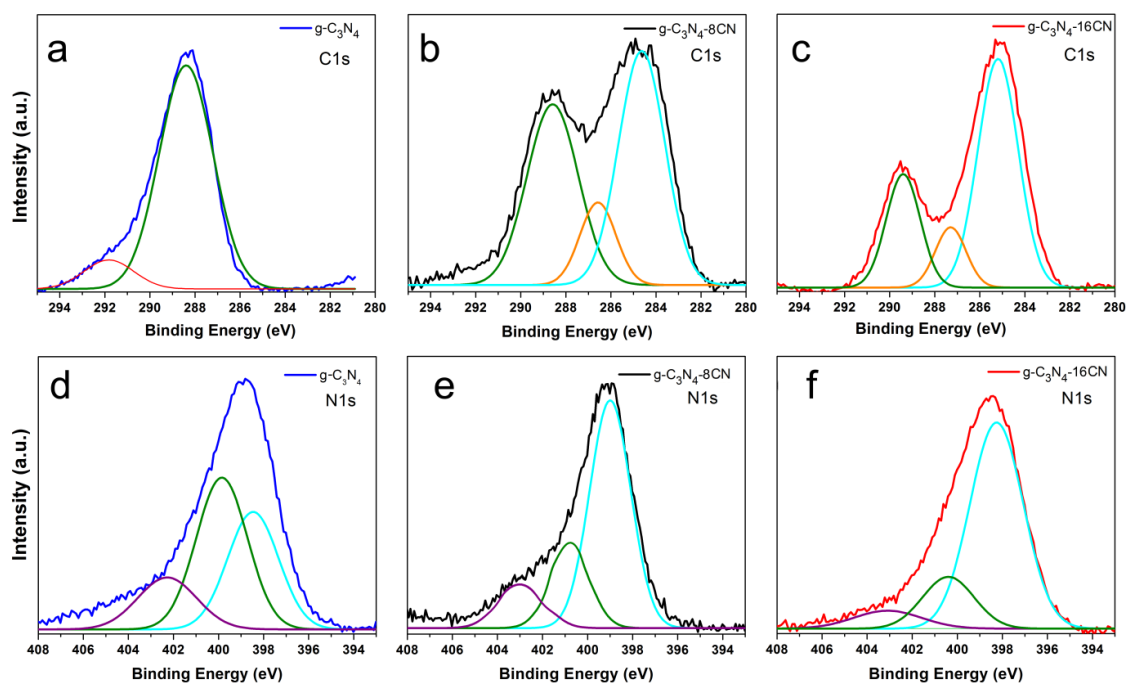


Figure 4.5 C 1s (a, b, c), N 1s (d, e, f) X-ray photoelectron spectroscopy (XPS) curves of g-C<sub>3</sub>N<sub>4</sub> (blue), g-C<sub>3</sub>N<sub>4</sub>-8CN (black), g-C<sub>3</sub>N<sub>4</sub>-16CN (red).

X-ray photoelectron spectroscopy (XPS) was employed to further analyze surface structural changes on the  $g\text{-C}_3\text{N}_4$  with the introduction of cyano group (Figure 4.5). For pristine  $g\text{-C}_3\text{N}_4$ , there is one main C1s peak with binding energy of 288.5 eV, which represents the carbon in triazine ring (N-C=N). After cyanation, two additional C1s peaks appear at 286.9 eV and 285.2 eV. They are, respectively, corresponding to the carbon atom in cyano group and the one in heptazine unit bonding with cyano group.<sup>[234, 235]</sup> The intensity of the additional peaks increases with the content of cyano group in the sample, strongly supporting that cyano group has been successfully grafted on carbon nitride scaffold. For the N1s curve (Figure 4.5), the broad peak contain 3 components with binding energy peak at 402 eV (hydrogenated nitrogen), 400 eV (charge depleted amine), and 398 eV (nitrogen in double bond and triple bond with carbon)<sup>[236]</sup>. With the increase of the cyano group content in the samples, the intensity of the peak at 398 eV is increasing, while the peak at 402 eV decreases. This again confirms that the amino group on the  $g\text{-C}_3\text{N}_4$  scaffold is successfully substituted by cyano group during photocatalytic cyanation process. Based on all those information and data, a simply schematic structures of  $g\text{-C}_3\text{N}_4\text{-xCN}$  and  $g\text{-C}_3\text{N}_4$  are shown in Figure 4.6, which shows the possible change in heptazine units in before and after the cyanation reaction.

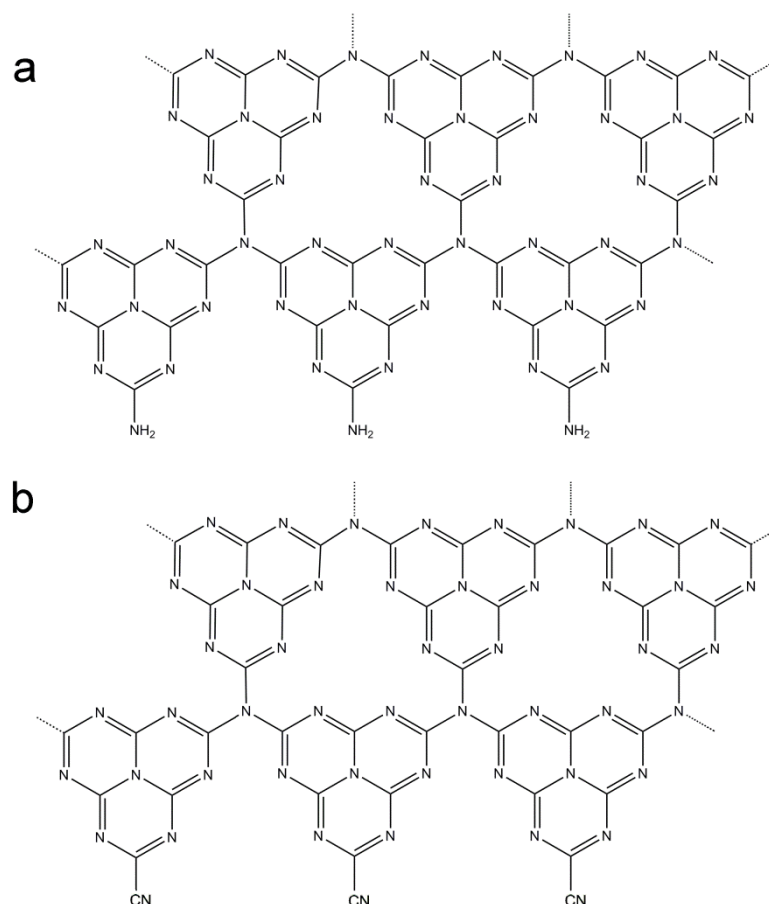


Figure 4.6 Proposed structural change in heptazine units in before (a) and after (b) the cyanation reaction.

Table 3.1 Results of g-C<sub>3</sub>N<sub>4</sub>-xCN preparation under different conditions

	oxygen	NaSCN	illumination	solvent	additives	products
1	+	+	+	ACN	-	+
2	-	+	+	ACN	-	-
3	+	-	+	ACN	-	-
4	+	+	-	ACN	-	-
5	+	+	+	ACN	TEMPO	-
6	+	+	+	DMF	-	-
7	+	+	+	EtOH	-	-

A series of control reactions were conducted for revealing the reaction mechanism of photocatalytic cyanation process. As shown in Table 4.1, light irradiation, NaSCN, and aerobic condition, are all prerequisites for the successful grafting of cyano group on the carbon nitride scaffold. This reaction was impeded by the addition of radical scavenger (TEMPO), which indicates that the cyanation reaction proceeded through a radical pathway. After the reaction, sulfate ions (SO<sub>4</sub><sup>2-</sup>), which is one of the products of the thiocyanate ion (SCN<sup>-</sup>) oxidation, are detected in inadequate washed materials. Together with the above spectroscopical analysis, we thus proposed a brief reaction mechanism. The aerobic photocatalytic oxidation of SCN<sup>-</sup> produces CN<sup>-</sup>, which could be converted to cyano radical by photo-induced hole. The cyano radicals can attack/recombine with the charged triazine ring and replace the amino group, releasing ammonium ions and affording cyanated carbon nitride.



#### 4.4 Band structures and photocatalysis performance of g-C<sub>3</sub>N<sub>4</sub>-xCN materials.

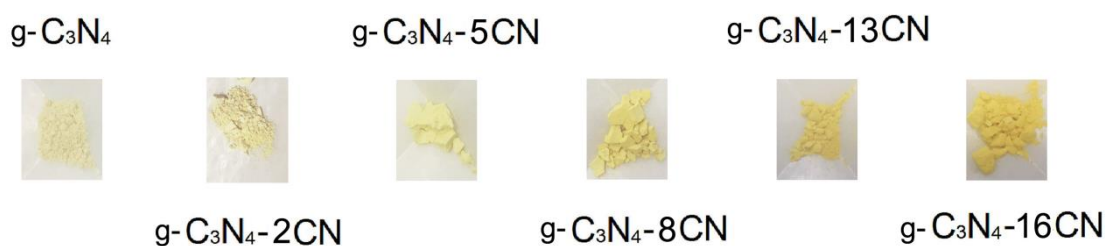


Figure 4.7 Photographs of the g-C<sub>3</sub>N<sub>4</sub>-xCN samples showing gradual color increase.

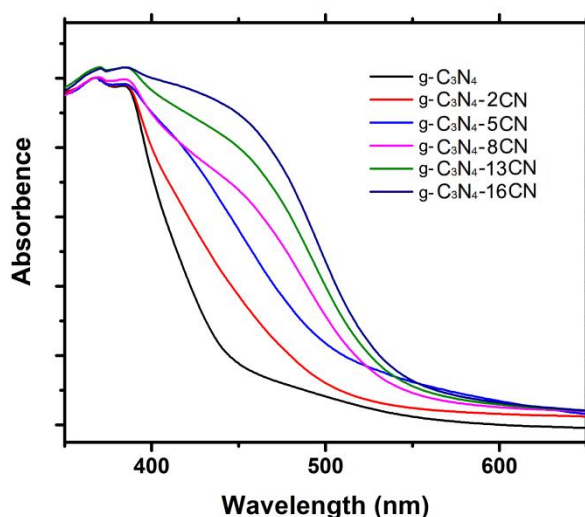


Figure 4.8 solid UV-Vis absorption spectra of the g-C<sub>3</sub>N<sub>4</sub>-xCN samples.

As the most obvious variation, it can be observed that the color of these samples change gradually from pale yellow to gold. The effect of the cyanation process on the visible light response of the materials was studied by UV-vis absorbance spectroscopy. As shown in Figure 4.8, the pristine g-C<sub>3</sub>N<sub>4</sub> has an absorption edge at around 450 nm, while a significant red shift of the absorption edges is observed for the samples with increasing cyano group content. For all, g-C<sub>3</sub>N<sub>4</sub>-xCN samples, a gradual significant red shift of the absorption edges with increasing C≡N contents is observed. The absorption edge of the sample g-C<sub>3</sub>N<sub>4</sub>-16CN extends to 590 nm, which is significant for a potential better coverage of the solar light spectrum. This means g-C<sub>3</sub>N<sub>4</sub>-xCN can also absorb green light and represents the success of g-C<sub>3</sub>N<sub>4</sub> modification *via* side chain substitution.



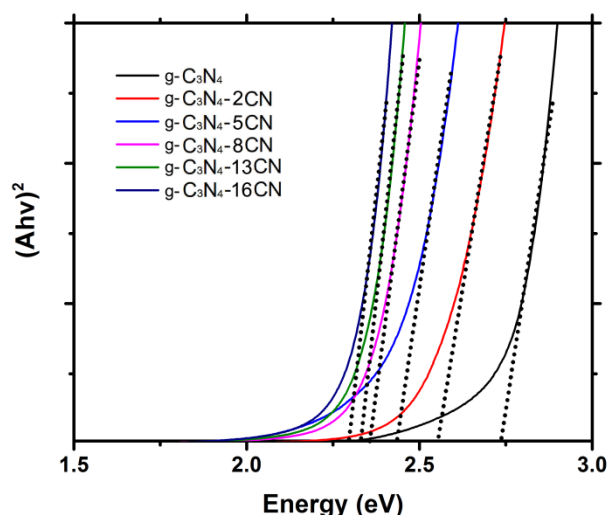


Figure 4.9 Tauc's plot for  $g\text{-C}_3\text{N}_4\text{-xCN}$  samples.

Based on the UV-Vis absorption spectra above, the optical bandgap of resulting  $g\text{-C}_3\text{N}_4\text{-xCN}$  can be calculated by the Tauc plot method. A Tauc plot is widely used method to determine the optical bandgap, or Tauc gap, in amorphous semiconductors. The resulting plot has a distinct linear range which denotes the onset of absorption. Thus, extrapolating this linear region to the abscissa yields the energy of the optical band gap of the material. The band gap of  $g\text{-C}_3\text{N}_4$  and  $g\text{-C}_3\text{N}_4\text{-xCN}$  were calculated and the results are as shown in Figure 4.9. As we can see, the band gap gradually decreases from 2.73 eV for the pristine  $g\text{-C}_3\text{N}_4$  to 2.29 eV for  $g\text{-C}_3\text{N}_4\text{-16CN}$ .

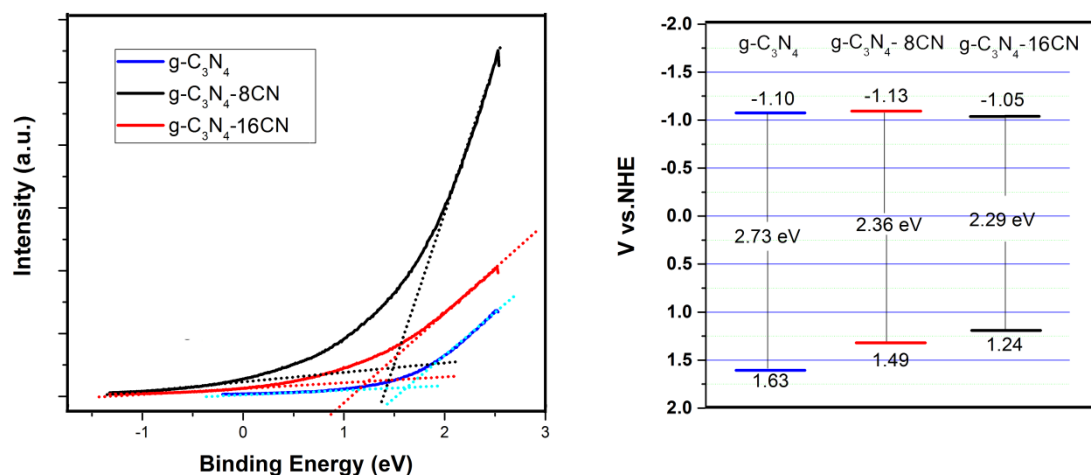


Figure 4.10 Ultraviolet photoelectron spectra (UPS, left) of  $g\text{-C}_3\text{N}_4$ ,  $g\text{-C}_3\text{N}_4\text{-8CN}$  and  $g\text{-C}_3\text{N}_4\text{-16CN}$ ; Scheme of the band gap structures (right) of  $g\text{-C}_3\text{N}_4$ ,  $g\text{-C}_3\text{N}_4\text{-8CN}$  and  $g\text{-C}_3\text{N}_4\text{-16CN}$ .

After the confirmation of band gap, it is necessary to affirm the exact valence band position of  $g\text{-C}_3\text{N}_4\text{-xCN}$  materials. To determine the valence band level, ultraviolet photoelectron spectroscopy (UPS) was used for these resulting materials. When absorbed ultraviolet photons, the tested samples can emit

photoelectrons. The kinetic energy spectra of photoelectrons can use to determine the position of valence bands from the intersection of line fitting of the valence band leading edge and the other line of the background. Here g-C<sub>3</sub>N<sub>4</sub>, g-C<sub>3</sub>N<sub>4</sub>-8CN and g-C<sub>3</sub>N<sub>4</sub>-16CN are selected as the representatives to show the change of valence band. As shown in Figure 4.10, the valence-band maximum (VBM) of g-C<sub>3</sub>N<sub>4</sub>, g-C<sub>3</sub>N<sub>4</sub>-8CN and g-C<sub>3</sub>N<sub>4</sub>-16CN are calculated to be 1.53, 1.41, and 1.24 V (vs. NHE), respectively. With the above mentioned band gap values in hand, the conduction band minimum (CBM) is thereby calculated to be -1.15, -0.95 and -1.05 V (vs. NHE). As a result, cyanation of the g-C<sub>3</sub>N<sub>4</sub> leads to the negative shift of the valence band maximum while keeping the conduction band minimum rather unchanged (Figure 4.10 b).

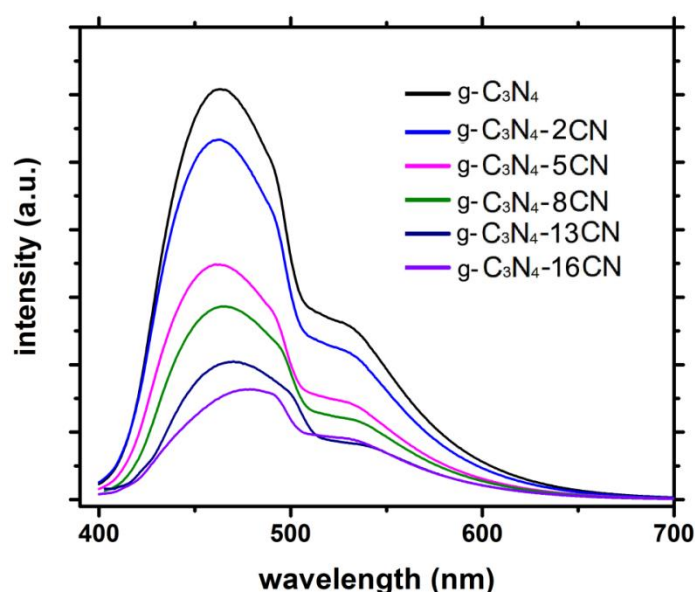
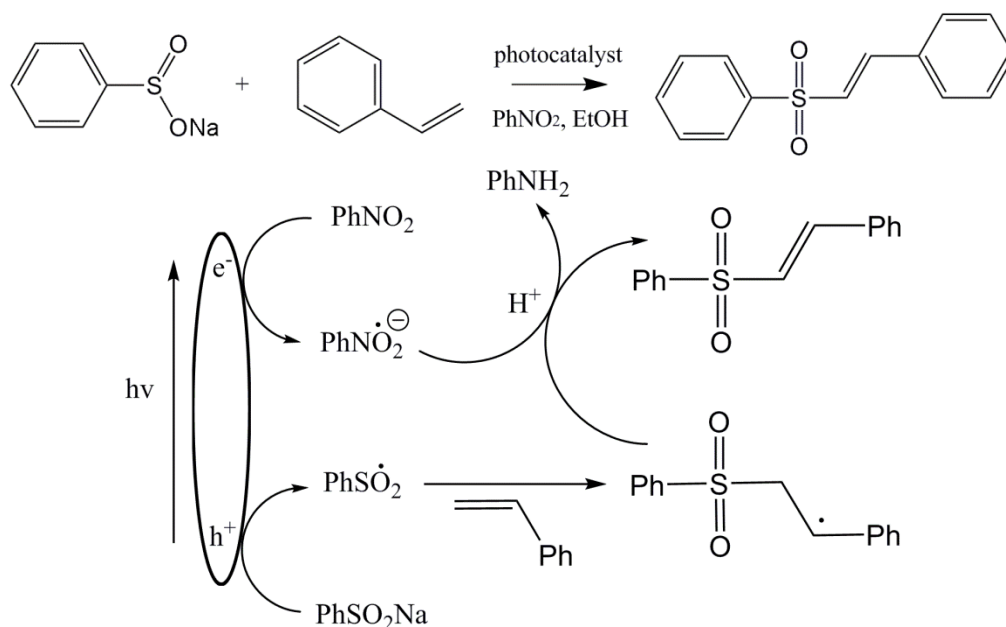


Figure 4.11 Photoluminescence spectra of g-C<sub>3</sub>N<sub>4</sub>-xCN materials.

As mentioned in Chapter 1.6, a too fast recombination process of photogenerated charges is an important reason for the low efficiency of photocatalysts. Therefore, photoluminescence (PL) measurements of g-C<sub>3</sub>N<sub>4</sub>-xCN are of additional value, which can clearly point out whether the radiative charge recombination process is inhibited or not. As shown in Figure 4.11, for g-C<sub>3</sub>N<sub>4</sub>, the strong PL emission at 470 nm shows a fast and rather efficient charge carrier recombination. After cyanation, the intensity of this emission peak is weakened. This implies that the cyanation reduces charge carrier recombination of these materials. This is potentially good for the photocatalytic reaction, which needs the charge carriers to initiate the photo-redox reaction. At the same time, the profile of the photoluminescence spectrum stays unchanged, which means that the higher positioned HOMO orbitals brought it by the nitriles are not really involved in radiative recombination. All those information speak for a rather stable localization

of the photogenerated charges by means of the cyano groups. It is thus reasonable to expect enhanced photocatalytic performance of the cyanated g-C<sub>3</sub>N<sub>4</sub>.



Scheme 4.1 Photocatalytic coupling reaction between styrene and benzenesulfinate sodium and its mechanism.<sup>[237] [238]</sup>

As reported, carbon nitride can be employed as a photo-redox catalyst for the light-induced sulfonylation of alkenes with sulfinate salts.<sup>[237]</sup> This photocatalytic reaction can widely proceed with various sulfonates and alkenes with good product yields. The excited photocatalyst can oxidize the sulfinate salt to its radical, while the photocatalyst itself forms a ground-state radical anion, which is re-oxidised by the nitrobenzene regenerating the photocatalyst.<sup>[237] [238]</sup> As a lowered recombination rate is favorable to such a photocatalytic reaction, the performance of the g-C<sub>3</sub>N<sub>4</sub>-xCN samples was therefore evaluated in the photocatalytic coupling reaction between styrene and sodium benzenesulfinate (Scheme 4.1).

In a typical photocatalytic experiment, sodium benzenesulfinate (0.05 mmol), styrene (0.017 mmol) nitrobenzene (NB, 0.034 mmol) and 20 mg photocatalyst are accurately weighted and added in to a 5 mL glass bottle with 3 mL EtOH as solvent. After full dissolution, the glass bottle was deposited under blue (445 nm) or green (520 nm) light illumination for 12 h. After that, 0.5 mL solution was taken for GC-MS measurements as well as for GC-FID measurements, from which the photocatalysis yield can be straightly calculated. During the experiments, all the steps are similar, only with the changes of catalysts and illumination source.

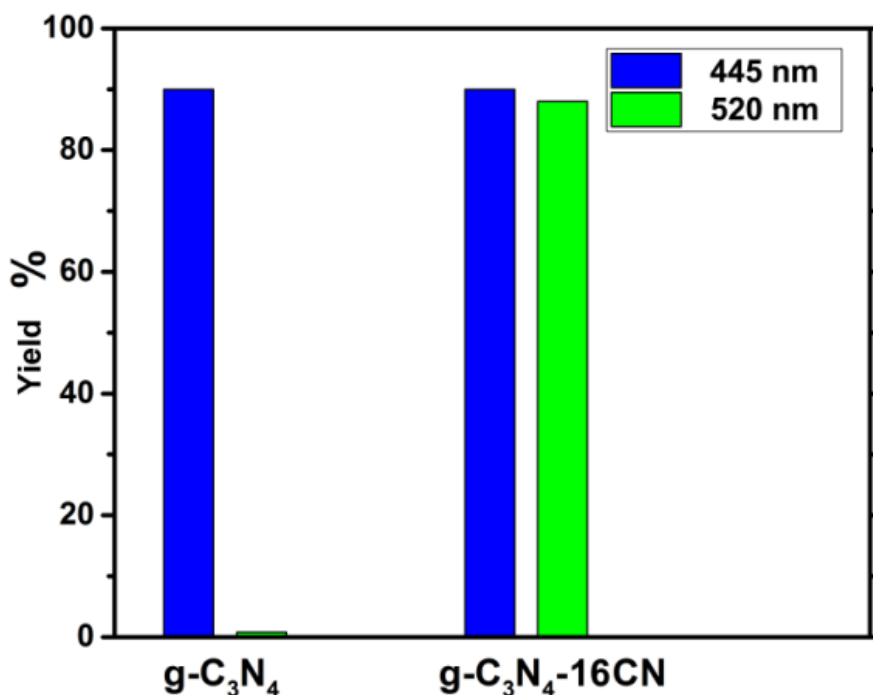


Figure 4.12 photocatalytic yields of g-C<sub>3</sub>N<sub>4</sub>, and g-C<sub>3</sub>N<sub>4</sub>-SCN under blue and green light illumination.

Under blue light (445 nm), both the pristine g-C<sub>3</sub>N<sub>4</sub> and g-C<sub>3</sub>N<sub>4</sub>-16CN show high performance. They could successfully couple the styrene and benzenesulfinate together with a yield at around 90 % (in terms of styrene conversion). When the photocatalytic reactions are irradiated by green light (520 nm), the reaction with g-C<sub>3</sub>N<sub>4</sub>-16 CN shows excellent yield of 88 %; while for the reaction with pristine g-C<sub>3</sub>N<sub>4</sub>, there is only a low conversion of 2 %. The great difference under green light illumination illustrates the influence of the cyanation of g-C<sub>3</sub>N<sub>4</sub>. Through that cyanation process, the light absorption range of g-C<sub>3</sub>N<sub>4</sub> is broadened, while staying a defined semiconductor with well accessible charges, which will greatly improve its solar-to-energy conversion efficiency.

#### 4.5 Conclusions

In this chapter, we for the first time propose a novel photocatalytic method for modifying the carbon nitride scaffold, by using sodium thiocyanate in acetonitrile as the cyano group source. The cyano group content in the sample could be easily controlled by the concentration of NaSCN. The cyanation modification takes place at former uncondensed amine groups and leads to a narrowed band gap as well as improved photo-induced charge carrier separation. The cyano group grafted carbon nitride shows a dramatically enhanced performance in mild photoredox reactions under green light, here exemplified by the photocatalytic coupling reaction between styrene and sodium benzenesulfinate, which is in stark contrast with the spectrally limited reactivity of pristine g-C<sub>3</sub>N<sub>4</sub>. This work not only offers a methodology for enhancing the visible light response of the carbon nitride materials, but also sheds light on the possibilities of designing novel carbon nitride materials by

attaching favorable donor and acceptor groups on the carbon nitride scaffold *via* chemical/photochemical reactions pathways.

## 5 Conclusions and outlooks

This thesis mainly focuses on the preparation of photoactive materials in novel methods based on the preparation of graphitic carbon nitride *via* supramolecular assembly. Three series of novel photocatalysts have been synthesized *via* utilizing different pre-compositions and post-modifications. These new methods successfully overcome some drawbacks of the pristine g-C<sub>3</sub>N<sub>4</sub>, such as high condensation temperature and a too restricted light absorption range.

In Chapter 2, inspired by carbon nitride preparation, a new supramolecular assembly was prepared *via* utilizing 2, 5-dihydroxy-1,4-benzoquinone (DBQ) to take the place of cyanuric acid in the supramolecular pre-monomer complex of polymeric carbon nitride. The complexes as well as its condensation products maintain sheet-like morphology, even up to high temperature of 800 °C. These materials cover the material classes of crystals, polymer frameworks and N-doped carbons. At a synthesis temperature as low as 250 °C, the product DBQ-M-250 shows good adsorption properties and good photoactive performance and, can successfully degrade methylene blue.

In Chapter 3, the acid monomer of the supramolecular complexes was further changed by using chlorine substitution (chloranilic acid, CLA). Highly ordered 1 D fiber-like structure materials were prepared instead of 2D sheet-like materials, because of the restriction to lateral growth. The optical and catalytic properties as well as the carbon and nitrogen ratio of the materials can be tuned according to the calcination temperature. Among all the obtained materials, CLA-M-250 condenses only on grain boundaries and its surfaces, which makes it a heterojunction semiconductor. This material shows the highest photocatalytic activity and strong oxidation capacity. It shows not only great photo-performance in RhB degradation, but also oxygen production in water splitting.

In the Chapter 4, the research focuses on the modification of photocatalyst in a post-modification instead of changing the primary composition. A novel photocatalytic method was proposed to modify a carbon nitride scaffold with cyano groups, whose content can be controlled by the input of sodium thiocyanate. The cyanation modification leads to narrowed band gap as well as improved photo-induced charge separation. Cyano group grafted carbon nitride thus shows dramatically enhanced performance in the photocatalytic coupling reaction between styrene and sodium benzenesulfinate under green light irradiation, which is in stark contrast with the inactivity of pristine g-C<sub>3</sub>N<sub>4</sub>.

In this thesis, all those materials exhibit a significant enhanced photocatalytic performance, and some of them are still with potential for further research. For example, CLA-M-250 is with a comparably strong oxidation power, but its water splitting efficiency is still very low. More attempts could be made to improve its photocatalysis performance by optimizing the oxidation cocatalyst. Besides, with the valence band (VB) of CLA-250 more positive than 1.763 eV vs. NHE, it is reasonable to employ it in more photocatalytic reactions. It is valuable research

topic to find out whether CLA-M-250 is capable in other relevant photocatalysis reactions and what kind of photocatalysis reaction can be realized with CLA-M-250. This is similar for the g-C<sub>3</sub>N<sub>4</sub>-16CN material prepared in Chapter 4. As modified, g-C<sub>3</sub>N<sub>4</sub> is expectable to be so reactive that it would be highly interesting to seek for whether this cyano group grafted photocatalyst can be employed in other usage. The work in this thesis to be understood is just as a start for these materials, which is expected to be followed by better performance and more results.

More importantly, the methods in this thesis are general and simple, and be extensively used in photocatalyst synthesis. It is reasonable to expect a further improvement of the performance of CN photoactive materials from both the pre-composition and the post-modification way.

It is to our opinion possible to obtain further different photocatalytic materials *via* supramolecular assembly but with more different initial monomers. This time, the attempts to modify monomers was limited to the replacement for cyanuric acid, but also the substitution of melamine can be considered. Various organic components can be utilized in approach, such as urea, cyanamide, oxamide, 1,3,5-tribenzenetriamine, piperazine, and benzoquinone dioxime. The new supramolecules as well as their condensation products will possess different properties, related to the introduction of more monomers. Within those variations, it is very likely to find new materials with even better photocatalytic performance for each specific reaction. More importantly, it is possible to utilize different monomers to synthesize CN materials with stereoscopic topology, which could possess high specific surface area, high structure stability, low gas resistance and a large number of exposed active sites for photo reactions.

The work of Chapter 4 sheds light on the possibilities of designing novel carbon nitride materials by attaching favorable functional groups on the carbon nitride scaffold *via* chemical/photochemical reactions pathways. In fact, there are a lot of references about the grafting of functional group to N including heterocycle *via* photo catalytic reaction. It is possible to try whether those methods can be used in g-C<sub>3</sub>N<sub>4</sub> modification. If so, these methods can be used to change the elemental composition and introduce modification into g-C<sub>3</sub>N<sub>4</sub>, which will lead to the improvement of photocatalysis efficiency. In general, this thesis brings two novel methods to effectively change photoactive material. I hope these innovative attempts can inspire more researchers in this area to prepare better photocatalysts, improve the photocatalysis efficiency and finally achieve widely commercial usage.





## 6 Appendix

### 6.1 Characterization methods

Powder X-Ray diffraction patterns were measured on a Bruker D8 Advance diffractometer equipped with a scintillation counter detector with CuK $\alpha$  radiation ( $\lambda = 0.15418$  nm) applying  $2\theta$  step size of  $0.05^\circ$  and counting time of 3s per step.

Elemental analysis was measured through combustion analysis with the Vario Micro device.

FT-IR spectra were recorded on a Varian1000 FT-IR spectrometer equipped with an attenuated total reflection unit with diamond applying a resolution of  $4\text{ cm}^{-1}$ .

Nitrogen adsorption/desorption measurements were performed after degassing the samples at  $150^\circ\text{C}$  for 20 hours using a Quantachrome Quadrasorb SI-MP porosimeter at  $77.4\text{ K}$ . The specific surface areas were calculated by applying the Brunauer-Emmett-Teller (BET) model to adsorption isotherms ( $\text{N}_2$  at  $77.4\text{ K}$ ) for  $0.05 < p/p_0 < 0.2$  using the QuadraWin 5.05 software package.

Optical absorbance spectra of powders were measured on a Shimadzu UV 2600 equipped with an integrating sphere. The absorption spectra of Methylene Blue and RhB solutions were recorded on a T70 UV/VIS spectrophotometer (PG instruments Ltd.).

The emission spectra were recorded on LS-50B, Perkin Elmer instrument. The excitation wavelength was  $350\text{ nm}$ . Time-resolved photoluminescence measurements were carried out at room temperature using Edinburgh Instruments (FLSP 920) system, equipped with a  $450\text{ W}$  xenon lamp as the excitation source.

SEM images were obtained on a LEO 1550-Gemini microscope. Shimadzu UV 2600 was used to reveal the optical absorbance spectra of powders. Energy disperse X-ray analysis and morphology observation by scanning electron microscope (SEM) were performed on JSM-7500F (JEOL) equipped with an Oxford Instruments X-MAX80 mm<sup>2</sup> detector.

Transmission electron microscopy (TEM) was performed by using an EM 912 Omega microscope at  $120\text{ kV}$ . Samples were prepared by depositing a drop of a suspension of particles in ethanol onto the amorphous carbon film. The structures of materials were also examined by transmission electron microscopy (TEM) using an EM 912 Omega microscope at  $120\text{ kV}$ .

The structures of materials were also examined by transmission electron microscopy (TEM) using an EM 912 Omega microscope at  $120\text{ kV}$ .

The high resolution Transmission electron microscopy images were acquired using a double-corrected Jeol ARM200F, equipped with a cold field emission gun. For the investigation, the acceleration

voltage was put to 200kV and a condenser aperture with a diameter of 20 $\mu$ m was used. With these settings, the microscope reaches a lattice resolution below 1Å. An attached Gatan GIF Quantum energy filter was used for the acquisition of the EELS measurements.

Elemental composition of products and chemical states of the surface elements were analyzed by X-ray photoelectron spectroscopy using ESCALab220i-XL electron spectrometer from VG Scientific and 300W AlK $\alpha$  radiation. For Chapter 4, the X-ray photoelectron spectroscopy was measured with CISSY equipment in ultra-high vacuum (UHV), with a SPECS XR 50 X ray gun Mg K $\alpha$  radiation and Combined Lens Analyser Module (CLAM ). All spectra were referenced to the C 1s peak of adventitious carbon at 284.8 eV. For quantification purposes, survey spectra at pass energy of 50 eV and high-resolution spectra at pass energy of 20eV were recorded and analysed by XPS Peak 4.1 software . The spectra were decomposed assuming line shapes as sum functions of Gaussian (80%) and Lorentzian (20%) functions.

Ultraviolet photoelectron spectroscopy (UPS) analyzed was carry out with CISSY equipment in ultra-high vacuum (UHV), with a excitation source of He I 21.2 eV radiation and UVS 10/35.

Zeta-potential measurements were performed using Zetasizer nano ZS, and the data analysis was conducted by using “Zetasizer” software.

TGA-MS measurement has been performed using a thermo microbalance TG 209 F1 Libra (Netzsch, Selb, Germany) coupled with a Thermostar Mass spectrometer (Pfeiffer Vacuum; Asslar/Germany) with a ionization energy of 75eV. A platinum crucible was used for the measurement of 10 mg of samples in a Helium flow of 10 mL/min and a purge flow of 10 mL/min. The samples have been heated with heat rate 2.5 K/min to 910 °C. Data have been recorded and analysed by the Proteus (6.0.0) and Quadstar (7.03, MID modus) software package.

Internal quantum efficiency was measured using Jasco-8300 fluorescence spectrometer equipped with ILF-835 100 mm integrating sphere. The sample was excited with 370 nm and the region 400-550 nm was used to calculate internal quantum efficiency.

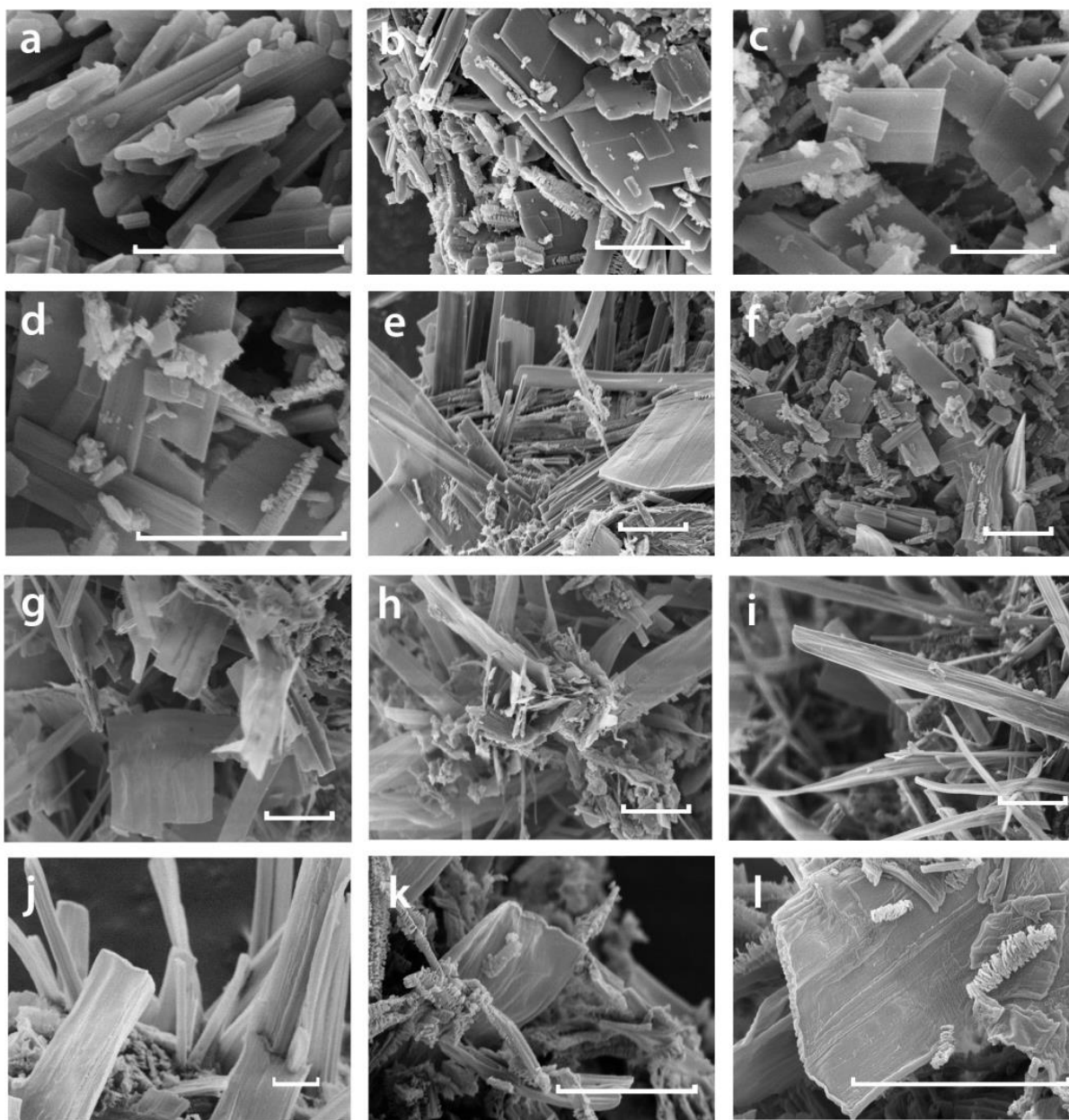
GC MS and GC FID measurement were conducted *via* Agilent 6890 Network GC System coupled with Agilent 5975 Inert Mass Selective

For oxygen production experiment, the content was monitored with oxygen dipping probe sensor from PreSens.

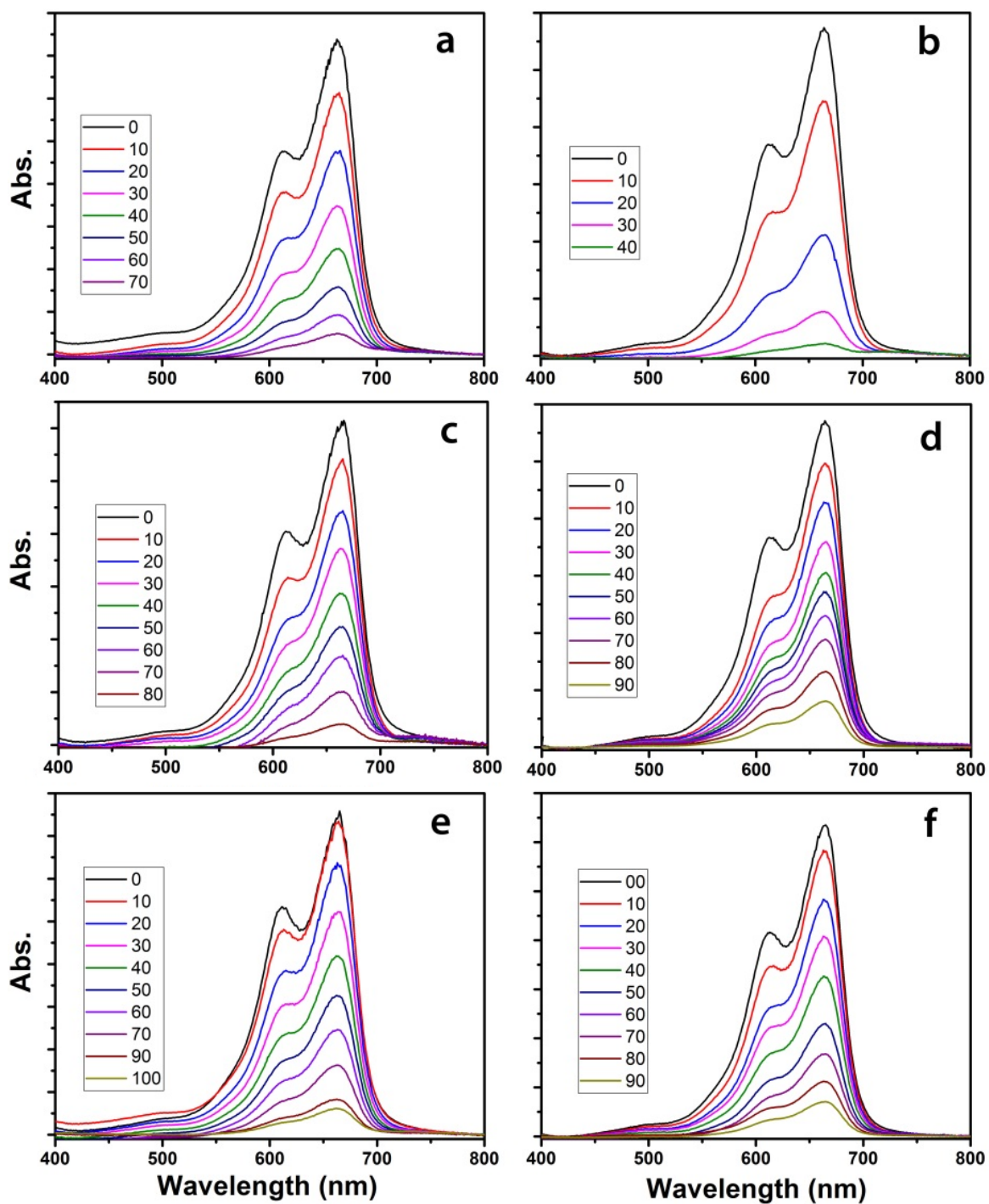
## 6.2 Supplementary information

Table A.1. Element weight percentage of the DBQ-M materials

Sample	N %	C %	H %	C/N mass ratio
B-DBQ-M	32.2	35.5	4.3	1.104
DBQ-M-150	33.6	38.2	4.2	1.182
DBQ-M-200	33.7	38.6	4.2	1.150
DBQ-M-250	31.7	42.8	3.3	1.340
DBQ-M-300	29.8	46.9	2.6	1.573
DBQ-M-350	27.4	44.9	3.1	1.643
DBQ-M-400	29.1	49.9	2.3	1.715
DBQ-M-480	29.0	52.9	2.4	1.824
DBQ-M-550	29.2	55.5	2.6	1.904
DBQ-M-600	28.4	26.4	2.4	1.987
DBQ-M-650	26.7	58.7	2.0	2.042
DBQ-M-700	24.6	62.0	2.3	2.527
DBQ-M-800	21.5	68.3	2.1	3.176



**Figure A1.** Scanning electron microscopy images of B-DBQ-M (a), DBQ-M-150 (b), DBQ-M-200 (c), DBQ-M-250 (d), DBQ-M-300 (e), DBQ-M-350 (f), DBQ-M-400(g), DBQ-M-480(h) DBQ-M-550(i), DBQ-M-600 (j), DBQ-M-700 (k) and DBQ-M-800 (l). The scale bars are equal to 3  $\mu\text{m}$ .



**Figure A2.** Degradation curves of MB with different catalysts. The catalysts are DBQ monomer (a), DBQ-M-150 (b), DBQ-M-250 (c), DBQ-M-350 (d), DBQ-M-480 (e), and DBQ-M-550 (f), respectively.

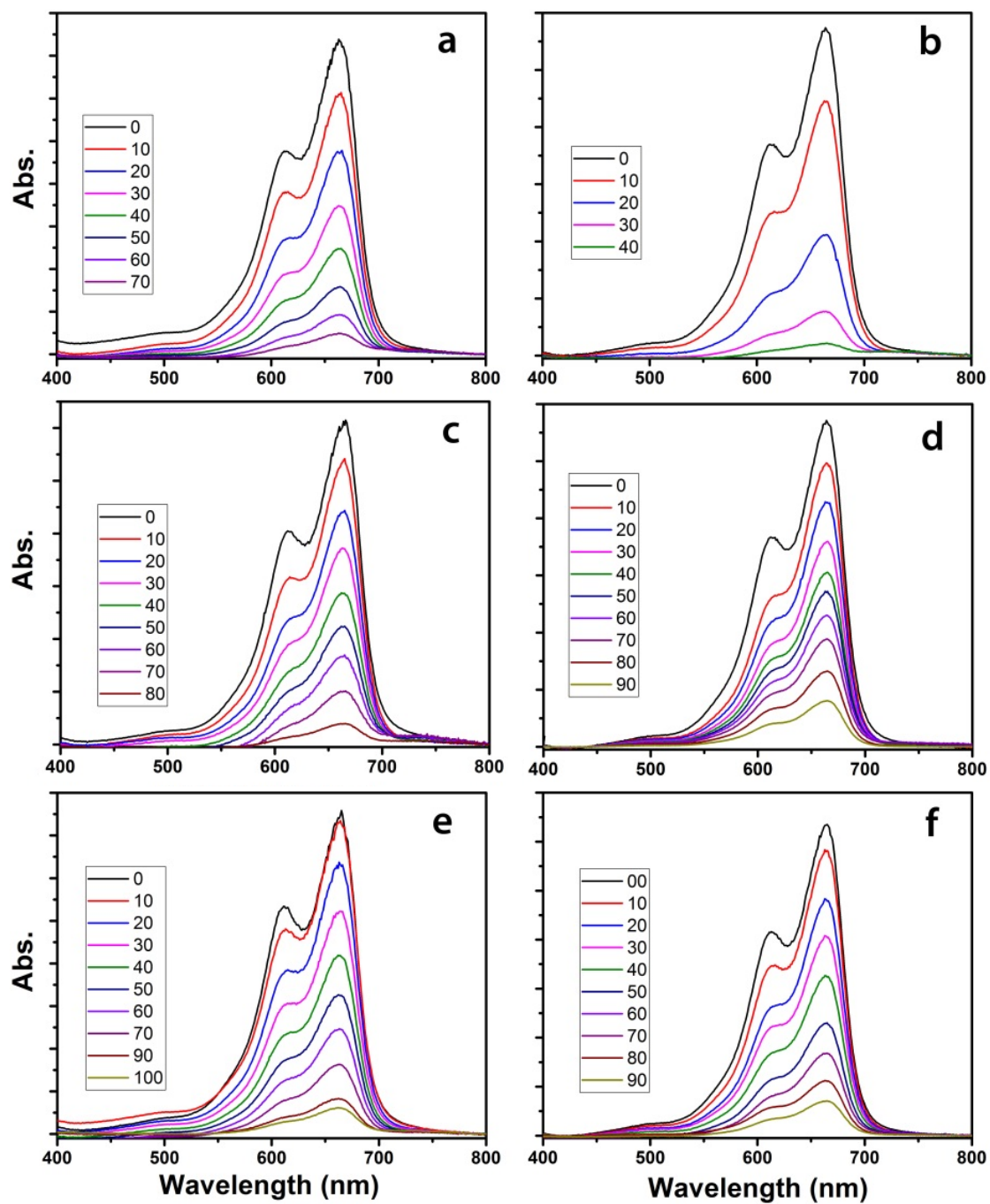


**Figure A3.** Comparison of MB degradation by DBQ-M-250 with different addition; (a) blank, (b) Ar purged, (c) O<sub>2</sub> purged, (d) methanol, (e) Ag ions, and (f) tert-Butanol.

Table A.2. Element weight percentage of the M-CLA materials

Sample	N %	C %	H %	C/N mass ratio
B-M-CLA	33.4	29.2	3.5	0.879
M-CLA-200	33.3	29.0	3.5	0.874
M-CLA-250	33.4	29.1	3.0	0.874
M-CLA-300	41.9	34.6	2.9	0.845
M-CLA-550	40.3	46.8	1.3	1.159
M-CLA-800	24.7	66.2	0	2.680

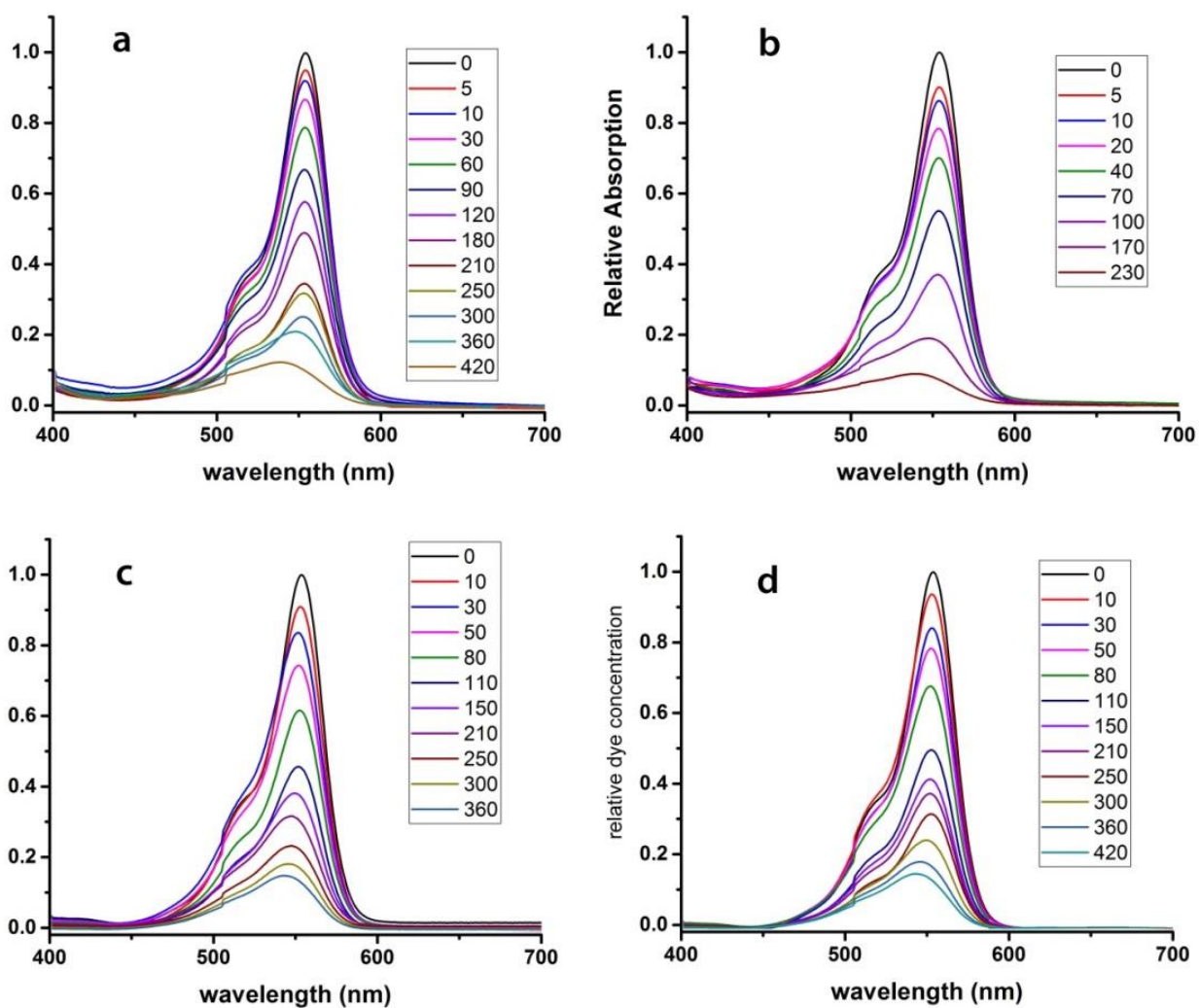


**Figure A4.** Degradation of RhB with CLA-M-200(a), CLA-M-250(b), CLA-M-300(c) and CLA-M-550(d) as Catalysts respectively.



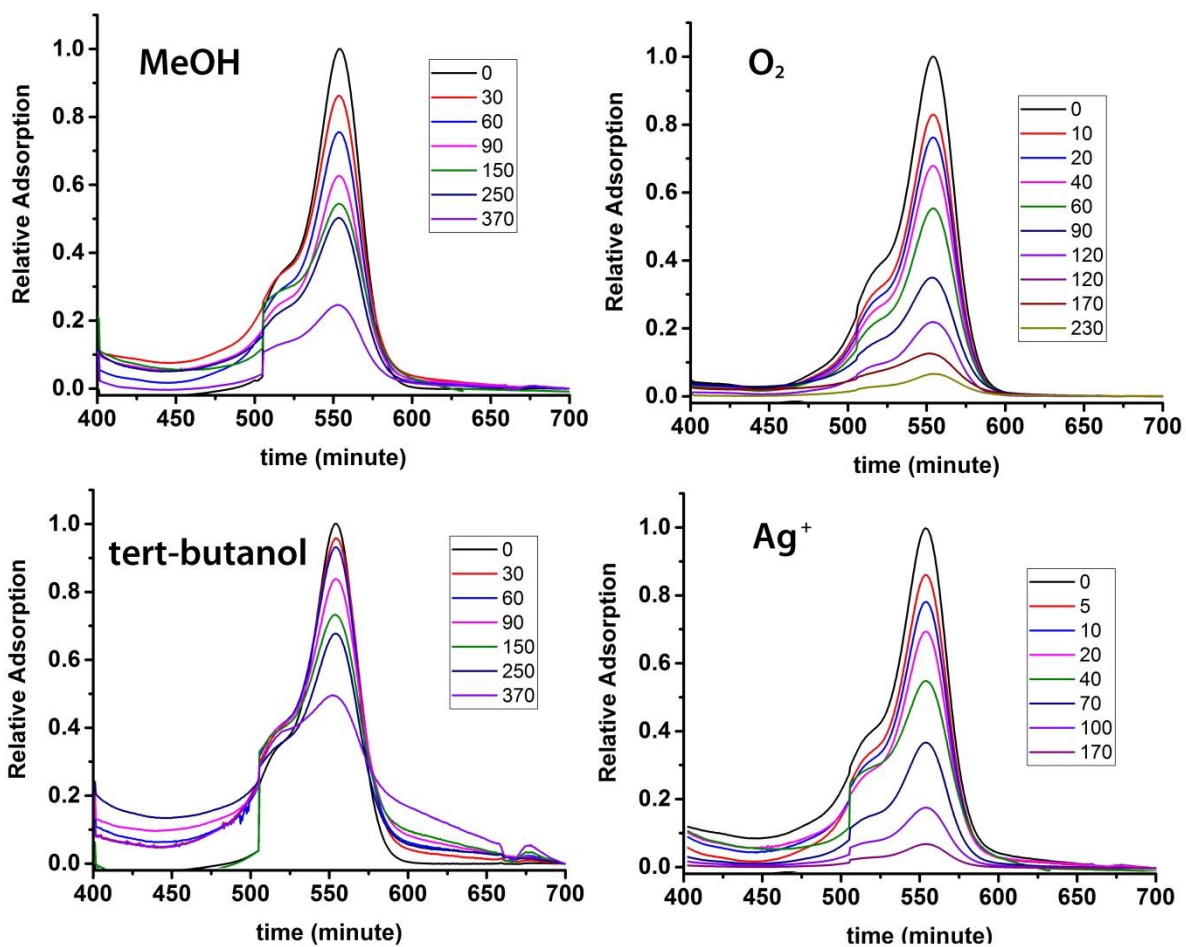


**Figure A5.** Photochemical RhB degradation curves with different additives. (CLA-M-250 as the catalyst).

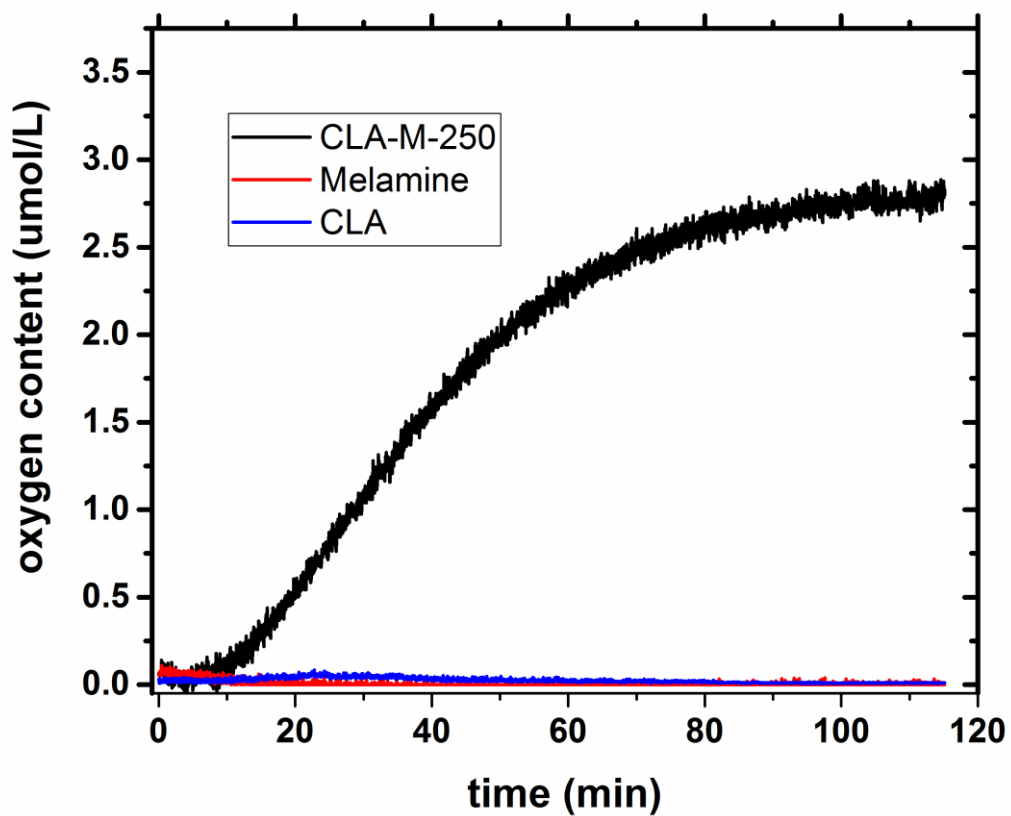


Figure A6. Comparison of oxygen production experiments with CLA-M-250 and that with monomers.

Table A.3. Element weight percentage of the g-C<sub>3</sub>N<sub>4</sub>-xCN materials

Sample	C %	N %	H %	S%	C/N mass ratio
g-C <sub>3</sub> N <sub>4</sub>	34.8	58.8	3.4	0.6	0.581
g-C <sub>3</sub> N <sub>4</sub> -2CN	34.6	58.5	3.5	0.8	0.592
g-C <sub>3</sub> N <sub>4</sub> -5CN	35.4	58.3	3.0	1.2	0.607
g-C <sub>3</sub> N <sub>4</sub> -8CN	36.1	58.1	2.9	0.7	0.621
g-C <sub>3</sub> N <sub>4</sub> -13CN	37.2	56.9	2.3	0.5	0.653
g-C <sub>3</sub> N <sub>4</sub> -16CN	37.6	56.6	2.0	1.0	0.664

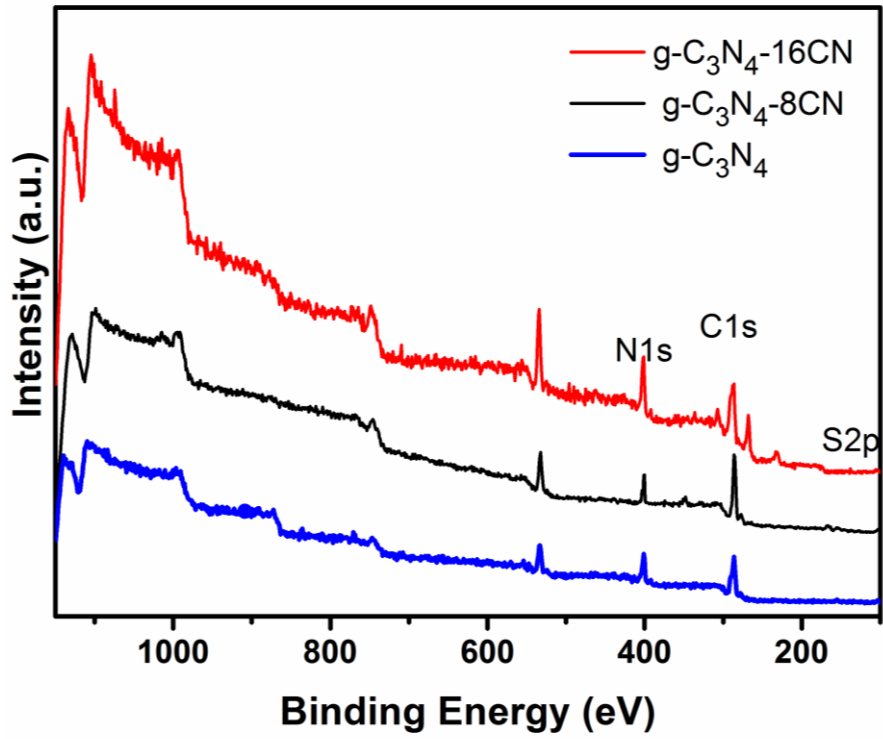
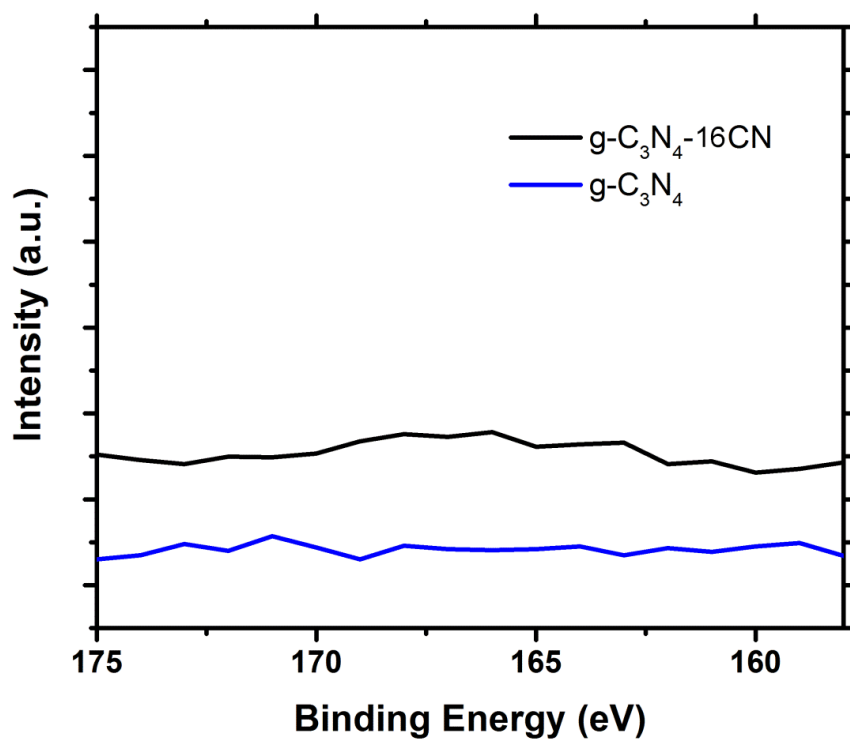


Figure A7. XPS overview curves of g-C<sub>3</sub>N<sub>4</sub>-16CN and g-C<sub>3</sub>N<sub>4</sub>.



**Figure A8.** XPS S 2p curves of g-C<sub>3</sub>N<sub>4</sub>-16CN and g-C<sub>3</sub>N<sub>4</sub>.

## 7 Acknowledgment

In the first place, I send Prof. Dr. Markus Antonietti my deep gratitude for providing me the great opportunity to work in Max-Planck-Institute for Colloid and interfaces and his significant support and help in my research and thesis completion.

Besides, I would like to thank Prof. Dr. Menny Shalom, who took me in the area of photocatalysis. During the research together, he inspired, encouraged, supported and helped me a lot. The works in Chapter 2 and 3 of this thesis benefit from our meaningful discussion, his suggestions and responsible supervision.

Moreover, I sincerely thank Dr. Yubao Zhao for his patient guidance and timely discussions in science. His extensive knowledge structure indeed helps me grasp every possible opportunity, in case of it slipping away. As the mentor for my Chapter 4, he contributes to the organization and guidance of that project.

Also, I am very grateful for the help from Heike Runge, Rona Pitschke, Jesus Barrio, Daniel Cruz, Antje Voelkel, and Tobias Heil. They are acknowledged for TEM, SEM, XPS, UPS, TGA-MS measurements, as well as the technical support and their general help.

Then, I would like thank Dr. Guigang Zhang, Daniel Cruz, Dr. Oleksandr Savatieiev, Dr Jingsan Xu and Dr. Wenyao Zhang, Katharina Otto. As colleges in the same group, they are always nice with me and helped me during my overseas study life. I wish them all the best for their future.

Additionally, I would like to thank all the other persons who I possibly forgot to mention here, but, who also generated an amazing working environment.

Finally, many thanks go to my family, my friends for their encouragement. They help me survive the most difficult days and the moments when I want to give it up. The thesis on hand would not have been possible without their supports.

## 8 References

- [1] M.L. Bacci, A concise history of world population, John Wiley & Sons2017.
- [2] United Nation DESA/POPULATION DIVISION, 2017 Revision of World Population Prospects (2017).
- [3] T. Covert, M. Greenstone, C.R. Knittel, The Journal of Economic Perspectives, 30 (2016) 117-137.
- [4] J.H. Seinfeld, S.N. Pandis, Atmospheric chemistry and physics: from air pollution to climate change, John Wiley & Sons2016.
- [5] L.D. Roper, Future World Energy, <http://www.roperld.com/science/energyfuture.htm>.
- [6] U.S. Energy Information Administration, Annual Energy Outlook 2017 (2017).
- [7] N.S. Lewis, D.G. Nocera, Proceedings of the National Academy of Sciences, 103 (2006) 15729-15735.
- [8] A.W. Kaplan, Technovation, 19 (1999) 467-481.
- [9] H. Buchberg, I. Catton, D. Edwards, Journal of Heat Transfer, 98 (1976) 182-188.
- [10] V. Gold, K. Loening, A. McNaught, P. Shemi, Blackwell Science, Oxford, (1997).
- [11] K. Glusac, What has light ever done for chemistry?, Nature Research, 2016.
- [12] A. Alias, Z. Zabidi, A. Ali, M. Harun, M. Yahya, International Journal of Applied Science and Technology, 3 (2013).
- [13] S. Tschierlei, M. Karnahl, M. Presselt, B. Dietzek, J. Guthmuller, L. González, M. Schmitt, S. Rau, J. Popp, Angewandte Chemie International Edition, 49 (2010) 3981-3984.
- [14] C.E.W. Wayne, R. P., Photochemistry, Oxford University Press, Oxford, United Kingdom, 2005.
- [15] L.-J. FAN, W.E. Jones Jr, Photochemistry and Photophysics of Polymeric Materials, (2010) 1.
- [16] N.J. Turro, Modern molecular photochemistry, University science books1991.
- [17] S.L. Murov, I. Carmichael, G.L. Hug, Handbook of photochemistry, CRC Press1993.
- [18] N. Serpone, E. Pelizzetti, Photocatalysis: fundamentals and applications, Wiley-Interscience1989.
- [19] M.A. Fox, M.T. Dulay, Chemical reviews, 93 (1993) 341-357.
- [20] P.C. Kamer, D. Vogt, J.W. Thybaut, Contemporary Catalysis: Science, Technology and Applications, Royal Society of Chemistry2017.
- [21] J. FentonH, Journal of the Chemical Society, Transactions, 65 (1894) 899-910.
- [22] M. Hayyan, M.A. Hashim, I.M. AlNashef, Chemical reviews, 116 (2016) 3029-3085.
- [23] M. Tamimi, S. Qourzal, N. Barka, A. Assabbane, Y. Ait-Ichou, Separation and Purification Technology, 61 (2008) 103-108.
- [24] A.L. Linsebigler, G. Lu, J.T. Yates Jr, Chemical reviews, 95 (1995) 735-758.
- [25] A. Fujishima, T.N. Rao, D.A. Tryk, Journal of Photochemistry and Photobiology C: Photochemistry Reviews, 1 (2000) 1-21.
- [26] Y. Qu, X. Duan, Chemical Society Reviews, 42 (2013) 2568-2580.

- [27] J. Salafsky, W. Lubberhuizen, R. Schropp, *Chemical physics letters*, 290 (1998) 297-303.
- [28] A.O. Ibhadon, P. Fitzpatrick, *Catalysts*, 3 (2013) 189-218.
- [29] M.R. Hoffmann, S.T. Martin, W. Choi, D.W. Bahnemann, *Chemical reviews*, 95 (1995) 69-96.
- [30] S. Fukuzumi, D. Hong, *European Journal of Inorganic Chemistry*, 2014 (2014) 645-659.
- [31] G. Hutchings, *Nanocatalysis: Synthesis and applications*, John Wiley & Sons 2013.
- [32] A. Fujishima, K. Honda, *nature*, 238 (1972) 37-38.
- [33] K. Hashimoto, H. Irie, A. Fujishima, *Japanese journal of applied physics*, 44 (2005) 8269.
- [34] T.-D. Nguyen-Phan, A.E. Baber, J.A. Rodriguez, S.D. Senanayake, *Applied Catalysis A: General*, 518 (2016) 18-47.
- [35] J.H. Carey, J. Lawrence, H.M. Tosine, *Bulletin of Environmental Contamination and Toxicology*, 16 (1976) 697-701.
- [36] T. Kawai, T. Sakata, *Nature*, 286 (1980) 474-476.
- [37] S.N. Frank, A.J. Bard, *Journal of the American Chemical Society*, 99 (1977) 303-304.
- [38] A. Anglada, A. Urtiaga, I. Ortiz, *Journal of Chemical Technology and Biotechnology*, 84 (2009) 1747-1755.
- [39] O. Legrini, E. Oliveros, A. Braun, *Chemical reviews*, 93 (1993) 671-698.
- [40] T. Inoue, A. Fujishima, S. Konishi, K. Honda, *Nature*, 277 (1979) 637-638.
- [41] W.-J. Ong, S.-Y. Voon, L.-L. Tan, B.T. Goh, S.-T. Yong, S.-P. Chai, *Industrial & Engineering Chemistry Research*, 53 (2014) 17333-17344.
- [42] T. Zhang, W. Lin, *Chemical Society Reviews*, 43 (2014) 5982-5993.
- [43] N. Zhang, Y.-J. Xu, *CrystEngComm*, 18 (2016) 24-37.
- [44] L. Jing, W. Zhou, G. Tian, H. Fu, *Chemical Society Reviews*, 42 (2013) 9509-9549.
- [45] D.J. Martin, G. Liu, S.J. Moniz, Y. Bi, A.M. Beale, J. Ye, J. Tang, *Chemical Society Reviews*, 44 (2015) 7808-7828.
- [46] F. Xu, Y. Shen, L. Sun, H. Zeng, Y. Lu, *Nanoscale*, 3 (2011) 5020-5025.
- [47] X. Bai, L. Wang, R. Zong, Y. Lv, Y. Sun, Y. Zhu, *Langmuir*, 29 (2013) 3097-3105.
- [48] X. Zhou, Q. Xu, W. Lei, T. Zhang, X. Qi, G. Liu, K. Deng, J. Yu, *Small*, 10 (2014) 674-679.
- [49] S. Han, L. Hu, Z. Liang, S. Wageh, A.A. Al - Ghamdi, Y. Chen, X. Fang, *Advanced Functional Materials*, 24 (2014) 5719-5727.
- [50] Q. Li, X. Li, S. Wageh, A. Al - Ghamdi, J. Yu, *Advanced Energy Materials*, 5 (2015).
- [51] J. Chen, X.J. Wu, L. Yin, B. Li, X. Hong, Z. Fan, B. Chen, C. Xue, H. Zhang, *Angewandte Chemie International Edition*, 54 (2015) 1210-1214.
- [52] C. Li, G. Chen, J. Sun, J. Rao, Z. Han, Y. Hu, Y. Zhou, (2015).
- [53] J. Zhu, F. Fan, R. Chen, H. An, Z. Feng, C. Li, *Angewandte Chemie International Edition*, 54 (2015) 9111-9114.



- [54] A.V. Akimov, R. Asahi, R. Jinnouchi, O.V. Prezhdo, *Journal of the American Chemical Society*, 137 (2015) 11517-11525.
- [55] S. Chen, S. Shen, G. Liu, Y. Qi, F. Zhang, C. Li, *Angewandte Chemie International Edition*, 54 (2015) 3047-3051.
- [56] W.-J. Ong, L.-L. Tan, Y.H. Ng, S.-T. Yong, S.-P. Chai, *Chem. Rev.*, 116 (2016) 7159-7329.
- [57] H. Zhang, X. Zuo, H. Tang, G. Li, Z. Zhou, *Physical Chemistry Chemical Physics*, 17 (2015) 6280-6288.
- [58] X. Wang, S. Blechert, M. Antonietti, *Acs Catalysis*, 2 (2012) 1596-1606.
- [59] F. Dong, L. Wu, Y. Sun, M. Fu, Z. Wu, S. Lee, *Journal of Materials Chemistry*, 21 (2011) 15171-15174.
- [60] J. Liebig, *European Journal of Organic Chemistry*, 10 (1834) 1-47.
- [61] E.C. Franklin, *Journal of the American Chemical Society*, 44 (1922) 486-509.
- [62] J.v. Liebig, *Ann. Pharm*, 10 (1834).
- [63] F. Goettmann, A. Fischer, M. Antonietti, A. Thomas, *Chemical communications*, (2006) 4530-4532.
- [64] X. Chen, J. Zhang, X. Fu, M. Antonietti, X. Wang, *Journal of the American Chemical Society*, 131 (2009) 11658-11659.
- [65] Y. Zheng, J. Liu, J. Liang, M. Jaroniec, S.Z. Qiao, *Energy & Environmental Science*, 5 (2012) 6717-6731.
- [66] M.L. Cohen, *Physical Review B*, 32 (1985) 7988.
- [67] Y. Zheng, L. Lin, B. Wang, X. Wang, *Angewandte Chemie International Edition*, 54 (2015) 12868-12884.
- [68] F. Dong, Z. Zhao, T. Xiong, Z. Ni, W. Zhang, Y. Sun, W.-K. Ho, *ACS applied materials & interfaces*, 5 (2013) 11392-11401.
- [69] J.L. Corkill, M.L. Cohen, *Physical Review B*, 48 (1993) 17622.
- [70] M.J. Bojdys, (2009).
- [71] J. Hong, X. Xia, Y. Wang, R. Xu, *Journal of Materials Chemistry*, 22 (2012) 15006-15012.
- [72] Y. Cui, J. Zhang, G. Zhang, J. Huang, P. Liu, M. Antonietti, X. Wang, *Journal of materials chemistry*, 21 (2011) 13032-13039.
- [73] J. Zhang, J. Sun, K. Maeda, K. Domen, P. Liu, M. Antonietti, X. Fu, X. Wang, *Energy & Environmental Science*, 4 (2011) 675-678.
- [74] J. Xu, H.-T. Wu, X. Wang, B. Xue, Y.-X. Li, Y. Cao, *Physical Chemistry Chemical Physics*, 15 (2013) 4510-4517.
- [75] K. Gibson, J. Glaser, E. Milke, M. Marzini, S. Tragl, M. Binnewies, H.A. Mayer, H.-J. Meyer, *Materials Chemistry and Physics*, 112 (2008) 52-56.

- [76] Y. Zhao, Z. Liu, W. Chu, L. Song, Z. Zhang, D. Yu, Y. Tian, S. Xie, L. Sun, *Advanced Materials*, 20 (2008) 1777-1781.
- [77] Q. Tay, P. Kanhere, C.F. Ng, S. Chen, S. Chakraborty, A.C.H. Huan, T.C. Sum, R. Ahuja, Z. Chen, *Chemistry of Materials*, 27 (2015) 4930-4933.
- [78] C. Ewels, M. Glerup, *Journal of nanoscience and nanotechnology*, 5 (2005) 1345-1363.
- [79] M. Humayun, Y. Qu, F. Raziq, R. Yan, Z. Li, X. Zhang, L. Jing, *Environmental science & technology*, 50 (2016) 13600-13610.
- [80] J. Zhang, G. Zhang, X. Chen, S. Lin, L. Möhlmann, G. Dołęga, G. Lipner, M. Antonietti, S. Blechert, X. Wang, *Angewandte Chemie*, 124 (2012) 3237-3241.
- [81] Y. Wang, X. Wang, M. Antonietti, *Angewandte Chemie International Edition*, 51 (2012) 68-89.
- [82] A. Thomas, A. Fischer, F. Goettmann, M. Antonietti, J.-O. Müller, R. Schlögl, J.M. Carlsson, *Journal of Materials Chemistry*, 18 (2008) 4893-4908.
- [83] C. Zhang, Y. Xiao, D. Liu, Q. Yang, C. Zhong, *Chemical Communications*, 49 (2013) 600-602.
- [84] J. Xu, T.J. Brenner, L. Chabanne, D. Neher, M. Antonietti, M. Shalom, *Journal of the American Chemical Society*, 136 (2014) 13486-13489.
- [85] X. Wang, K. Maeda, A. Thomas, K. Takanaabe, G. Xin, J.M. Carlsson, K. Domen, M. Antonietti, *Nature materials*, 8 (2009) 76-80.
- [86] P. Wu, J. Wang, J. Zhao, L. Guo, F.E. Osterloh, *Chemical Communications*, 50 (2014) 15521-15524.
- [87] H. Wang, X. Zhang, J. Xie, J. Zhang, P. Ma, B. Pan, Y. Xie, *Nanoscale*, 7 (2015) 5152-5156.
- [88] G. Dong, K. Zhao, L. Zhang, *Chemical Communications*, 48 (2012) 6178-6180.
- [89] S. Yan, Z. Li, Z. Zou, *Langmuir*, 25 (2009) 10397-10401.
- [90] G. Liu, P. Niu, C. Sun, S.C. Smith, Z. Chen, G.Q. Lu, H.-M. Cheng, *Journal of the American Chemical Society*, 132 (2010) 11642-11648.
- [91] S. Zhang, J. Li, X. Wang, Y. Huang, M. Zeng, J. Xu, *ACS applied materials & interfaces*, 6 (2014) 22116-22125.
- [92] X. Chang, T. Wang, J. Gong, *Energy & Environmental Science*, 9 (2016) 2177-2196.
- [93] B. Kumar, M. Llorente, J. Froehlich, T. Dang, A. Sathrum, C.P. Kubiak, *Annual review of physical chemistry*, 63 (2012) 541-569.
- [94] H.W. Nasution, E. Purnama, S. Kosela, J. Gunlazuardi, *Catalysis Communications*, 6 (2005) 313-319.
- [95] G. Zhang, Z.A. Lan, X. Wang, *ChemCatChem*, 7 (2015) 1422-1423.
- [96] Y. Wang, Y. Xu, Y. Wang, H. Qin, X. Li, Y. Zuo, S. Kang, L. Cui, *Catalysis Communications*, 74 (2016) 75-79.
- [97] G. Dong, L. Zhang, *Journal of Materials Chemistry*, 22 (2012) 1160-1166.

- [98] P. Niu, Y. Yang, C.Y. Jimmy, G. Liu, H.-M. Cheng, *Chemical Communications*, 50 (2014) 10837-10840.
- [99] S.-W. Cao, X.-F. Liu, Y.-P. Yuan, Z.-Y. Zhang, Y.-S. Liao, J. Fang, S.C.J. Loo, T.C. Sum, C. Xue, *Applied Catalysis B: Environmental*, 147 (2014) 940-946.
- [100] K. Wang, Q. Li, B. Liu, B. Cheng, W. Ho, J. Yu, *Applied Catalysis B: Environmental*, 176 (2015) 44-52.
- [101] J. Qin, S. Wang, H. Ren, Y. Hou, X. Wang, *Applied Catalysis B: Environmental*, 179 (2015) 1-8.
- [102] S. Zhou, Y. Liu, J. Li, Y. Wang, G. Jiang, Z. Zhao, D. Wang, A. Duan, J. Liu, Y. Wei, *Applied Catalysis B: Environmental*, 158 (2014) 20-29.
- [103] G. Gao, Y. Jiao, E.R. Waclawik, A. Du, *Journal of the American Chemical Society*, 138 (2016) 6292-6297.
- [104] G. Sahara, H. Kumagai, K. Maeda, N. Kaeffer, V. Artero, M. Higashi, R. Abe, O. Ishitani, *Journal of the American Chemical Society*, 138 (2016) 14152-14158.
- [105] U.I. Gaya, A.H. Abdullah, *Journal of Photochemistry and Photobiology C: Photochemistry Reviews*, 9 (2008) 1-12.
- [106] D. Chatterjee, S. Dasgupta, *Journal of Photochemistry and Photobiology C: Photochemistry Reviews*, 6 (2005) 186-205.
- [107] T. Sano, S. Tsutsui, K. Koike, T. Hirakawa, Y. Teramoto, N. Negishi, K. Takeuchi, *Journal of materials chemistry A*, 1 (2013) 6489-6496.
- [108] T.L. Thompson, J.T. Yates, *Chemical Reviews*, 106 (2006) 4428-4453.
- [109] Y. Yang, Y. Guo, F. Liu, X. Yuan, Y. Guo, S. Zhang, W. Guo, M. Huo, *Applied Catalysis B: Environmental*, 142 (2013) 828-837.
- [110] S. Chen, Y. Hu, S. Meng, X. Fu, *Applied Catalysis B: Environmental*, 150 (2014) 564-573.
- [111] Q. Liu, Y. Guo, Z. Chen, Z. Zhang, X. Fang, *Applied Catalysis B: Environmental*, 183 (2016) 231-241.
- [112] K. Li, L. Yan, Z. Zeng, S. Luo, X. Luo, X. Liu, H. Guo, Y. Guo, *Applied Catalysis B: Environmental*, 156 (2014) 141-152.
- [113] M.N. Chong, B. Jin, C.W. Chow, C. Saint, *Water research*, 44 (2010) 2997-3027.
- [114] D. Friedmann, A. Hakki, H. Kim, W. Choi, D. Bahnemann, *Green Chemistry*, 18 (2016) 5391-5411.
- [115] F. Su, S.C. Mathew, L. Möhlmann, M. Antonietti, X. Wang, S. Blechert, *Angewandte Chemie International Edition*, 50 (2011) 657-660.
- [116] F. Su, S.C. Mathew, G. Lipner, X. Fu, M. Antonietti, S. Blechert, X. Wang, *Journal of the American Chemical Society*, 132 (2010) 16299-16301.
- [117] P. Zhang, Y. Wang, H. Li, M. Antonietti, *Green Chemistry*, 14 (2012) 1904-1908.
- [118] Z. Zheng, X. Zhou, *Chinese Journal of Chemistry*, 30 (2012) 1683-1686.

- [119] Y. Zhao, M. Antonietti, *Angewandte Chemie*, (2017).
- [120] J. Guo, Z. Gan, Z. Lu, J. Liu, J. Xi, Y. Wan, L. Le, H. Liu, J. Shi, R. Xiong, *Journal of Applied Physics*, 114 (2013) 104903.
- [121] R. Abe, *Journal of Photochemistry and Photobiology C: Photochemistry Reviews*, 11 (2010) 179-209.
- [122] M. Van Hollebeke, L.M. Sung, F. McDonald, *Solar Physics*, 41 (1975) 189-223.
- [123] R. Daghrir, P. Drogui, D. Robert, *Industrial & Engineering Chemistry Research*, 52 (2013) 3581-3599.
- [124] J. Wen, J. Xie, X. Chen, X. Li, *Applied Surface Science*, 391 (2017) 72-123.
- [125] A.S. Weingarten, R.V. Kazantsev, L.C. Palmer, M. McClendon, A.R. Koltonow, A.P. Samuel, D.J. Kiebal, M.R. Wasielewski, S.I. Stupp, *Nature chemistry*, 6 (2014) 964-970.
- [126] W. Jiang, W. Luo, R. Zong, W. Yao, Z. Li, Y. Zhu, *Small*, 12 (2016) 4370-4378.
- [127] M. Zhang, W. Jiang, D. Liu, J. Wang, Y. Liu, Y. Zhu, Y. Zhu, *Applied Catalysis B: Environmental*, 183 (2016) 263-268.
- [128] W. Jiang, Y. Zhu, G. Zhu, Z. Zhang, X. Chen, W. Yao, *Journal of Materials Chemistry A*, 5 (2017) 5661-5679.
- [129] X. Zhou, F. Peng, H. Wang, H. Yu, Y. Fang, *Chemical Communications*, 47 (2011) 10323-10325.
- [130] A. Maldotti, A. Molinari, R. Amadelli, *Chemical Reviews*, 102 (2002) 3811-3836.
- [131] G. Palmisano, E. García-López, G. Marci, V. Loddo, S. Yurdakal, V. Augugliaro, L. Palmisano, *Chemical Communications*, 46 (2010) 7074-7089.
- [132] B. Weng, S. Liu, Z.-R. Tang, Y.-J. Xu, *Rsc Advances*, 4 (2014) 12685-12700.
- [133] H. Li, X. He, Z. Kang, H. Huang, Y. Liu, J. Liu, S. Lian, C.H.A. Tsang, X. Yang, S.T. Lee, *Angewandte Chemie International Edition*, 49 (2010) 4430-4434.
- [134] S. Yang, Y. Gong, J. Zhang, L. Zhan, L. Ma, Z. Fang, R. Vajtai, X. Wang, P.M. Ajayan, *Advanced materials*, 25 (2013) 2452-2456.
- [135] L. Shi, T. Wang, H. Zhang, K. Chang, J. Ye, *Advanced functional materials*, 25 (2015) 5360-5367.
- [136] G. Li, Z. Lian, W. Wang, D. Zhang, H. Li, *Nano Energy*, 19 (2016) 446-454.
- [137] N. Murakami, S. Kawakami, T. Tsubota, T. Ohno, *Journal of Molecular Catalysis A: Chemical*, 358 (2012) 106-111.
- [138] L.G. Devi, R. Kavitha, *Applied Catalysis B: Environmental*, 140 (2013) 559-587.
- [139] J. Fang, H. Fan, Y. Ma, Z. Wang, Q. Chang, *Applied Surface Science*, 332 (2015) 47-54.
- [140] X. Wang, X. Chen, A. Thomas, X. Fu, M. Antonietti, *Advanced Materials*, 21 (2009) 1609-1612.
- [141] Z. Ding, X. Chen, M. Antonietti, X. Wang, *ChemSusChem*, 4 (2011) 274-281.
- [142] L.-F. Gao, T. Wen, J.-Y. Xu, X.-P. Zhai, M. Zhao, G.-W. Hu, P. Chen, Q. Wang, H.-L. Zhang, *ACS applied materials & interfaces*, 8 (2015) 617-624.

- [143] S. Hu, R. Jin, G. Lu, D. Liu, J. Gui, *Rsc Advances*, 4 (2014) 24863-24869.
- [144] J. Tian, Q. Liu, A.M. Asiri, A.H. Qusti, A.O. Al-Youbi, X. Sun, *Nanoscale*, 5 (2013) 11604-11609.
- [145] M. Wu, J.M. Yan, X.n. Tang, M. Zhao, Q. Jiang, *ChemSusChem*, 7 (2014) 2654-2658.
- [146] M. Zhang, X. Bai, D. Liu, J. Wang, Y. Zhu, *Applied Catalysis B: Environmental*, 164 (2015) 77-81.
- [147] X. Ma, Y. Lv, J. Xu, Y. Liu, R. Zhang, Y. Zhu, *The Journal of Physical Chemistry C*, 116 (2012) 23485-23493.
- [148] J. Ran, T.Y. Ma, G. Gao, X.-W. Du, S.Z. Qiao, *Energy & Environmental Science*, 8 (2015) 3708-3717.
- [149] H. Xu, Z. Wu, Y. Wang, C. Lin, *Journal of Materials Science*, (2017) 1-14.
- [150] J. Cui, S. Liang, X. Wang, J. Zhang, *Materials Chemistry and Physics*, 161 (2015) 194-200.
- [151] S. Lin, X. Ye, X. Gao, J. Huang, *Journal of Molecular Catalysis A: Chemical*, 406 (2015) 137-144.
- [152] S. Hu, J. Zhu, L. Wu, X. Wang, P. Liu, Y. Zhang, Z. Li, *The Journal of Physical Chemistry C*, 115 (2010) 460-467.
- [153] H. Wang, L. Zhang, Z. Chen, J. Hu, S. Li, Z. Wang, J. Liu, X. Wang, *Chemical Society Reviews*, 43 (2014) 5234-5244.
- [154] Y. Wang, Q. Wang, X. Zhan, F. Wang, M. Safdar, J. He, *Nanoscale*, 5 (2013) 8326-8339.
- [155] J. Zhang, M. Zhang, R.Q. Sun, X. Wang, *Angewandte Chemie*, 124 (2012) 10292-10296.
- [156] J. Yu, S. Wang, J. Low, W. Xiao, *Physical Chemistry Chemical Physics*, 15 (2013) 16883-16890.
- [157] Z. Jiang, C. Zhu, W. Wan, K. Qian, J. Xie, *Journal of Materials Chemistry A*, 4 (2016) 1806-1818.
- [158] F. Ke, L. Wang, J. Zhu, *Nano Research*, 8 (2015) 1834-1846.
- [159] A. Dhakshinamoorthy, A.M. Asiri, H. García, *Angewandte Chemie International Edition*, 55 (2016) 5414-5445.
- [160] H. Wang, X. Yuan, Y. Wu, G. Zeng, X. Chen, L. Leng, H. Li, *Applied Catalysis B: Environmental*, 174 (2015) 445-454.
- [161] R. Chen, J. Zhang, Y. Wang, X. Chen, J.A. Zapien, C.-S. Lee, *Nanoscale*, 7 (2015) 17299-17305.
- [162] N. Vallavoju, J. Sivaguru, *Chemical Society Reviews*, 43 (2014) 4084-4101.
- [163] M. Shalom, S. Inal, C. Fettkenhauer, D. Neher, M. Antonietti, *Journal of the American Chemical Society*, 135 (2013) 7118-7121.
- [164] X.-H. Li, J. Zhang, X. Chen, A. Fischer, A. Thomas, M. Antonietti, X. Wang, *Chemistry of Materials*, 23 (2011) 4344-4348.
- [165] J. Sun, J. Zhang, M. Zhang, M. Antonietti, X. Fu, X. Wang, *Nature Communications*, 3 (2012) 1139.
- [166] J. Liu, H. Wang, Z.P. Chen, H. Moehwald, S. Fiechter, R. van de Krol, L. Wen, L. Jiang, M. Antonietti, *Advanced Materials*, 27 (2015) 712-718.
- [167] Z. Yang, Y. Zhang, Z. Schnepf, *Journal of Materials Chemistry A*, 3 (2015) 14081-14092.

- [168] H. Yan, *Chemical Communications*, 48 (2012) 3430-3432.
- [169] F. He, G. Chen, Y. Yu, Y. Zhou, Y. Zheng, S. Hao, *Chemical Communications*, 51 (2015) 425-427.
- [170] Z. Lin, X. Wang, *ChemSusChem*, 7 (2014) 1547-1550.
- [171] C. Zhao, G. Tan, J. Huang, W. Yang, H. Ren, A. Xia, *ACS applied materials & interfaces*, 7 (2015) 23949-23957.
- [172] G. Zhang, G. Li, X. Wang, *ChemCatChem*, 7 (2015) 2864-2870.
- [173] W. Pipornpong, R. Wanbayor, V. Ruangpornvisuti, *Applied Surface Science*, 257 (2011) 10322-10328.
- [174] F. Wang, Y. Zhou, P. Li, L. Kuai, Z. Zou, *Chinese Journal of Catalysis*, 37 (2016) 863-868.
- [175] L. Yang, J. Huang, L. Shi, L. Cao, Q. Yu, Y. Jie, J. Fei, H. Ouyang, J. Ye, *Applied Catalysis B: Environmental*, 204 (2017) 335-345.
- [176] P. Zhang, H. Li, Y. Wang, *Chemical Communications*, 50 (2014) 6312-6315.
- [177] S. Chen, P. Slattum, C. Wang, L. Zang, *Chemical reviews*, 115 (2015) 11967-11998.
- [178] M. Grzelczak, J. Vermant, E.M. Furst, L.M. Liz-Marzán, *ACS nano*, 4 (2010) 3591-3605.
- [179] D. González-Rodríguez, A.P. Schenning, *Chemistry of Materials*, 23 (2010) 310-325.
- [180] Z.-G. Gu, Z. Chen, W.-Q. Fu, F. Wang, J. Zhang, *ACS applied materials & interfaces*, 7 (2015) 28585-28590.
- [181] J.W. Steed, J.L. Atwood, P.A. Gale, *Definition and emergence of supramolecular chemistry*, Wiley Online Library 2012.
- [182] J.W. Steed, *Chemical Communications*, 47 (2011) 1379-1383.
- [183] N. Fechner, M. Antonietti, *Nano Today*, 10 (2015) 593-614.
- [184] J. Zhang, X. Chen, K. Takahashi, K. Maeda, K. Domen, J.D. Epping, X. Fu, M. Antonietti, X. Wang, *Angewandte Chemie International Edition*, 49 (2010) 441-444.
- [185] W.-J. Ong, L.-L. Tan, S.-P. Chai, S.-T. Yong, A.R. Mohamed, *Nano Energy*, 13 (2015) 757-770.
- [186] W.-J. Ong, L.-L. Tan, S.-P. Chai, S.-T. Yong, *Dalton Transactions*, 44 (2015) 1249-1257.
- [187] Y.S. Jun, E.Z. Lee, X. Wang, W.H. Hong, G.D. Stucky, A. Thomas, *Advanced Functional Materials*, 23 (2013) 3661-3667.
- [188] J. Tian, R. Ning, Q. Liu, A.M. Asiri, A.O. Al-Youbi, X. Sun, *ACS applied materials & interfaces*, 6 (2014) 1011-1017.
- [189] C. Gambarotti, L. Melone, T. Caronna, C. Punta, *Current Organic Chemistry*, 17 (2013) 2406-2419.
- [190] Q. Lin, L. Li, S. Liang, M. Liu, J. Bi, L. Wu, *Applied Catalysis B: Environmental*, 163 (2015) 135-142.
- [191] Q. Xiang, J. Yu, M. Jaroniec, *Chemical Society Reviews*, 41 (2012) 782-796.
- [192] N.P. Wickramaratne, J. Xu, M. Wang, L. Zhu, L. Dai, M. Jaroniec, *Chemistry of Materials*, 26 (2014) 2820-2828.

- [193] J. Liu, H. Wang, M. Antonietti, *Chemical Society Reviews*, 45 (2016) 2308-2326.
- [194] F. Goettmann, A. Fischer, M. Antonietti, A. Thomas, *Angewandte Chemie International Edition*, 45 (2006) 4467-4471.
- [195] C. Cheng, Y. Huang, J. Wang, B. Zheng, H. Yuan, D. Xiao, *Analytical chemistry*, 85 (2013) 2601-2605.
- [196] W. Ma, D. Han, M. Zhou, H. Sun, L. Wang, X. Dong, L. Niu, *Chemical Science*, 5 (2014) 3946-3951.
- [197] X. Zhang, H. Wang, H. Wang, Q. Zhang, J. Xie, Y. Tian, J. Wang, Y. Xie, *Advanced materials*, 26 (2014) 4438-4443.
- [198] J. Liu, J. Huang, H. Zhou, M. Antonietti, *ACS applied materials & interfaces*, 6 (2014) 8434-8440.
- [199] R. Cazelles, J. Liu, M. Antonietti, *ChemElectroChem*, 2 (2015) 333-337.
- [200] W.J. Lee, U.N. Maiti, J.M. Lee, J. Lim, T.H. Han, S.O. Kim, *Chemical Communications*, 50 (2014) 6818-6830.
- [201] X.-H. Li, M. Antonietti, *Chemical Society Reviews*, 42 (2013) 6593-6604.
- [202] L. Li, Y. Zhao, M. Antonietti, M. Shalom, *Small*, 12 (2016) 6090-6097.
- [203] N. Fechler, N.P. Zussblatt, R. Rothe, R. Schlögl, M.G. Willinger, B.F. Chmelka, M. Antonietti, *Advanced Materials*, 28 (2016) 1328-1328.
- [204] Z.P. Chen, M. Antonietti, D. Dontsova, *Chemistry-A European Journal*, 21 (2015) 10805-10811.
- [205] W. Lubitz, W. Tumas, *Hydrogen: an overview*, ACS Publications, 2007.
- [206] M.G. Walter, E.L. Warren, J.R. McKone, S.W. Boettcher, Q. Mi, E.A. Santori, N.S. Lewis, *Chemical reviews*, 110 (2010) 6446-6473.
- [207] S.J. Moniz, S.A. Shevlin, D.J. Martin, Z.-X. Guo, J. Tang, *Energy & Environmental Science*, 8 (2015) 731-759.
- [208] R. Marschall, *Advanced Functional Materials*, 24 (2014) 2421-2440.
- [209] Y. Cheng, S.P. Jiang, *Progress in natural science: materials international*, 25 (2015) 545-553.
- [210] A. Tanaka, K. Hashimoto, H. Kominami, *Journal of the American Chemical Society*, 136 (2014) 586-589.
- [211] G. Zhang, S. Zang, L. Lin, Z.-A. Lan, G. Li, X. Wang, *ACS applied materials & interfaces*, 8 (2016) 2287-2296.
- [212] G. Zhang, S. Zang, X. Wang, *Acs Catalysis*, 5 (2015) 941-947.
- [213] J. Liu, Y. Liu, N. Liu, Y. Han, X. Zhang, H. Huang, Y. Lifshitz, S.-T. Lee, J. Zhong, Z. Kang, *Science*, 347 (2015) 970-974.
- [214] G. Gao, Y. Jiao, F. Ma, Y. Jiao, E. Waclawik, A. Du, *Physical Chemistry Chemical Physics*, 17 (2015) 31140-31144.
- [215] J. Xu, S. Cao, T. Brenner, X. Yang, J. Yu, M. Antonietti, M. Shalom, *Advanced Functional Materials*, 25 (2015) 6265-6271.

- [216] T. Jordan, N. Fechler, J. Xu, T.J. Brenner, M. Antonietti, M. Shalom, *ChemCatChem*, 7 (2015) 2826-2830.
- [217] Y. Ishida, L. Chabanne, M. Antonietti, M. Shalom, *Langmuir*, 30 (2014) 447-451.
- [218] B. Roy, P. Baire, A.K. Nandi, *RSC Advances*, 4 (2014) 1708-1734.
- [219] M. Prager, W. Sawka-Dobrowolska, L. Sobczyk, A. Pawlukojć, E. Grech, A. Wischniewski, M. Zamponi, *Chemical physics*, 332 (2007) 1-9.
- [220] L. Li, M. Shalom, Y. Zhao, J. Barrio, M. Antonietti, *Journal of Materials Chemistry A*, 5 (2017) 18502-18508.
- [221] C. Ronning, H. Feldermann, R. Merk, H. Hofsäss, P. Reinke, J.-U. Thiele, *Physical Review B*, 58 (1998) 2207.
- [222] M.M. Unterlass, F. Emmerling, M. Antonietti, J. Weber, *Chemical communications*, 50 (2014) 430-432.
- [223] W.-J. Ong, L.-L. Tan, Y.H. Ng, S.-T. Yong, S.-P. Chai, *Chemical reviews*, 116 (2016) 7159-7329.
- [224] C. Ye, J.-X. Li, Z.-J. Li, X.-B. Li, X.-B. Fan, L.-P. Zhang, B. Chen, C.-H. Tung, L.-Z. Wu, *ACS Catalysis*, 5 (2015) 6973-6979.
- [225] H. Yu, R. Shi, Y. Zhao, T. Bian, Y. Zhao, C. Zhou, G.I. Waterhouse, L.Z. Wu, C.H. Tung, T. Zhang, *Advanced Materials*, 29 (2017).
- [226] Z. Hong, B. Shen, Y. Chen, B. Lin, B. Gao, *Journal of Materials Chemistry A*, 1 (2013) 11754-11761.
- [227] H. Yu, R. Shi, Y. Zhao, T. Bian, Y. Zhao, C. Zhou, G.I. Waterhouse, L.Z. Wu, C.H. Tung, T. Zhang, *Advanced Materials*, 29 (2017).
- [228] P. Niu, L.C. Yin, Y.Q. Yang, G. Liu, H.M. Cheng, *Advanced Materials*, 26 (2014) 8046-8052.
- [229] H.L. Lee, Z. Sofer, V. Mazánek, J. Luxa, C.K. Chua, M. Pumera, *Applied Materials Today*, (2016).
- [230] M. Rueping, S. Zhu, R.M. Koenigs, *Chemical Communications*, 47 (2011) 12709-12711.
- [231] T. Castanheiro, J. Suffert, M. Donnard, M. Gulea, *Chemical Society Reviews*, 45 (2016) 494-505.
- [232] I. Wilson, G. Harris, *Journal of the American Chemical Society*, 83 (1961) 286-289.
- [233] R. Jenny, M. Botz, D. Dimitriadis, T. Polglase, W. Phillips, *Minerals and Metallurgical Processing*, 18 (2001) 126-132.
- [234] A. Majumdar, S.C. Das, T. Shripathi, R. Hippler, *Composite Interfaces*, 19 (2012) 161-170.
- [235] M. González-Torres, M.G. Olayo, G.J. Cruz, L.M. Gómez, V. Sánchez-Mendieta, F. González-Salgado, *Advances in Chemistry*, 2014 (2014).
- [236] X. Miao, X. Yan, D. Qu, D. Li, F. Tao, Z. Sun, *ACS Applied Materials & Interfaces*, (2017).
- [237] A. U. Meyer, V. W. Lau, B. König, B. V. Lotsch, *European Journal of Organic Chemistry*, 15(2017), 2179-2185.



[238] A. U. Meyer, S. Jager, D. P. Hari, B. König, B. V. Lotsch, *Adv. Synth. Catal.* 357 (2015), 2050 – 2054.